

**AN EXAMINATION OF THE THERMOPIEZOELECTRIC EFFECT  
IN PIEZOELECTRIC ACTUATORS VIA FINITE ELEMENTS**

RAFAEL TOLEDO

A THESIS SUBMITTED TO THE FACULTY OF GRADUATE STUDIES  
IN PARTIAL FULFILMENT OF THE REQUIREMENTS  
FOR THE DEGREE OF

MASTER OF SCIENCE

GRADUATE PROGRAM IN EARTH AND SPACE SCIENCE  
YORK UNIVERSITY  
TORONTO, ONTARIO  
SEPTEMBER 2023

©Rafael Toledo, 2023

## **Abstract**

The application of piezoelectric actuators in smart structures is a rapidly developing field, especially in aerospace environments. Since thermal effects play an important role in aerospace environments, thermopiezoelectricity has been studied as it takes into account the thermal field in addition to the mechanical and electrical fields. As a result, the coupling effects among these three fields have to be considered, including the pyroelectric (change in the electric potential due to the presence of a thermal field) and electrocaloric (change in the temperature when an electric field is applied) effects. This thesis presents an examination of how these coupled effects can affect the performance of piezoelectric bender and stack actuators in varying external environments. More specifically, this thesis investigates the influence of the pyroelectric and electrocaloric effects on the positioning and dynamic performance of these actuators in static and dynamic cases by using a custom written finite element code that considers the three fully coupled field equations of thermopiezoelectricity.

*This thesis is dedicated to my family*

## Acknowledgements

I would like to sincerely thank my supervisor, Dr. Ryan Orszulik, for accepting me as a graduate student in 2020 and firmly holding my position until 2021 during the challenges of the pandemic. His support, mentorship, patience, and valuable insights have been crucial to my academic journey. Dr. Orszulik's continuous encouragement to strive for excellence has not only shaped the quality and direction of my research but has also inspired me to reach new heights, and I am thankful to have had him as a mentor throughout my graduate study period.

I also want to thank my labmates over the years – Rita, Ariel, Arvin, Annamalai, Simon, and Ian – for their contributions during work and conversations during our coffee breaks.

I want to express my gratitude to Diana, Joaquin, and Miriam, who provided emotional support, lent a listening ear to my frustrations, and celebrated the successes of this academic journey with me. Finally, my forever thanks go to my parents, Adilson and Rosangela, and my siblings, Paula and Marcus, for their

support and encouragement throughout this academic endeavor. Their love and understanding provided the foundation upon which I could pursue and achieve my educational goals.

# Table of Contents

<b>Abstract</b>	<b>ii</b>
<b>Dedication</b>	<b>iii</b>
<b>Acknowledgements</b>	<b>iv</b>
<b>Table of Contents</b>	<b>vi</b>
<b>List of Tables</b>	<b>xi</b>
<b>List of Figures</b>	<b>xiii</b>
<b>1 Introduction</b>	<b>1</b>
1.1 The Finite Element Method . . . . .	2
1.2 Piezoelectric Effect . . . . .	6
1.2.1 Piezoelectric Materials . . . . .	7
1.2.2 Piezoelectric Sensors . . . . .	11

1.2.3	Piezoelectric Actuators . . . . .	13
1.2.3.1	Stack Actuators . . . . .	13
1.2.3.2	Bender Actuators . . . . .	15
1.3	Linear Theory of Piezoelectricity . . . . .	18
1.4	Thermopiezoelectricity . . . . .	20
1.5	Research Objectives and Contributions . . . . .	23
1.6	Organization . . . . .	26
<b>2</b>	<b>Finite Element Implementation and Verification</b>	<b>28</b>
2.1	Classical Shape Functions . . . . .	32
2.2	Isoparametric Formulation . . . . .	33
2.3	Higher-Order Shape Functions . . . . .	34
2.4	Gaussian Quadrature . . . . .	37
2.5	Thermopiezoelectric Finite Element Formulation . . . . .	41
2.6	Boundary Conditions . . . . .	52
2.6.1	Homogeneous Boundary Conditions . . . . .	54
2.6.2	Non-homogeneous Boundary Conditions . . . . .	56
2.7	Static Analysis . . . . .	57
2.8	Modal Analysis . . . . .	59
2.9	Dynamic Analysis . . . . .	61

2.9.1	Newmark Integration Method . . . . .	62
2.10	Verification of Static Analysis . . . . .	65
2.10.1	Three-Dimensional Solid Element with Reduced Integration	66
2.10.1.1	Three-Dimensional Solid Static Case . . . . .	67
2.10.2	Piezoelectric Element . . . . .	68
2.10.2.1	Piezoelectric Static Case 1 . . . . .	68
2.10.2.2	Piezoelectric Static Case 2 . . . . .	69
2.10.3	Thermoelastic Element . . . . .	71
2.10.3.1	Thermoelastic Static Case . . . . .	71
2.10.4	Verification of Numerical Analysis with Benchmark . . . . .	72
2.11	Verification of Transient Analysis . . . . .	75
2.11.1	Rayleigh Damping Coefficients . . . . .	76
2.11.2	Three-Dimensional Solid Element . . . . .	77
2.11.2.1	Three-Dimensional Solid Transient Case . . . . .	77
2.11.3	Piezoelectric Element . . . . .	80
2.11.3.1	Piezoelectric Transient Case . . . . .	80
2.11.4	Thermoelastic Element . . . . .	82
2.11.4.1	Thermoelastic Transient Case . . . . .	82
2.12	Thermopiezoelectric Element . . . . .	84

<b>3 Examination of the Thermopiezoelectric Effect in Multilayer Stack</b>	
<b>Actuators</b>	<b>90</b>
3.1 Scaling Factor and Validation . . . . .	92
3.2 Rotation Matrices . . . . .	93
3.3 Step Input Signal . . . . .	95
3.3.1 Step Input for a 1-Layer Model . . . . .	96
3.3.2 Step Input for a 7-Layer Model . . . . .	98
3.3.3 Step Input for a 375-layer Model . . . . .	102
3.4 Thermal Load . . . . .	105
<b>4 Examination of the Thermopiezoelectric Effect in Multimorph Bender Actuators</b>	<b>108</b>
4.1 Differential Voltage Control for Displacement Test . . . . .	111
4.1.1 Displacement Test 1 . . . . .	112
4.1.2 Displacement Test 2 . . . . .	114
4.2 Transient Analysis . . . . .	115
4.2.1 Step Input . . . . .	115
4.2.2 Sinusoidal Input . . . . .	120
4.2.3 Thermal Load . . . . .	125
<b>5 Temperature Dependence of the Piezoelectric Strain Coefficients</b>	<b>127</b>

5.1	Stack Actuators with Varying Piezoelectric Strain Coefficients Matrix	130
5.1.1	Step Input . . . . .	132
5.2	Bender Actuators with Varying Piezoelectric Strain Coefficients Matrix	133
5.2.1	Step Input . . . . .	135
5.2.2	Thermal Load . . . . .	136
5.3	Case Study: A Stratospheric Balloon Flight . . . . .	138
<b>6</b>	<b>Conclusions and Future Work</b>	<b>144</b>
6.1	Future Work . . . . .	149
<b>A</b>	<b>Appendix A</b>	<b>151</b>
	<b>Bibliography</b>	<b>151</b>

## List of Tables

1.1	PZT ceramics properties for room temperature (25°C). (Source:[1])	10
1.2	Piezoelectric stack actuator specifications. (Source:[2]) . . . . .	15
1.3	Piezo bender actuator specifications from <i>PI Ceramics</i> [2] . . . . .	18
1.4	A comparison of the capabilities of commercial software . . . . .	24
2.1	Gaussian points and weights . . . . .	38
2.2	Normalized tip deflection of a cantilever beam ( $w_{fem}/w_{exact}$ ) as compared to the Bernoulli-Euler theory prediction for a reference problem. (Source:[3]) . . . . .	41
2.3	A comparison of the first five natural frequencies between the FE Code and ABAQUS . . . . .	60
2.4	Steps of the Newmark integration method . . . . .	65
2.5	Material coefficients PVDF . . . . .	74
2.6	First 5 natural frequencies of the PL127.10 actuator . . . . .	76
2.7	Material parameters for the considered five-layer plate. (Source: [4])	86

3.1	P-887.51 specifications. (Source: [2]) . . . . .	90
3.2	Material parameters of the P-887.51 actuator. (Source: [2]) . . . . .	91
4.1	PB4NB2W bender actuator specifications (Source: [5]) . . . . .	109
4.2	Material parameters of PB4NB2W actuator. (Source: [5]) . . . . .	110
4.3	Differential voltage control . . . . .	111
5.1	Newmark integration steps for consideration of the dependence of the piezoelectric strain coefficient $d_{31}$ and $d_{33}$ on temperature . . . . .	129
A.1	External force equations for thermopiezoelectric finite element formulation . . . . .	151
A.2	Thermopiezoelectric finite element equations of stationary terms . . . . .	152
A.3	Thermopiezoelectric finite element equations of dynamic terms . . . . .	153

## List of Figures

1.1	Example of 1D, 2D, and 3D structures. (Source: [6]) . . . . .	4
1.2	Example of 1D, 2D, and 3D discretization. (Source: [6]) . . . . .	4
1.3	The discretization, or mesh, of a generic aircraft (Image source: [7])	5
1.4	(a) Direct piezoelectric effect. (b) Converse piezoelectric effect. (Image source: [8]) . . . . .	7
1.5	Barium titanate crystal structure. (Image source: [9]) . . . . .	9
1.6	Piezoelectric stack actuator. (Image source: [2]) . . . . .	14
1.7	Unimorph and bimorph structures. (Image source: [10]) . . . . .	16
1.8	Bimorph series connection. (Image source: [2]) . . . . .	17
1.9	Bimorph parallel connection. (Image source: [2]) . . . . .	17
1.10	Multimorph actuator. (Image source: [2]) . . . . .	17
2.1	Finite element analysis procedure . . . . .	31
2.2	Nodes and degrees of freedom of a bar element. (Image adapted from: [11]) . . . . .	32

2.3	Nodes and degrees of freedom of bar element: quadratic or higher-order shape function. (Source: [12]) . . . . .	35
2.4	Reference 20-noded hexahedral element ( $-1 \leq \xi_1 \leq 1, -1 \leq \xi_2 \leq 1, -1 \leq \xi_3 \leq 1$ ). (Image adapted from: [13]) . . . . .	36
2.5	Illustration of the location of Gauss points. (Image adapted from: [6])	38
2.6	Example of Gaussian quadrature full integration of a 20-noded hexahedral element. (Image adapted from: [14]) . . . . .	39
2.7	Example of Gaussian quadrature reduced integration of 20-noded hexahedral element. (Image adapted from: [14]) . . . . .	40
2.8	Example of boundary conditions: Neumann (1), Dirichlet (2). (Image adapted from:[15]) . . . . .	53
2.9	Five mode shapes of the PL127.10 modal analysis in the FE code .	61
2.10	Rectangular structure with 2 attached layers with dimensions of $31 \times 9.6 \times 0.67$ mm . . . . .	66
2.11	Aluminum plate with forces (red arrows) applied on the edge nodes	67
2.12	Developed displacement in $z$ for the three-dimensional solid static case	68
2.13	Displacement in $z$ and voltage results for the piezoelectric static case 1	69
2.14	Bimorph PL127.10 with a concentrated force applied in the right end, middle node. . . . .	70
2.15	Displacement in $z$ and voltage results for the piezoelectric static case 2	71

2.16 Displacement in $x$ and temperature results for a thermal load application . . . . .	72
2.17 Bimorph beam consisting of PVDF material with dimensions $100 \times 5 \times 1$ mm . . . . .	73
2.18 Transverse deflection . . . . .	75
2.19 Node of interest (red point) . . . . .	78
2.20 Time versus nodal $z$ -displacement at reference node . . . . .	78
2.21 Transverse deflection at time $t = 1$ second across the length of the actuator . . . . .	79
2.22 Sinusoidal wave . . . . .	80
2.23 Time versus nodal $z$ -displacement at reference node (node 4) . . . . .	81
2.24 Transverse deflection at time $t = 0.25$ seconds and $0.75$ seconds . . . . .	82
2.25 Sinusoidal thermal load applied in time . . . . .	83
2.26 Deflection of the bimorph at reference node due to thermal load . . . . .	84
2.27 Laminate configuration. (Source: [4]) . . . . .	85
2.28 Non-dimensional transverse deflection . . . . .	88
2.29 The induced electric potential at $[y^*, -0.5t]$ due to a thermal load . . . . .	89
3.1 Multilayer stack actuator (Source: [2]) . . . . .	91
3.2 Displacement of the stack actuator with voltage scaling for the nominal displacement . . . . .	93

3.3	Stack actuator modeled as 1-layer with the reference node highlighted	97
3.4	Developed voltage, $z$ -deflection, and temperature for the reference node . . . . .	97
3.5	Developed temperature due to step input for a 1-layer stack model .	98
3.6	7-layer stack actuator with electric connection and reference node .	99
3.7	Developed voltage, $z$ -deflection, and temperature for the reference node . . . . .	100
3.8	Developed temperature of the 7-layer stack actuator due to a step input . . . . .	101
3.9	Time versus $z$ -displacement for thermopiezoelectric and piezoelectric simulations . . . . .	102
3.10	Developed displacement of the 375-layer stack actuator due to a step input . . . . .	103
3.11	Developed temperature of the 375-layer stack actuator . . . . .	104
3.12	Developed displacement in $z$ through the length for 1 layer, 7 layers, and 375 layers . . . . .	105
3.13	Sinusoidal thermal load . . . . .	106
3.14	Stack actuator under thermal load considering the pyroelectric effect versus neglecting the pyroelectric effect . . . . .	107
4.1	Bimorph actuator. (Source: [5]) . . . . .	109

4.2	Polarization direction and voltage application to a multilayer bender actuator. (Source: [2]) . . . . .	112
4.3	PB4NB2W diagram - $xz$ view: polarization direction . . . . .	112
4.4	Bender actuator model with mechanical boundary conditions depicted	113
4.5	Developed displacement of the bender actuator due to a constant bias of 150 V and a variable voltage of 150 V . . . . .	114
4.6	Developed displacement of the bender actuator due to a constant bias of 150 V and a variable voltage of 0 V . . . . .	115
4.7	Reference node (red dot) in $yz$ view . . . . .	116
4.8	Bender actuator due to a step signal . . . . .	117
4.9	Thermopiezoelectric analysis versus piezoelectric analysis . . . . .	119
4.10	Unipolar sinusoidal wave signal . . . . .	120
4.11	Developed temperature at different times considering the pyroelec- tric effect . . . . .	122
4.12	Developed temperature at different times neglecting the pyroelectric effect . . . . .	124
4.13	Bender actuator under thermal load considering the pyroelectric ef- fect versus without the pyroelectric effect . . . . .	126
5.1	Evolution of the piezoelectric coefficient $d_{33}$ as a function of temper- ature for soft PZT type. (Source:[16]) . . . . .	131

5.2	Evolution of the piezoelectric coefficient $d_{33}$ as a function of temperature for PZT 5A ceramic . . . . .	131
5.3	Time versus developed $z$ -displacement . . . . .	133
5.4	Evolution of the piezoelectric coefficient $d_{31}$ as a function of temperature for PZT type. (Source: [1]) . . . . .	134
5.5	Time versus developed $z$ -displacement for a voltage step . . . . .	136
5.6	Displacement in $z$ caused by a dynamic thermal load . . . . .	138
5.7	Step input that scans across the bimorph range and the ambient temperature variation that occurs during the simulation . . . . .	139
5.8	Multimorph bender actuator performance with changing ambient conditions while scanning across the full range . . . . .	142
5.9	Displacement of the bender actuator due to step input signals and temperature variations . . . . .	143

# 1 Introduction

Piezoelectricity is a phenomenon by which an electric field is generated when mechanical pressure is applied to a material, or when mechanical strain is produced when an electric field is applied. It is referred to as the direct piezoelectric effect when an electric field is produced, and the converse piezoelectric effect when mechanical strain is generated [17, 18, 19].

The piezoelectric effect is present in many applications, including quartz watches (an electronic oscillator regulated by a quartz crystal), SONAR systems (piezoelectric transducers that convert mechanical energy into electric signals due to the direct piezoelectric effect), ultrasound machines (piezoelectric transducers which convert electrical energy into mechanical vibrations, creating ultrasound waves for medical imaging applications due to the converse piezoelectric effect), and smart structures in aerospace applications (piezoelectric actuators that convert voltage into mechanical displacement due to the converse piezoelectric effect) [20, 4]. The application of piezoelectric actuators in smart structures is a rapidly developing field, especially in

aerospace environments, and has received significant attention in recent years. The performance of actuators must be ensured when large, possibly rapid, temperature variations are considered, which is the case particularly in aerospace environments and therefore, the theory of thermopiezoelectricity must be applied. Thermopiezoelectricity considers the thermal field in addition to the electrical and mechanical fields [4], and thus the coupling effects among these three fields must be taken into account, including the pyroelectric and electrocaloric effects. The pyroelectric effect is a phenomenon observed in certain materials in which voltage can be produced in response to variations in temperature. The electrocaloric effect is the opposite, where temperature can be generated due to an applied electric potential.

This thesis focuses on analyzing the three fully-coupled field equations of thermopiezoelectricity derived by Gornandt and Gabbert [4] and their impact on piezoelectric bending and stack actuators. To achieve this, a finite element code is implemented in MATLAB. Static and dynamic models are developed to accurately quantify the influence of the pyroelectric and electrocaloric effects on the positioning and dynamic performance of these actuators.

## **1.1 The Finite Element Method**

The finite element method is a numerical technique used for solving a vast number of problems in the fields of engineering and physics. In structural applica-

tions, when dealing with physical systems characterized by complex geometries and material properties, analytical approaches may not be viable. In such cases, the application of a numerical method like the finite element method becomes essential to obtain approximate solutions [21]. The finite element method subdivides the studied body into a discrete number of simplified subdomains referred to as finite elements. These elements are interconnected at specific points known as nodes. This process, known as discretization [21], allows complex geometries and physical behaviors to be represented in a more manageable manner for computational analysis. The finite element method involves formulating equations to describe the behavior of each individual finite element based on the physics and boundary conditions of the problem.

In structural applications, the problem is typically simplified to a one-dimensional, two-dimensional, or three-dimensional domain, typical examples of which can be seen in Fig. 1.1. These domains can then be discretized as demonstrated in Fig. 1.2. The 1D structure can be discretized simply, for example, with beam elements, which is demonstrated in Fig. 1.2(a). The 2D domain has a simpler geometry and therefore simpler discretization process is required, where surface element with quadrilaterals and triangles are used, as shown in Fig. 1.2(b). The example of a 3D structure can be discretized using 3D solid elements, known as brick elements, as shown in Fig. 1.2(c). It is important to mention that in this particular example, there is a gap

between the physical and finite element model domain, which typically cannot be avoided in the discretization process [6]. Complex geometries require a discretization process that will result in a more complex mesh, as an example of which can be seen in Fig. 1.3.

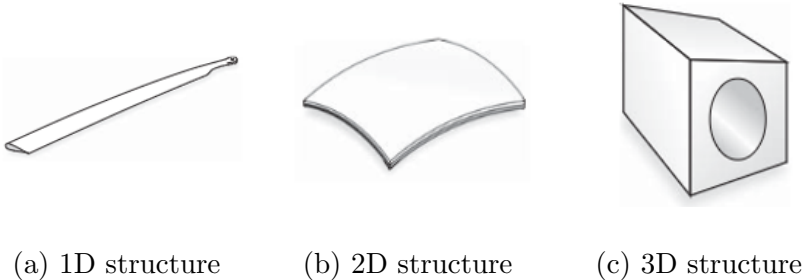


Fig. 1.1 Example of 1D, 2D, and 3D structures. (Source: [6])

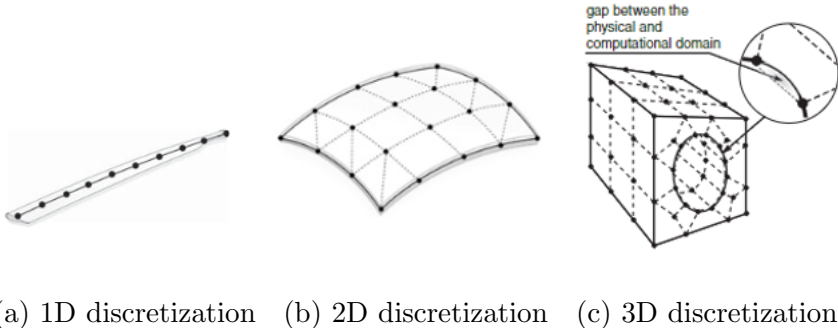


Fig. 1.2 Example of 1D, 2D, and 3D discretization. (Source: [6])



Fig. 1.3 The discretization, or mesh, of a generic aircraft (Image source: [7])

Without loss of generality, the behavior of individual subdomains for a linear static case can be described in a compact matrix form as

$$k^e u^e = f^e \quad (1.1)$$

where  $k^e$  is referred to as the element stiffness matrix,  $u^e$  is the vector of element nodal degrees of freedom, and  $f^e$  is the vector of element nodal forces. The elements are globally combined, and the equations can be solved to obtain the global behavior of the entire body. The finite element method finds applications in many engineering fields, including structural analysis, heat transfer, fluid dynamics, and piezoelectric analysis, providing accurate and reliable solutions [21].

## 1.2 Piezoelectric Effect

The piezoelectric effect was discovered in 1880 by the brothers Pierre and Jacques Curie. By that time, it was already accepted that some crystals could generate electricity when heated, which is known as the pyroelectric effect. The Curie brothers demonstrated that crystals such as quartz, tourmaline, and sugar cane could generate electricity when subjected to mechanical pressure [22, 17, 23, 24, 25, 26, 19, 27]. This effect is referred to as the direct piezoelectric effect, and is demonstrated in Fig. 1.4(a). One year later, in 1881, Gabriel Lippman discovered the converse piezoelectric effect, in which a material exhibits mechanical strain proportional to the applied electric field [17, 26, 27], as shown in Fig. 1.4(b). The word “piezo” originates from Greek and means pressure, hence piezoelectricity refers to “pressure electricity”. Currently, there are numerous applications of piezoelectric materials, however, the first significant application was the development of a piezoelectric sonar instrument for submarines during World War I [22, 23, 17].

The direct piezoelectric effect occurs when force is applied via either tension or compression to the piezoelectric material, as its crystal structure changes, which results in positive and negative charges concentrating on opposite sides, and therefore net polarization occurs. A metal plate or electrodes gather these charges resulting in a measurable voltage across the material as demonstrated in Fig. 1.4(a) [20].

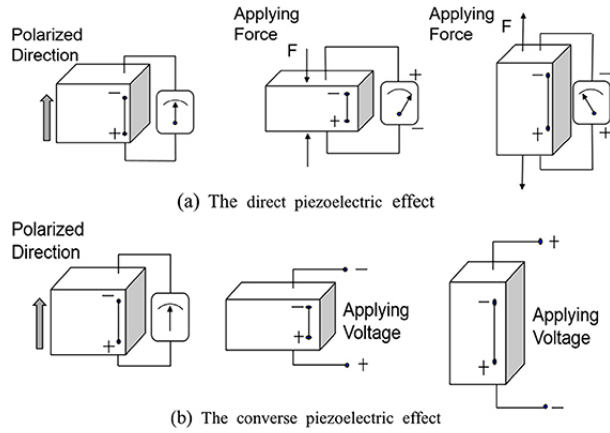


Fig. 1.4 (a) Direct piezoelectric effect. (b) Converse piezoelectric effect. (Image source: [8])

The converse piezoelectric effect is shown in Fig.1.4(b), in which the reverse process occurs. An electric field is applied, which results in deformation of the crystal structure. This deformation of the crystal structure converts the electric energy into mechanical strain, causing the material to change its shape. This process is widely used in actuators, since it provides a mechanical response to an input voltage [20].

### 1.2.1 Piezoelectric Materials

There are two types of piezoelectric materials: natural and synthetic. The first type are naturally occurring crystal materials such as Rochelle salt, quartz, and Tourmaline-group minerals. The second type of piezoelectric materials, the

synthetic, are polymers, composites, quartz analogs, and ceramics [19].

There are 32 classes of crystals and they can be divided into seven different groups according to the symmetry of the crystals faces [19, 28, 29]. From the 32 classes of crystals, only 20 contain piezoelectric properties, in which, ten of them are polar and the other half are non-polar. The main difference between them is that the polar presents spontaneous polarization, meaning that the crystal does not need to have an applied mechanical load to present polarization [19, 29]. This is known as a ferroelectric material, which was discovered in Rochelle salt by Valesk in 1921 [30]. By definition, all ferroelectric materials are pyroelectric (generate voltage when temperature changes), and all pyroelectric materials are piezoelectric, however not all piezoelectric materials are pyroelectric [20, 18].

During World War II, advances in piezoelectric research led to the discovery of a certain type of ceramic material that could show dielectric constants up to 100 times higher than usual crystals. Three different countries, USA, Japan and the USSR discovered at the same time that this ceramic material could be manufactured to provide piezoelectric and dielectric properties higher than the ones found in natural piezoelectric crystals. This ceramic was known as barium titanate ( $\text{BaTiO}_3$ ) and it presents a stable perovskite structure, which denotes any material with the chemical formula  $\text{ABO}_3$ , where A and B are cations, and O stands for oxygen (see Fig. 1.5). For different ranges of temperatures,  $\text{BaTiO}_3$  presents different crystal

system groups, such as trigonal for temperatures below  $-90^{\circ}\text{C}$ , orthorhombic for temperatures between  $-90^{\circ}$  and  $5^{\circ}\text{C}$ , and tetragonal for temperatures between  $5^{\circ}$  and  $120^{\circ}\text{C}$  [18].

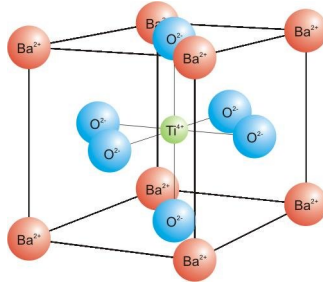


Fig. 1.5 Barium titanate crystal structure. (Image source: [9])

Lead titanate ( $\text{PbTiO}_3$ ) is another ceramic material with perovskite structure. It belongs to the tetragonal crystal system at room temperature, and as the temperature increases, the lead titanate structure transforms to a cubic lattice at the Curie temperature of  $490^{\circ}\text{C}$ , which is the temperature above which the material loses its piezoelectric and ferroelectric properties [18, 19, 17].

Lead zirconate titanate (PZT) was discovered in 1952 and it showed higher piezoelectric properties than barium titanate [31]. PZT is a solid solution of lead titanate ( $\text{PbTiO}_3$ ) and lead zirconate ( $\text{PbZrO}_3$ ), with chemical formula  $\text{Pb}(\text{Zr},\text{Ti})\text{O}_3$ . Lead zirconate titanate is currently one of the most studied and used materials for piezoelectric applications due to its Curie temperature, high dielectric constant, and high electromechanical coupling coefficient [31, 18, 32, 33].

The PZT ceramic which has the highest extensional and transverse strain constants is PZT-5H, followed by PZT-5J, and PZT-5A. Table 1.1 presents some relevant properties of PZT at room temperature.

Property	Units	PZT-5A	PZT-5H	PZT-5J
Planar coupling coefficient - $k_p$	-	0.68	0.75	0.72
Transverse coupling coefficient - $k_{31}$	-	0.35	0.44	0.37
Extensional coupling coefficient - $k_{33}$	-	0.72	0.75	0.74
Transverse strain constant - $d_{31}(10^{-12})$	m/V	-190	-320	-270
Extensional strain constant - $d_{33}(10^{-12})$	m/V	390	650	485
Transverse voltage constant - $g_{31}(10^{-3})$	Vm/N	-11.3	-9.5	-10.4
Extensional voltage constant - $g_{33}(10^{-3})$	Vm/N	23.2	19.0	21.3
Density - $\rho$	g/cm <sup>3</sup>	7.95	7.87	7.90

Table 1.1 PZT ceramics properties for room temperature (25°C). (Source:[1])

Due to their large piezoelectric and dielectric coefficients [33], PZT ceramics are used in many sensor [34], actuator [35, 36], and transducer applications [37, 38]. Since the discovery of the piezoelectric effect, huge advances have been made in studying crystals, ceramics, and their applications. More recently, engineers and scientists have been working on composite materials in order to fabricate them with piezoelectric properties, such as macrofiber composites [39]. Piezoelectrics are often referred to as smart materials [18], which when integrated into structures are referred to as smart structures [26, 40].

### 1.2.2 Piezoelectric Sensors

Piezoelectric sensors are devices which use the direct piezoelectric effect in order to measure changes in mechanical components like pressure, and generate an output signal [20, 17, 29, 19]. Applications of piezoelectric sensors mainly started after World War I, with the interest of measuring acceleration, pressure and force [20] and currently are widely used in applications such as in aerospace [41], medical [42] and nuclear engineering [43].

Piezoelectric sensors are commonly made using piezoelectric ceramics, natural crystals (such as quartz and tourmaline), synthetic crystals (like lithium niobate), and thin films. These sensors exhibit high stability, sensitivity, mechanical strength, and modulus of elasticity, among other favorable characteristics [20]. One specific type of sensor is the piezoelectric force sensor, which generates an electric charge output proportional to the applied input force [20]. A notable application of a piezoelectric force sensor was studied by Itoh and Suga, who developed a force sensor for an atomic force microscope (AFM) [44]. In the medical field, Curry et al. studied and proposed a biodegradable piezoelectric force sensor intended to measure and monitor biological forces such as brain and lung pressure. After obtaining the required measurements, this sensor can dissolve harmlessly within the body without causing any damage [45].

Another type of sensor is the piezoelectric pressure sensor which works in a similar way to the force sensor. Pressure sensors have a sensing element called a diaphragm which is responsible for transmitting the force to the sensor. This force is directly proportional to the applied pressure and an electric charge output is generated [20]. Piezoelectric pressure sensors are also widely used in many applications. Joshi et al. studied and designed a piezoelectric pressure sensor to measure the radial artery pulse [46], since the traditional method requires extensive training and may lead to false interpretations. Kim et al. have recently studied a piezoelectric pressure sensor based on flexible gallium nitride thin film for high temperature applications such as aerospace ( $-60^{\circ}\text{C}$  to  $900^{\circ}\text{C}$ ) and automotive ( $100^{\circ}\text{C}$  to  $350^{\circ}\text{C}$ ) [47].

Piezoelectric acceleration sensors are also widely used in engineering applications. The principle is the same as the piezoelectric force sensor, however, a seismic mass is attached to the sensor. When a mechanical force is applied to the structure and generates acceleration [48], the beam deforms and this creates strain in the piezoelectric structure, typically placed at the root of the beam, and then an electric signal output is generated [20, 49]. Zheng et. al studied how different types of piezoelectric acceleration sensors worked at high temperatures (above  $645^{\circ}\text{C}$ ), mainly for monitoring the vibration of engines [50].

### 1.2.3 Piezoelectric Actuators

Piezoelectric actuators are devices through which the converse piezoelectric effect generates a mechanical displacement when voltage is applied. They have a high power density, large frequency response, but typically produce very small strain [51, 52, 53]. Due to their high precision, piezoelectric actuators have been widely used in precise positioning applications [54, 55], piezoelectric motors [56], and microelectromechanical systems (MEMS) [57, 58, 59, 60]. Due to their small stroke, applications can be restricted [61], therefore, amplification mechanisms are often required in many applications.

According to Niezrecki [51], piezoelectric actuators can be classified according to their type of amplification mechanism as internally leveraged, externally leveraged, and frequency leveraged actuators [61]. Externally leveraged actuators rely on an external mechanical component to amplify a stroke, while internally leveraged actuators generate a stroke through the internal structure. Frequency-leveraged actuators utilize an alternating control signal to generate motion [51].

#### 1.2.3.1 Stack Actuators

Stack actuators are actuators in which piezoelectric slabs are “stacked” on top of each other in order to increase the longitudinal deflection when voltage is applied,

as shown in Fig. 1.6. The displacement and force are directly proportional to the length of the actuator and its cross sectional area [51, 52, 53]. Stack actuators are commonly used in applications which require high precision, such as precision positioning platforms, and vibration control [62, 63].

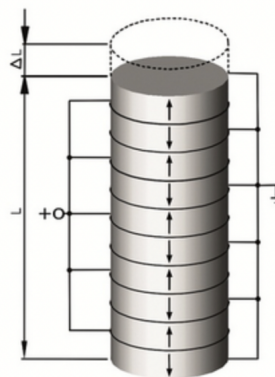


Fig. 1.6 Piezoelectric stack actuator. (Image source: [2])

Stack actuators can produce nominal displacements of 0.1% to 0.15% of their length, with blocking forces of around  $30 \text{ N/mm}^2$  relative to the cross-sectional area of the actuator [2]. Table 1.2 provides some commercial specifications for PICMA Stack Multilayer Piezo Actuators from *PI Ceramics* [2], at an operating voltage range from -20 to 120 V. The PICMA multilayer piezo actuator exhibits high response and force generation, and it demonstrated excellent performance and durability during tests conducted by NASA, retaining 96% of its original displacement after 100 billion cycles [2].

Piezo actuator model	Dimensions [mm]	Max. displacement [ $\mu\text{m}$ ]	Blocking force [N]
P-882.11	3×2×9	8	190
P-883.11	3×3×9	8	290
P-885.51	5×5×18	18	900
P-887.51	7×7×18	18	1750

Table 1.2 Piezoelectric stack actuator specifications. (Source:[2])

### 1.2.3.2 Bender Actuators

In bender actuators, one or more layers of piezoelectric ceramics are bonded together and a passive layer may also be included, as shown in the simple schematic of Fig. 1.7. The structure is called unimorph when only one layer of piezoceramic is present, and it is called bimorph when the structure has two layers of the piezoelectric ceramics. When the structure has more than two layers, it is typically referred to as a multimorph [51, 64, 53, 65]. Bender actuators provide a larger mechanical deflection in response to the applied voltage than stack actuators, however, bender actuators show a much smaller blocked force [51, 52, 53, 64].

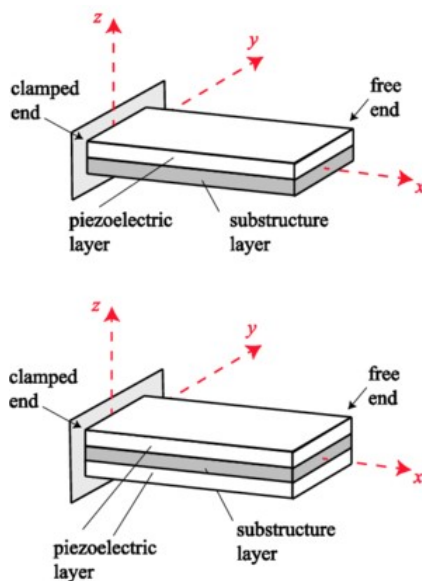


Fig. 1.7 Unimorph and bimorph structures. (Image source: [10])

Series and parallel connections are used in the fabrication of bimorph and multimorph actuators, as shown in Fig. 1.8 and Fig. 1.9. When a series connection is implemented, the piezoelectric layers have opposite polarization, and the electric field is applied along the total thickness of the bender. In parallel connections, the layers polarization is in the same direction, and the electric field is now applied to each separate plate with opposite polarity (see Fig. 1.9) [64]. As the electric field is applied in parallel to only one plate and in anti parallel to the other, one layer expands and the other contracts due to the transverse strain, generating bending in the structure [51, 64].

In multilayer bender actuators, typically the middle layers have the same polar-

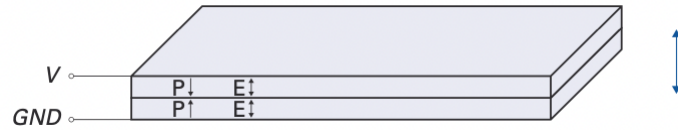


Fig. 1.8 Bimorph series connection. (Image source: [2])

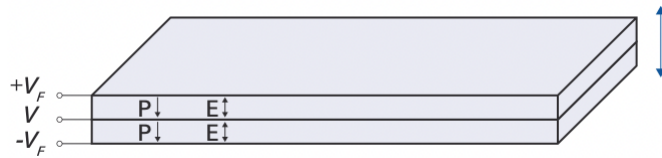


Fig. 1.9 Bimorph parallel connection. (Image source: [2])

ization direction, while the top and bottom layers have the same polarity in relation to each other, but are opposite in relation to the middle layers, as shown in the 4-layer bender actuator in Fig. 1.10.

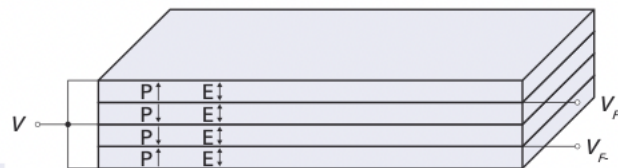


Fig. 1.10 Multimorph actuator. (Image source: [2])

Generally, bender actuators produce large physical displacements under smaller applied voltage, as in the PICMA Bender Piezo Actuator PL140.10, from *PI Ceramics*, which can produce a stroke of 1000  $\mu\text{m}$  under an operating voltage of 0-60 V. Table 1.3 shows some commercial specifications of rectangular bender actuators,

from *PI Ceramics* for an operating voltage of 0-60 V. Furthermore, it shows that bender actuators provide a large displacement, however with very small blocking forces as compared to stacks [2].

Piezo bender actuator model	Dimensions [mm]	Displacement [ $\mu\text{m}$ ]	Blocking force [N]
PL122.10	25×9.6×0.67	± 250	± 1.1
PL127.10	31×9.6×0.67	± 450	± 1.0
PL140.10	45×11×0.55	± 1000	± 0.5

Table 1.3 Piezo bender actuator specifications from *PI Ceramics* [2]

### 1.3 Linear Theory of Piezoelectricity

The IEEE Standard on Piezoelectricity [66] provides a general linear theory of piezoelectricity where the material properties are assumed as constants regardless of the magnitude of the applied mechanical stresses and electrical fields. The constitutive equations of a piezoelectric material can be introduced following the assumption that the total strain is the sum of the mechanical strain caused by the mechanical stress and the actuation strain generated by the applied voltage [67].

The constitutive equations of piezoelectricity in strain-charge tensor form is given as [66]

$$S_{ij} = s_{ijkl}^E T_{kl} + d_{kij} E_k \quad (1.2)$$

$$D_i = d_{ikl} T_{kl} + \varepsilon_{ij}^T E_k \quad (1.3)$$

where  $S_{ij}$  is the strain tensor,  $s_{ijkl}^E$  is the compliance tensor (where the superscript  $E$  denotes measured at constant electric field),  $T_{kl}$  is the stress tensor,  $d_{kij}$  and  $d_{ikl}$  are the piezoelectric tensors, and  $E_k$  represents the electric field. The electric displacement is denoted as  $D_i$ , and  $\varepsilon_{ij}^T$  (where the superscript  $T$  denotes measured at constant stress) represents the dielectric constants. Eq. (1.2) corresponds to the converse piezoelectric effect, and Eq. (1.3) represents the direct piezoelectric effect.

It is possible to rewrite the constitutive equations (Eqs. (1.2)-(1.3)) in engineering notation form as

$$S = s^E \sigma + dE \quad (1.4)$$

$$D = d^T \sigma + \varepsilon^\sigma E \quad (1.5)$$

where  $S$  is the strain vector,  $s^E$  is the matrix of compliance constants and it is given in  $\text{m}^2/\text{N}$ ,  $\sigma$  is the stress vector in  $\text{N}/\text{m}^2$ ,  $d$  represents the piezoelectric strain matrix in  $\text{m}/\text{V}$ , in which the superscript  $T$  denotes the transpose of the matrix,  $E$  is the applied electric field vector in  $\text{V}/\text{m}$ ,  $D$  is the electric displacement vector given in  $\text{C}/\text{m}^2$ , and  $\varepsilon^\sigma$  corresponds to the matrix of permittivity constants in  $\text{F}/\text{m}$ .

In full matrix form, Eqs. (1.4)-(1.5) become

$$\begin{bmatrix} S_1 \\ S_2 \\ S_3 \\ S_4 \\ S_5 \\ S_6 \end{bmatrix} = \begin{bmatrix} s_{11}^E & s_{12}^E & s_{13}^E & s_{14}^E & s_{15}^E & s_{16}^E \\ s_{21}^E & s_{22}^E & s_{23}^E & s_{24}^E & s_{25}^E & s_{26}^E \\ s_{31}^E & s_{32}^E & s_{33}^E & s_{34}^E & s_{35}^E & s_{36}^E \\ s_{41}^E & s_{42}^E & s_{43}^E & s_{44}^E & s_{45}^E & s_{46}^E \\ s_{51}^E & s_{52}^E & s_{53}^E & s_{54}^E & s_{55}^E & s_{56}^E \\ s_{61}^E & s_{62}^E & s_{63}^E & s_{64}^E & s_{65}^E & s_{66}^E \end{bmatrix} \begin{bmatrix} \sigma_1 \\ \sigma_2 \\ \sigma_3 \\ \sigma_4 \\ \sigma_5 \\ \sigma_6 \end{bmatrix} + \begin{bmatrix} d_{11} & d_{21} & d_{31} \\ d_{12} & d_{22} & d_{32} \\ d_{13} & d_{23} & d_{33} \\ d_{14} & d_{24} & d_{34} \\ d_{15} & d_{25} & d_{35} \\ d_{16} & d_{26} & d_{36} \end{bmatrix} \begin{bmatrix} E_1 \\ E_2 \\ E_3 \end{bmatrix} \quad (1.6)$$

$$\begin{bmatrix} D_1 \\ D_2 \\ D_3 \end{bmatrix} = \begin{bmatrix} d_{11} & d_{12} & d_{13} & d_{14} & d_{15} & d_{16} \\ d_{21} & d_{22} & d_{23} & d_{24} & d_{25} & d_{26} \\ d_{31} & d_{32} & d_{33} & d_{34} & d_{35} & d_{36} \end{bmatrix} \begin{bmatrix} \sigma_1 \\ \sigma_2 \\ \sigma_3 \\ \sigma_4 \\ \sigma_5 \\ \sigma_6 \end{bmatrix} + \begin{bmatrix} \varepsilon_{11}^\sigma & \varepsilon_{12}^\sigma & \varepsilon_{13}^\sigma \\ \varepsilon_{21}^\sigma & \varepsilon_{22}^\sigma & \varepsilon_{23}^\sigma \\ \varepsilon_{31}^\sigma & \varepsilon_{32}^\sigma & \varepsilon_{33}^\sigma \end{bmatrix} \begin{bmatrix} E_1 \\ E_2 \\ E_3 \end{bmatrix} \quad (1.7)$$

For a transversely isotropic piezoelectric material, such as PZT, the matrices can be reduced to

$$\begin{bmatrix} S_1 \\ S_2 \\ S_3 \\ S_4 \\ S_5 \\ S_6 \end{bmatrix} = \begin{bmatrix} s_{11}^E & s_{12}^E & s_{13}^E & 0 & 0 & 0 \\ s_{12}^E & s_{11}^E & s_{13}^E & 0 & 0 & 0 \\ s_{13}^E & s_{13}^E & s_{33}^E & 0 & 0 & 0 \\ 0 & 0 & 0 & s_{44}^E & 0 & 0 \\ 0 & 0 & 0 & 0 & s_{44}^E & 0 \\ 0 & 0 & 0 & 0 & 0 & 2(s_{11}^E - s_{12}^E) \end{bmatrix} \begin{bmatrix} \sigma_1 \\ \sigma_2 \\ \sigma_3 \\ \sigma_4 \\ \sigma_5 \\ \sigma_6 \end{bmatrix} + \begin{bmatrix} 0 & 0 & d_{31} \\ 0 & 0 & d_{31} \\ 0 & 0 & d_{33} \\ 0 & d_{15} & 0 \\ d_{15} & 0 & 0 \\ 0 & 0 & 0 \end{bmatrix} \begin{bmatrix} E_1 \\ E_2 \\ E_3 \end{bmatrix} \quad (1.8)$$

$$\begin{bmatrix} D_1 \\ D_2 \\ D_3 \end{bmatrix} = \begin{bmatrix} 0 & 0 & 0 & 0 & d_{15} & 0 \\ 0 & 0 & 0 & d_{15} & 0 & 0 \\ d_{31} & d_{31} & d_{33} & 0 & 0 & 0 \end{bmatrix} \begin{bmatrix} \sigma_1 \\ \sigma_2 \\ \sigma_3 \\ \sigma_4 \\ \sigma_5 \\ \sigma_6 \end{bmatrix} + \begin{bmatrix} \varepsilon_{11}^\sigma & 0 & 0 \\ 0 & \varepsilon_{11}^\sigma & 0 \\ 0 & 0 & \varepsilon_{33}^\sigma \end{bmatrix} \begin{bmatrix} E_1 \\ E_2 \\ E_3 \end{bmatrix} \quad (1.9)$$

## 1.4 Thermopiezoelectricity

Thermopiezoelectricity takes into account the thermal field in addition to the mechanical and electrical fields. As a result, the coupling effects among these three fields must be considered, including the pyroelectric and electrocaloric effects.

Several studies have been conducted on thermopiezoelectricity and, in 1974, Mindlin derived the governing equations of a linear piezothermoelastic medium [68].

In 1978, Nowacki presented the theorem for the solutions of piezothermoelastic differential equations [69]. Nowacki also investigated the influence of a temperature field on an elastic dielectric medium in 1982 [70]. Chandrasekharaiah worked on thermopiezoelectricity, in 1984, presenting equations for a temperature rate theory of thermopiezoelectricity [71]. These equations predicted a finite speed of propagation of the thermal field. Additionally, in 1988, Chandrasekharaiah conducted a research on generalized linear thermoelasticity theory for piezoelectric materials obtaining an equation of energy balance and a theorem on the uniqueness of the solution [72]. Rao and Sunar studied the thermopiezoelectric sensors and actuators in advanced intelligent structures, in 1993, in which they used a finite element formulation to analyse the problem [73]. One year later, Tzou and Howard investigated the use of a piezothermoelastic shell vibration theory for applications in active structures [74], and Tzou and Ye studied the piezothermoelastic effects of distributed piezoelectric sensors/actuators in structural systems [75]. Yang and Batra investigated the effect of heat conduction on the shift in frequencies of a vibrating linear piezoelectric body in 1995 [76]. Two methods were used in the research, one involving the thermal conductivity and the other involving the thermocoupling constants. In 2000, Fung et al. analysed the dynamics of a piezothermoelastic resonator with several shapes [77]. In 2002, Görnandt and Gabbert proposed a finite element implementation for thermopiezoelectric smart structures in order to solve

the coupled field problem [4]. In 2003, Ashida and Tauchert conducted a study on thermally-induced wave propagation in a piezoelectric plate using the Laplace transform technique, considering thermal relaxation time, which is the amount of time that a material takes to return to ambient temperature following heating [78]. The analyses demonstrated that the relaxation time significantly influenced the stresses, displacements and electric potential difference across the plate, however, it had small consequences in the temperature field. Tian et al. proposed in 2007 a finite element method for generalized piezothermoelastic problems [79]. In 2012, Al-shaikh developed a mathematical modelling for the influence of initial stresses and relaxation time on reflection and refraction waves in a thermopiezoelectric media [80].

Following [4], the governing constitutive equations for a thermopiezoelectric material can be written as

$$T_{ij} = C_{ijkl}u_{kl} - e_{kij}E_k - \zeta_{ij}\theta \quad (1.10)$$

$$D_i = e_{ijk}u_{jk} + \varepsilon_{ij}E_j + p_i\theta \quad (1.11)$$

$$\eta = \zeta_{ij}u_{ij} + p_iE_i + \lambda\theta \quad (1.12)$$

where  $T_{ij}$ ,  $D_i$ , and  $\eta$  are defined as the stress tensor, electric displacement, and entropy density, respectively. The terms  $C_{ijkl}$ ,  $e_{kij}$  and  $\varepsilon_{ij}$  are the elastic compliance, piezoelectric, and dielectric permittivity coefficients. The term  $\zeta_{ij}\theta$  in Eq. (2.15) is

related to the thermal stress via  $\zeta_{ij}$  which is defined as the temperature-stress coefficient, where  $\theta$  is a small temperature change. The term  $p_i\theta$  in Eq. (2.16) is the pyroelectric term, where  $p_i$  is defined as the pyroelectric constant [81, 82]. The term  $\zeta_{ij}u_{ij}$  in Eq. (2.17) stands for the heat of deformation (thermal-mechanical coupling),  $p_iE_i$  is the electrocaloric effect (thermal-electrical coupling effect), and the coefficient  $\lambda$  is defined as  $\rho C_v^E/\Theta_0$ , where  $C_v^E$  is the specific heat capacity, and  $\Theta_0$  is the reference temperature, that is the point with no thermal strains [81, 82, 26].

In many applications, such as in the aerospace field, the thermal effects influence the behavior of piezoelectric actuators and structures. More recent studies have been conducted by Elahi et al., such as a thermopiezoelectric energy harvester for a reconnaissance satellite structure [83], and in 2021, Elahi [84] investigated the structural health monitoring of aerospace structures through piezoelectric aeroelastic energy harvesting [84].

## 1.5 Research Objectives and Contributions

The objective of this research is to investigate the influence of these effects on piezoelectric actuators and predict their behavior in environments where thermal fields play an important role. Moreover, it is of interest to determine whether the pyroelectric and electrocaloric effects exert a significant impact on the analyzed actuators in comparison to simulations that do not consider these coefficients.

Coefficient	ABAQUS 2021	ANSYS 2021	COMSOL 6.0
Piezoelectric	✓	✓	✓
Pyroelectric	x	x	✓
Electrocaloric	x	x	✓
Fully coupled effects	x	x	x

Table 1.4 A comparison of the capabilities of commercial software

There are currently no commercial finite element software codes available that include both the pyroelectric and electrocaloric effects in a fully-coupled implementation (see Table 1.4). To investigate the thermopiezoelectric effect in piezoelectric actuators, a finite element code is implemented in MATLAB that considers the three fully-coupled field equations of thermopiezoelectricity. Both static and dynamic cases are analyzed for piezoelectric bender and stack actuators, simulating thermal conditions that could occur in varying external environments.

For this investigation, the development of the code is divided into four parts. The first step is to implement a finite element code for a three dimensional solid element, then for a piezoelectric element. The third step is to implement a finite element code for a thermoelastic element, and finally the last step is the implementation for a thermopiezoelectric element.

In the literature there are studies on thermopiezoelectricity and how the coupled three-field problem (mechanical, electrical, thermal) can be solved numerically, for static and dynamic cases. Gornandt and Gabbert [4], for instance, presented

the weak form of the fully coupled thermopiezoelectric field equations, and investigated static and dynamic cases, in which it was demonstrated that a change in temperature exerted an impact on the structures behaviour. These results focused on structural and sensing applications, and did not consider actuators. This thesis focuses on actuators as it is known that driving causes self-heating in actuators and a drift in their position, however it has not been studied with a fully coupled three-field model.

This research will provide a quantification of the coupling effects on piezoelectric actuators in dynamic applications, and the prediction of their behaviour will open the door to a deeper understating of how these effects impact the actuators and allow more complex models to be implemented.

The objectives of this research can be summarized as:

1. Implement a finite element code in MATLAB to numerically solve the three fully-coupled field equations of thermopiezoelectricity for simulations of piezoelectric actuators under environments in which the thermal field plays an important role.
2. Investigate and quantify the influence that the electric field has on the temperature, and how the temperature affects the positioning and dynamic performance of these actuators.

3. Predict the behaviour of piezoelectric actuators when temperature is considered and the piezoelectric strain coefficients are temperature dependent.

## 1.6 Organization

This thesis is divided into six main parts beginning with the presentation of the finite element formulation of the constitutive equations of thermopiezoelectricity and the verification of the code in Chapter 2. This begins with a description of the finite element method, covering isoparametric formulation, classical shape functions, high-order shape functions, Gaussian quadrature, thermopiezoelectric finite element formulation, boundary conditions, static, modal, and dynamic solutions. The verification process starts with a three dimensional solid element, proceeds to a piezoelectric element, and finally includes a thermoelastic element by comparing the results with ABAQUS and with benchmarks. Two benchmarks are investigated: a piezoelectric problem proposed by Tzou [85], and a thermopiezoelectric problem proposed by Tauchert [86] and further investigated by Gornandt and Gabbert [4]. Chapter 3 focuses on the simulations of multilayer stack actuators. This Chapter introduces stack actuators, alongside the model that is used in the simulations. The stack actuator, with different numbers of layers, is analyzed for a step input signal, a sinusoidal input, and a thermal load. Chapter 4 discusses the analysis of multimorph bender actuators. The actuator is simulated for a step input signal,

a sinusoidal input, and a thermal load. Chapter 5 revisits the simulations analyzed in Chapter 3 and 4, with consideration of the temperature dependence of the piezoelectric strain coefficients  $d_{31}$  and  $d_{33}$ . The chapter discusses the differences between piezoelectric simulations and simulations using temperature-independent coefficients, as well as results that incorporate temperature-dependent piezoelectric strain coefficients  $d_{31}$  and  $d_{33}$ . To conclude Chapter 5, a realistic case study for bender actuators is analyzed. This scenario considers the temperature variations experienced for a piezoelectrically-actuated instrument on a stratospheric balloon flight that includes convection, and a multi-step scan across the actuation range with the consideration of the temperature-dependent coefficient  $d_{31}$ . The analysis compares piezoelectric, thermopiezoelectric with temperature-independent coefficient  $d_{31}$ , thermopiezoelectric with temperature-independent coefficient  $d_{31}$  while neglecting the pyroelectric and electrocaloric effects, and thermopiezoelectric simulations with temperature-dependent coefficient  $d_{31}$ . Finally, Chapter 6 concludes the thesis by summarizing the findings of the research and presenting directions for future work.

## 2 Finite Element Implementation and Verification

The finite element implementation is the process of translating the numerical principles and mathematical concepts of the finite element method into practical computer programs. It involves numerically formulating the problem which results in a system of algebraic equations for the solution, partitioning the domain into smaller elements, choosing shape functions, assembling a global system of equations, applying boundary conditions to solve the equations, and performing model verification in the post-processing step.

The finite element equations of a physical system can be formulated using one of three main techniques. For structural analysis problems, these techniques include the direct equilibrium method, variation methods based on the principle of virtual work, and weighted residual method [21, 87, 6]. The direct equilibrium method is the simplest method and typically finds applications to derive the element stiffness matrices for 1D elements, such as trusses, springs, and beams. In structural

mechanics problems, two primary direct approaches are commonly employed. In one approach, referred to as the force (or flexibility) method, the unknowns of the problem are internal forces. The governing equations are obtained by first utilizing equilibrium equations, and additional necessary equations are then derived by introducing compatibility equations. The result is a set of algebraic equations used to determine the unknown forces. The second method, referred to as the displacement or stiffness method, takes into account the nodal displacements as the problem's unknowns. For instance, satisfaction of compatibility constraints demand that elements connected at a common node, along a common edge, or on a common surface, continue to be connected at that node, edge, or surface upon loading. The equilibrium equations and a relevant formula connecting forces to displacements are then used to translate the governing equations into terms of nodal displacements. Since it provides a more straightforward formulation for the majority of structural application problems, the displacement approach is used more frequently in commercial finite element programs [21, 87].

The variational approach is founded on the idea of minimizing a functional, a mathematical statement that includes the unknown field variable and its derivatives. In comparison to the direct method, the variational method makes it much simpler to derive the finite element equations for two and three-dimensional elements. It does, however, need the existence of a functional, whose minimization

results in the stiffness matrix and associated element equations. The functional reflects a physical quantity relevant to the system under study, such as the total energy produced by the external forces or potential energy. The principle of minimal potential energy, for instance, can be used as the functional for structural analysis problems because it is a relatively simple physical idea to comprehend.

In the weighted residual technique, an approximate solution to the equations is obtained by minimizing the difference between the original equations and the approximation. The equations are multiplied by weight functions to achieve this, and the domain is then integrated.

Any of these methods will result in equations that describe an element's behaviour. For the linear static case, these equations can be expressed in matrix form as

$$k^e u^e = f^e \tag{2.1}$$

where  $k^e$  is the element stiffness matrix which relates the nodal displacement vector  $u^e$  to the nodal forces vector  $f^e$  for a unique element  $e$ .

The element equations must be assembled into global equations. Without loss of generality, the global system of equations is given as

$$KU = F \tag{2.2}$$

where  $K$  is the global stiffness matrix,  $U$  is the vector of generalized displacements,

and  $F$  is the vector of global nodal forces. The global stiffness matrix  $K$  can be expressed as

$$K = \sum_{e=1}^n k^e \quad (2.3)$$

The vector of global nodal forces is given as

$$F = \sum_{e=1}^n f^e \quad (2.4)$$

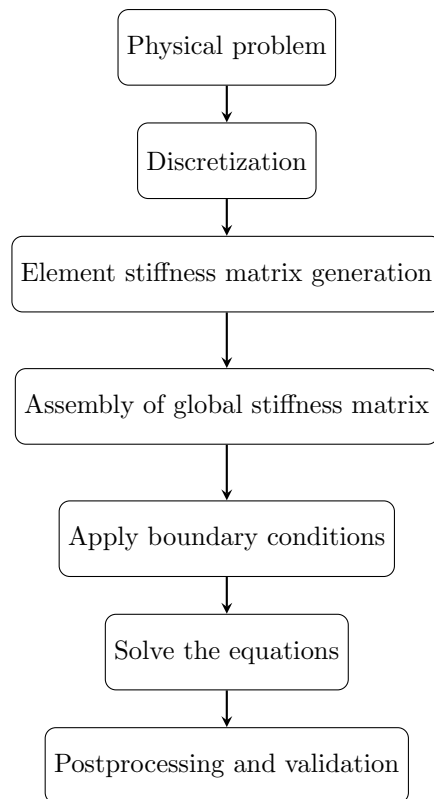


Fig. 2.1 Finite element analysis procedure

The typical technique used to solve for  $U$  involves taking the inverse of the

global stiffness matrix  $K$  and pre-multiplying it by the vector of global nodal forces  $F$ . A summary of the finite element analysis procedure for structural application problems that produces displacement solutions is shown in Fig. 2.1.

## 2.1 Classical Shape Functions

Shape functions are functions used to approximate the behaviour of physical quantities, such as displacement, within the elements. They interpolate the solution between the values obtained at the nodes polynomial. The value of a shape function at a specific node is one, whereas it is zero at the other nodes, where the sum of all shape functions is equal to one at any point [87, 21, 88, 89]. The most common types of shape functions include linear, quadratic, or higher-order shape functions, depending on what type of element is chosen in the discretization and its degree of freedom. An example of one-dimensional bar element is shown in Fig. 2.2.

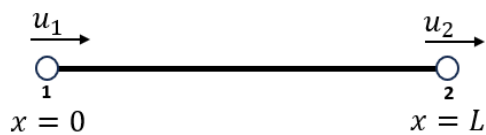


Fig. 2.2 Nodes and degrees of freedom of a bar element. (Image adapted from: [11])

For the one-dimensional bar element, the unknown variable  $u(x)$  can be written

as

$$u(x) = \left(1 - \frac{x}{L}\right) u_1 + \left(\frac{x}{L}\right) u_2 \quad (2.5)$$

where  $N_1 = \left(1 - \frac{x}{L}\right)$  is the first shape function (associated with node 1), and  $N_2 = \left(\frac{x}{L}\right)$  is the second shape function.

It is important to mention that the polynomial order of the shape function typically determines the accuracy of the approximation.

## 2.2 Isoparametric Formulation

The development of equations and element matrices in terms of a global coordinate system ( $x, y, z$  for 3D structures) becomes extremely challenging for complex elements and is typically not possible because all elements may have different geometry. Therefore, the isoparametric formulation was developed [90], which allows for elements to take on both straight lines and curved surfaces. The isoparametric formulation uses a natural coordinate reference system ( $\xi_1, \xi_2, \xi_3$  for 3D structures) which assigns coordinates to the nodes in a normalized interval, typically ranging from -1 to 1, and facilitates the evaluation of integrals in the natural coordinate domain. Furthermore, the application of the isoparametric formulation results in simpler and more efficient computer programs.

The relationship between the global and natural coordinate systems is referred to as transformation mapping, and it must be used in equation formulations to

compute the derivatives of the shape functions. The shape functions are defined in terms of the natural coordinates  $\xi_i$ , but their partial derivatives are with respect to Cartesian coordinates. Calculating these derivatives involves using the inverse of the Jacobian matrix and applying the chain rule. This process of coordinate transformation through the Jacobian matrix is demonstrated for a shape function  $N$  as

$$\begin{bmatrix} \frac{\partial N^{(i)}}{\partial \xi_1} \\ \frac{\partial N^{(i)}}{\partial \xi_2} \\ \frac{\partial N^{(i)}}{\partial \xi_3} \end{bmatrix} = \underbrace{\begin{bmatrix} \frac{\partial x}{\partial \xi_1} & \frac{\partial y}{\partial \xi_1} & \frac{\partial z}{\partial \xi_1} \\ \frac{\partial x}{\partial \xi_2} & \frac{\partial y}{\partial \xi_2} & \frac{\partial z}{\partial \xi_2} \\ \frac{\partial x}{\partial \xi_3} & \frac{\partial y}{\partial \xi_3} & \frac{\partial z}{\partial \xi_3} \end{bmatrix}}_J \begin{bmatrix} \frac{\partial N^{(i)}}{\partial x} \\ \frac{\partial N^{(i)}}{\partial y} \\ \frac{\partial N^{(i)}}{\partial z} \end{bmatrix} \Rightarrow \begin{bmatrix} \frac{\partial N^{(i)}}{\partial x} \\ \frac{\partial N^{(i)}}{\partial y} \\ \frac{\partial N^{(i)}}{\partial z} \end{bmatrix} = J^{-1} \begin{bmatrix} \frac{\partial N^{(i)}}{\partial \xi_1} \\ \frac{\partial N^{(i)}}{\partial \xi_2} \\ \frac{\partial N^{(i)}}{\partial \xi_3} \end{bmatrix} \quad (2.6)$$

where  $J$  is the Jacobian matrix,  $J^{-1}$  is the inverse of the Jacobian matrix, and  $|J|$  is denominated as the determinant of the Jacobian, which is given as

$$|J| = \frac{\partial x}{\partial \xi_1} \begin{bmatrix} \frac{\partial y}{\partial \xi_2} & \frac{\partial z}{\partial \xi_2} \\ \frac{\partial y}{\partial \xi_3} & \frac{\partial z}{\partial \xi_3} \end{bmatrix} - \frac{\partial y}{\partial \xi_1} \begin{bmatrix} \frac{\partial x}{\partial \xi_2} & \frac{\partial z}{\partial \xi_2} \\ \frac{\partial x}{\partial \xi_3} & \frac{\partial z}{\partial \xi_3} \end{bmatrix} + \frac{\partial z}{\partial \xi_1} \begin{bmatrix} \frac{\partial x}{\partial \xi_2} & \frac{\partial y}{\partial \xi_2} \\ \frac{\partial x}{\partial \xi_3} & \frac{\partial y}{\partial \xi_3} \end{bmatrix} \quad (2.7)$$

## 2.3 Higher-Order Shape Functions

Higher-order element shape functions can be created by adding more nodes to the sides of the linear element. For the one-dimensional example shown in Fig. 2.2, an additional node can be implemented (see Fig 2.3), resulting in higher-order (or quadratic) shape functions.

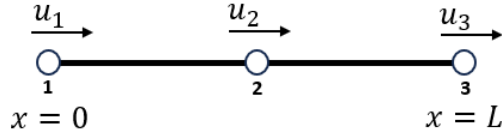


Fig. 2.3 Nodes and degrees of freedom of bar element: quadratic or higher-order shape function. (Source: [12])

The unknown variable  $u(x)$  is now given as

$$u(x) = \left(1 - \frac{3x}{L} + \frac{2x^2}{L^2}\right) u_1 + \left(\frac{4x}{L} - \frac{4x^2}{L^2}\right) u_2 + \left(-\frac{x}{L} + \frac{2x^2}{L^2}\right) u_3 \quad (2.8)$$

where  $N_1 = \left(1 - \frac{3x}{L} + \frac{2x^2}{L^2}\right)$  is the first shape function,  $N_2 = \left(\frac{4x}{L} - \frac{4x^2}{L^2}\right)$  is the second shape function, and  $N_3 = \left(-\frac{x}{L} + \frac{2x^2}{L^2}\right)$  is the third shape function.

For three-dimensional elements, higher-order shape functions are often used. With fewer elements, convergence to the exact solution happens more quickly because these elements produce higher-order strain variations within each element [21, 87]. Fig. 2.4 shows a reference 20-noded hexahedral element in the natural coordinates  $(-1 \leq \xi_1 \leq 1, -1 \leq \xi_2 \leq 1, -1 \leq \xi_3 \leq 1)$ .

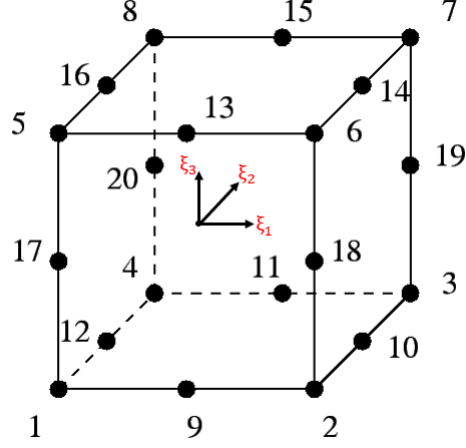


Fig. 2.4 Reference 20-noded hexahedral element ( $-1 \leq \xi_1 \leq 1, -1 \leq \xi_2 \leq 1, -1 \leq \xi_3 \leq 1$ ). (Image adapted from: [13])

The shape functions for the 20-noded hexahedral element are given as

- For the edge nodes  $j = 1, 2, 3, 4, 5, 6, 7, 8$ :

$$N_j = \frac{1}{8}(1 + \xi_1^{(j)} \xi_1)(1 + \xi_2^{(j)} \xi_2)(1 + \xi_3^{(j)} \xi_3)(\xi_1^{(j)} \xi_1 + \xi_2^{(j)} \xi_2 + \xi_3^{(j)} \xi_3 - 2) \quad (2.9)$$

- For the midside nodes  $j = 9, 11, 13, 15$ :

$$N_j = \frac{1}{4}(1 - \xi_1^2)(1 + \xi_2^{(j)} \xi_2)(1 + \xi_3^{(j)} \xi_3) \quad (2.10)$$

- For the midside nodes  $j = 10, 12, 14, 16$ :

$$N_j = \frac{1}{4}(1 - \xi_2^2)(1 + \xi_1^{(j)} \xi_1)(1 + \xi_3^{(j)} \xi_3) \quad (2.11)$$

- For the midside nodes  $j = 17, 18, 19, 20$ :

$$N_j = \frac{1}{4}(1 - \xi_3^2)(1 + \xi_1^{(j)}\xi_1)(1 + \xi_2^{(j)}\xi_2) \quad (2.12)$$

## 2.4 Gaussian Quadrature

Gaussian quadrature is a numerical method to solve definite integrals. In finite element analysis, it is considered one of the most useful methods for numerical evaluation of integrals [21]. Gaussian quadrature relies on evaluating a function  $y(\xi)$  at  $n$  different specific sampling points  $\xi_i$ , where each function evaluation  $y(\xi_i)$  is multiplied by the corresponding weight  $W_i$  and summed to obtain an approximation of the integral [6]. Without loss of generality, Gaussian quadrature approximates the integral on a reference domain  $[-1, 1]$ . The formula for a one-dimensional case is given as

$$I = \int_{-1}^1 y(\xi) d\xi \approx \sum_{i=1}^n W_i y(\xi_i) \quad (2.13)$$

The position of Gaussian points and their corresponding weights are given in Table 2.1, for one, two, and three sampling points.

In general, Gaussian quadrature provides exact integration for polynomials up to order  $2m - 1$ , where  $m$  is the order of the polynomial [21]. However, if the function  $y(\xi)$  is not a polynomial, Gaussian quadrature becomes an approximation rather than an exact solution, where the accuracy of the approximation of the solution is

Number of points $n$	Locations, $\xi_i$	Weights, $W_i$
1	$\xi_1 = 0$	2
2	$\xi_1 = \xi_2 = \pm \sqrt{\frac{1}{3}}$	1
3	$\xi_1 = \xi_3 = \pm \frac{\sqrt{15}}{5}$	5/9
	$\xi_2 = 0$	8/9

Table 2.1 Gaussian points and weights

increased by using more Gauss points [21, 6, 87].

As the Gaussian quadrature formulation is described in a natural reference system with coordinates  $\xi_i$ , where the coordinates can vary between -1 and 1, an example of the Gauss points for one-dimensional, two-dimensional, and three-dimensional structures in this natural coordinate system is demonstrated in Fig. 2.5.

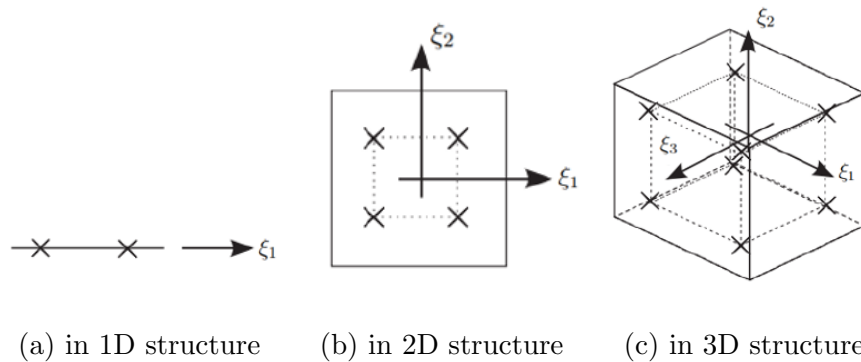


Fig. 2.5 Illustration of the location of Gauss points. (Image adapted from: [6])

The one-dimensional quadrature rule can naturally be extended to three dimensions and is given as

$$I = \int_{-1}^1 \int_{-1}^1 \int_{-1}^1 y(\xi_1, \xi_2, \xi_3) d\xi_1 d\xi_2 d\xi_3 = \sum_{i=1}^n \sum_{j=1}^n \sum_{k=1}^n y(\xi_i, \xi_j, \xi_k) W_i W_j W_k \quad (2.14)$$

The number of Gauss points used to integrate the function defines whether the integration is considered full integration or reduced integration. For a 20-noded hexahedral element (brick element), full integration has 3 points in each direction ( $3 \times 3 \times 3$ ), therefore 27 points are evaluated for the integration, as shown in Fig. 2.6. For the reduced integration of the 20-noded hexahedral element, only 2 points are needed in each direction ( $2 \times 2 \times 2$ ), therefore 8 points are needed (see Fig. 2.7), which drastically reduces the computational time to run simulations.

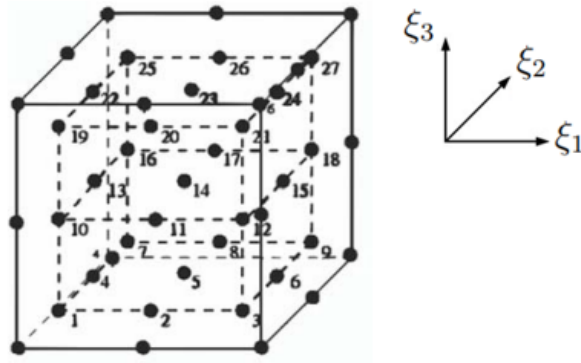


Fig. 2.6 Example of Gaussian quadrature full integration of a 20-noded hexahedral element. (Image adapted from: [14])

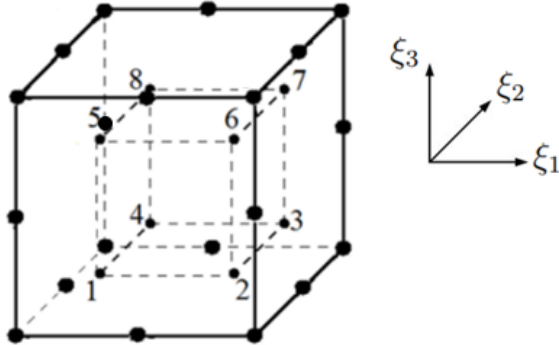


Fig. 2.7 Example of Gaussian quadrature reduced integration of 20-noded hexahedral element. (Image adapted from: [14])

The 20-noded hexahedral element with reduced integration is typically the best choice for most general stress/displacement simulations [3, 21]. The 20-noded hexahedral element with reduced integration (C3D20R) also provides more consistent and accurate results than the full integration element (C3D20) in comparison with the analytical results for the deflection of a beam, as shown in Table 2.2. Thus, for most simulations in this thesis unless otherwise noted, the reduced integration 20-noded hexahedral element is employed.

Element type	Depth x Mesh			
	1×4	2×4	4×4	8×16
C3D20	0.987	0.987	0.988	1.000
C3D20R	1.001	1.001	1.001	1.001

Table 2.2 Normalized tip deflection of a cantilever beam ( $w_{fem}/w_{exact}$ ) as compared to the Bernoulli-Euler theory prediction for a reference problem. (Source:[3])

## 2.5 Thermopiezoelectric Finite Element Formulation

The governing constitutive equations for a thermopiezoelectric material are given as [4]

$$T_{ij} = C_{ijkl}u_{kl} - e_{kij}E_k - \zeta_{ij}\theta \quad (2.15)$$

$$D_i = e_{ijk}u_{jk} + \varepsilon_{ij}E_j + p_i\theta \quad (2.16)$$

$$\eta = \zeta_{ij}u_{ij} + p_iE_i + \lambda\theta \quad (2.17)$$

where  $T_{ij}$ ,  $D_i$ , and  $\eta$  are defined as the stress tensor, electric displacement, and entropy density, respectively. The terms  $C_{ijkl}$ ,  $e_{kij}$ ,  $\varepsilon_{ij}$ , and  $E$  are the elastic compliance, piezoelectric matrix, dielectric permittivity matrix, and the electric field, respectively. The temperature-stress coefficient is defined as  $\zeta_{ij}$ , and  $\theta$  is a small temperature change, therefore the term  $\zeta_{ij}\theta$  in Eq. (2.15) is described as the thermal stress. The pyroelectric matrix is defined as  $p_i$ , where the term  $p_i\theta$ , in Eq. (2.16), stands for pyroelectricity [81, 82]. The term  $\zeta_{ij}u_{ij}$  in Eq. (2.17) stands for the heat of deformation (thermal-mechanical coupling),  $p_iE_i$  is the electrocaloric ef-

fect (thermal-electrical coupling effect), and the coefficient  $\lambda$  is defined as  $\rho C_v^E / \Theta_0$ , where  $C_v^E$  is the specific heat capacity, and  $\Theta_0$  is the reference temperature, that is the point without thermal strain [81, 82, 26].

The field variables for a thermopiezoelectric finite element  $(u, \phi, \theta)$ , where  $u$  stands for mechanical displacement,  $\phi$  represents electric potential, and  $\theta$  denotes temperature, can be approximated by the shape functions  $N_u$  (mechanical),  $N_\phi$  (electrical), and  $N_\theta$  (thermal), along with the unknown nodal degrees of freedom  $u^e$ ,  $\phi^e$ , and  $\theta^e$ . The field variable  $u$  corresponds to the mechanical degrees of freedom and is represented as a vector with dimensions of  $60 \times 1$  for a 20-noded hexahedral element, as each node has three mechanical degrees of freedom. The field variable associated with electrical degrees of freedom is  $\phi$ , which is a vector with dimensions of  $20 \times 1$  for a 20-noded hexahedral element, as there is only one electrical degree of freedom per node. Since there is one degree of freedom per node for the thermal field,  $\theta$  is a vector with dimensions of  $20 \times 1$  for a 20-noded hexahedral element. The shape functions for a 20-noded hexahedral element related to mechanical degrees of freedom form a matrix with dimensions of  $3 \times 60$ , while the shape functions associated with electrical and thermal degrees of freedom are matrices with dimensions of  $1 \times 20$ . The shape functions  $N_u^{(1)}$  through  $N_u^{(20)}$  are defined as in the shape functions

related to the mechanical field, and can be described as

$$N_u = \begin{bmatrix} N_u^{(1)} & 0 & 0 & N_u^{(2)} & 0 & 0 & \dots & 0 \\ 0 & N_u^{(1)} & 0 & 0 & N_u^{(2)} & 0 & \dots & 0 \\ 0 & 0 & N_u^{(1)} & 0 & 0 & N_u^{(2)} & \dots & N_u^{(20)} \end{bmatrix} \quad (2.18)$$

The shape functions matrix related to the electrical field can be written as

$$N_\phi = \begin{bmatrix} N_\phi^{(1)} & N_\phi^{(2)} & \dots & N_\phi^{(20)} \end{bmatrix} \quad (2.19)$$

Similarly, the shape functions matrix related to the thermal field can be described as

$$N_\theta = \begin{bmatrix} N_\theta^{(1)} & N_\theta^{(2)} & \dots & N_\theta^{(20)} \end{bmatrix} \quad (2.20)$$

The relation of the field variables  $u$ ,  $\phi$ ,  $\theta$ , shape functions  $N_u$ ,  $N_\phi$ ,  $N_\theta$ , and unknown degrees of freedom  $u^e$ ,  $\phi^e$ ,  $\theta^e$  can be formulated as

$$u = N_u(\xi_1, \xi_2, \xi_3)u^e \quad (2.21)$$

$$\phi = N_\phi(\xi_1, \xi_2, \xi_3)\phi^e \quad (2.22)$$

$$\theta = N_\theta(\xi_1, \xi_2, \xi_3)\theta^e \quad (2.23)$$

The gradient matrices, which relates the strain, electric potential, and temperature at each integration point to the unknown degrees of freedom  $u^e$ ,  $\phi^e$ ,  $\theta^e$ , respectively, are given as

$$B_u = D_u N_u$$

$$B_\phi = D_\phi N_\phi \quad (2.24)$$

$$B_\theta = D_\theta N_\theta$$

where  $D_u$ ,  $D_\phi$ , and  $D_\theta$  are the differential matrices in Cartesian coordinates  $x$ ,  $y$ , and  $z$

$$D_u = \begin{bmatrix} \frac{\partial}{\partial x} & 0 & 0 \\ 0 & \frac{\partial}{\partial y} & 0 \\ 0 & 0 & \frac{\partial}{\partial z} \\ \frac{\partial}{\partial y} & \frac{\partial}{\partial x} & 0 \\ 0 & \frac{\partial}{\partial z} & \frac{\partial}{\partial y} \\ \frac{\partial}{\partial z} & 0 & \frac{\partial}{\partial x} \end{bmatrix} \quad (2.25)$$

$$D_\phi = D_\theta = \begin{bmatrix} \frac{\partial}{\partial x} \\ \frac{\partial}{\partial y} \\ \frac{\partial}{\partial z} \end{bmatrix} \quad (2.26)$$

The gradient matrices for the mechanical, electrical, and thermal fields can now be described in extended matrix form. The  $i^{\text{th}}$  partition of the gradient matrix for the mechanical field  $B_u^{(i)}$  in general form is given as

$$B_u^{(i)} = \begin{bmatrix} \frac{\partial N_u^{(i)}}{\partial x} & 0 & 0 \\ 0 & \frac{\partial N_u^{(i)}}{\partial y} & 0 \\ 0 & 0 & \frac{\partial N_u^{(i)}}{\partial z} \\ \frac{\partial N_u^{(i)}}{\partial y} & \frac{\partial N_u^{(i)}}{\partial x} & 0 \\ 0 & \frac{\partial N_u^{(i)}}{\partial z} & \frac{\partial N_u^{(i)}}{\partial y} \\ \frac{\partial N_u^{(i)}}{\partial z} & 0 & \frac{\partial N_u^{(i)}}{\partial x} \end{bmatrix} \quad (2.27)$$

The general form of the gradient matrices for the electrical  $B_\phi^{(i)}$  and thermal  $B_\theta^{(i)}$  fields are written as

$$B_\phi^{(i)} = \begin{bmatrix} \frac{\partial N_\phi^{(i)}}{\partial x} \\ \frac{\partial N_\phi^{(i)}}{\partial y} \\ \frac{\partial N_\phi^{(i)}}{\partial z} \end{bmatrix} \quad (2.28)$$

$$B_\theta^{(i)} = \begin{bmatrix} \frac{\partial N_\theta^{(i)}}{\partial x} \\ \frac{\partial N_\theta^{(i)}}{\partial y} \\ \frac{\partial N_\theta^{(i)}}{\partial z} \end{bmatrix}$$

where  $i = 1, 2, \dots, n$  ( $n =$  number of nodes of the element).

For a 20-noded hexahedral element, Eq. (2.27) becomes

$$B_u = \begin{bmatrix} \frac{\partial N_u^{(1)}}{\partial x} & 0 & 0 & \frac{\partial N_u^{(2)}}{\partial x} & 0 & 0 & \frac{\partial N_u^{(3)}}{\partial x} & 0 & \dots & 0 \\ 0 & \frac{\partial N_u^{(1)}}{\partial y} & 0 & 0 & \frac{\partial N_u^{(2)}}{\partial y} & 0 & 0 & \frac{\partial N_u^{(3)}}{\partial y} & \dots & 0 \\ 0 & 0 & \frac{\partial N_u^{(1)}}{\partial z} & 0 & 0 & \frac{\partial N_u^{(2)}}{\partial z} & 0 & 0 & \dots & \frac{\partial N_u^{(20)}}{\partial z} \\ \frac{\partial N_u^{(1)}}{\partial y} & \frac{\partial N_u^{(1)}}{\partial x} & 0 & \frac{\partial N_u^{(2)}}{\partial y} & \frac{\partial N_u^{(2)}}{\partial x} & 0 & \frac{\partial N_u^{(3)}}{\partial y} & \frac{\partial N_u^{(3)}}{\partial x} & \dots & 0 \\ 0 & \frac{\partial N_u^{(1)}}{\partial z} & \frac{\partial N_u^{(1)}}{\partial y} & 0 & \frac{\partial N_u^{(2)}}{\partial z} & \frac{\partial N_u^{(2)}}{\partial y} & 0 & \frac{\partial N_u^{(3)}}{\partial z} & \dots & \frac{\partial N_u^{(20)}}{\partial y} \\ \frac{\partial N_u^{(1)}}{\partial z} & 0 & \frac{\partial N_u^{(1)}}{\partial x} & \frac{\partial N_u^{(2)}}{\partial z} & 0 & \frac{\partial N_u^{(2)}}{\partial x} & \frac{\partial N_u^{(3)}}{\partial z} & 0 & \dots & \frac{\partial N_u^{(20)}}{\partial x} \end{bmatrix} \quad (2.29)$$

and Eq. (2.28) becomes

$$\begin{aligned}
B_\phi &= \begin{bmatrix} \frac{\partial N_\phi^{(1)}}{\partial x} & \frac{\partial N_\phi^{(2)}}{\partial x} & \frac{\partial N_\phi^{(3)}}{\partial x} & \cdots & \frac{\partial N_\phi^{(20)}}{\partial x} \\ \frac{\partial N_\phi^{(1)}}{\partial y} & \frac{\partial N_\phi^{(2)}}{\partial y} & \frac{\partial N_\phi^{(3)}}{\partial y} & \cdots & \frac{\partial N_\phi^{(20)}}{\partial y} \\ \frac{\partial N_\phi^{(1)}}{\partial z} & \frac{\partial N_\phi^{(2)}}{\partial z} & \frac{\partial N_\phi^{(3)}}{\partial z} & \cdots & \frac{\partial N_\phi^{(20)}}{\partial z} \end{bmatrix} \\
B_\theta &= \begin{bmatrix} \frac{\partial N_\theta^{(1)}}{\partial x} & \frac{\partial N_\theta^{(2)}}{\partial x} & \frac{\partial N_\theta^{(3)}}{\partial x} & \cdots & \frac{\partial N_\theta^{(20)}}{\partial x} \\ \frac{\partial N_\theta^{(1)}}{\partial y} & \frac{\partial N_\theta^{(2)}}{\partial y} & \frac{\partial N_\theta^{(3)}}{\partial y} & \cdots & \frac{\partial N_\theta^{(20)}}{\partial y} \\ \frac{\partial N_\theta^{(1)}}{\partial z} & \frac{\partial N_\theta^{(2)}}{\partial z} & \frac{\partial N_\theta^{(3)}}{\partial z} & \cdots & \frac{\partial N_\theta^{(20)}}{\partial z} \end{bmatrix}
\end{aligned} \tag{2.30}$$

The shape functions  $N_u$ ,  $N_\phi$ ,  $N_\theta$  are given in the natural coordinates  $\xi_1$ ,  $\xi_2$ ,  $\xi_3$ , however, their partial derivatives are in relation to Cartesian coordinates  $x$ ,  $y$ ,  $z$ . The computation of these derivatives requires the inverse of the Jacobian matrix and the application of the chain rule. For the sake of simplicity, Eq. (2.28) is used to demonstrate the transformation of coordinates to evaluate the derivatives, and can be formulated as

$$\begin{bmatrix} \frac{\partial N_\phi^{(i)}}{\partial \xi_1} \\ \frac{\partial N_\phi^{(i)}}{\partial \xi_2} \\ \frac{\partial N_\phi^{(i)}}{\partial \xi_3} \end{bmatrix} = \underbrace{\begin{bmatrix} \frac{\partial x}{\partial \xi_1} & \frac{\partial y}{\partial \xi_1} & \frac{\partial z}{\partial \xi_1} \\ \frac{\partial x}{\partial \xi_2} & \frac{\partial y}{\partial \xi_2} & \frac{\partial z}{\partial \xi_2} \\ \frac{\partial x}{\partial \xi_3} & \frac{\partial y}{\partial \xi_3} & \frac{\partial z}{\partial \xi_3} \end{bmatrix}}_J \begin{bmatrix} \frac{\partial N_\phi^{(i)}}{\partial x} \\ \frac{\partial N_\phi^{(i)}}{\partial y} \\ \frac{\partial N_\phi^{(i)}}{\partial z} \end{bmatrix} \Rightarrow \begin{bmatrix} \frac{\partial N_\phi^{(i)}}{\partial x} \\ \frac{\partial N_\phi^{(i)}}{\partial y} \\ \frac{\partial N_\phi^{(i)}}{\partial z} \end{bmatrix} = J^{-1} \begin{bmatrix} \frac{\partial N_\phi^{(i)}}{\partial \xi_1} \\ \frac{\partial N_\phi^{(i)}}{\partial \xi_2} \\ \frac{\partial N_\phi^{(i)}}{\partial \xi_3} \end{bmatrix} \tag{2.31}$$

where  $J^{-1}$  is the inverse of the Jacobian matrix.

From the constitutive thermopiezoelectric equations (Eqs. (2.15)-(2.17)), and since there are three coupled fields (mechanical, electrical and thermal), the finite

element formulation can be derived following the method presented in [4] as

$$M_{uu}^e \ddot{u}^e + k_{uu}^e u^e + k_{u\phi}^e \phi^e - k_{u\theta}^e \theta^e = f_{uu}^e \quad (2.32)$$

$$k_{\phi u}^e u^e - k_{\phi\phi}^e \phi^e + k_{\phi\theta}^e \theta^e = f_{\phi\phi}^e \quad (2.33)$$

$$k_{\theta u}^e \dot{u}^e - k_{\theta\phi}^e \dot{\phi}^e + H_{\theta\theta}^e \dot{\theta}^e + k_{\theta\theta}^e \theta^e = f_{\theta\theta}^e \quad (2.34)$$

where the element mass matrix is

$$M_{uu}^e = \int_{V^e} \rho N_u^T N_u dV^e \quad (2.35)$$

where  $\rho$  is the density, and  $V^e$  means that the integral is evaluated over the volume of the element. The mechanical element stiffness matrix is given as

$$k_{uu}^e = \int_{V^e} B_u^T C B_u dV^e \quad (2.36)$$

where  $C$  is the stiffness matrix [N/m<sup>2</sup>] with dimensions 6×6, which for the case of PZT takes the form of a transversely isotropic material and can be written as

$$C = \begin{bmatrix} C_{11}^E & C_{12}^E & C_{13}^E & 0 & 0 & 0 \\ C_{21}^E & C_{22}^E & C_{23}^E & 0 & 0 & 0 \\ C_{31}^E & C_{32}^E & C_{33}^E & 0 & 0 & 0 \\ 0 & 0 & 0 & C_{44}^E & 0 & 0 \\ 0 & 0 & 0 & 0 & C_{55}^E & 0 \\ 0 & 0 & 0 & 0 & 0 & C_{66}^E \end{bmatrix} = \begin{bmatrix} C_{11}^E & C_{12}^E & C_{13}^E & 0 & 0 & 0 \\ C_{12}^E & C_{11}^E & C_{13}^E & 0 & 0 & 0 \\ C_{13}^E & C_{13}^E & C_{33}^E & 0 & 0 & 0 \\ 0 & 0 & 0 & C_{44}^E & 0 & 0 \\ 0 & 0 & 0 & 0 & C_{55}^E & 0 \\ 0 & 0 & 0 & 0 & 0 & C_{55}^E \end{bmatrix} \quad (2.37)$$

where  $C^E$  are the elastic constants at constant electric field. The direct piezoelectric coupling element stiffness matrix is described as

$$k_{u\phi}^e = \int_{V^e} B_u^T e^T B_\phi dV^e \quad (2.38)$$

where  $e$  is the matrix of piezoelectric stress coefficients [N/(Vm)] with dimension  $3 \times 6$ , which for the case of PZT can be written as

$$e = \begin{bmatrix} 0 & 0 & 0 & 0 & e_{15} & 0 \\ 0 & 0 & 0 & e_{15} & 0 & 0 \\ e_{31} & e_{32} & e_{33} & 0 & 0 & 0 \end{bmatrix} \quad (2.39)$$

The elasto-thermal element stiffness matrix is given as

$$k_{u\theta}^e = \int_{V^e} B_u^T \zeta N_\theta dV^e \quad (2.40)$$

where  $\zeta$  is the thermal stress coefficient vector [N/(m<sup>2</sup>K)] which is obtained by multiplying the compliance matrix  $C$  by the vector of thermal expansion coefficients  $\alpha$ , where  $\alpha$  is given as

$$\alpha = \begin{bmatrix} \alpha_{11} \\ \alpha_{22} \\ \alpha_{33} \\ 0 \\ 0 \\ 0 \end{bmatrix} \quad (2.41)$$

Therefore the thermal stress coefficients vector  $\zeta$ , for PZT, can be written as

$$\zeta = \begin{bmatrix} C_{11}^E \alpha_{11} + C_{12}^E \alpha_{22} + C_{13}^E \alpha_{33} \\ C_{21}^E \alpha_{11} + C_{22}^E \alpha_{22} + C_{23}^E \alpha_{33} \\ C_{31}^E \alpha_{11} + C_{32}^E \alpha_{22} + C_{33}^E \alpha_{33} \\ 0 \\ 0 \\ 0 \end{bmatrix} \quad (2.42)$$

The dielectric element stiffness matrix is described as

$$k_{\phi\phi}^e = \int_{V^e} B_{\phi}^T \varepsilon B_{\phi} dV^e \quad (2.43)$$

where  $\varepsilon$  is the matrix of dielectric coefficients [F/m] with dimensions  $3 \times 3$ , which is given as

$$\varepsilon = \begin{bmatrix} \varepsilon_{11}^{Tr} & 0 & 0 \\ 0 & \varepsilon_{22}^{Tr} & 0 \\ 0 & 0 & \varepsilon_{33}^{Tr} \end{bmatrix} \quad (2.44)$$

where  $\varepsilon^{Tr}$  are the free dielectric constants (piezoelectric measured when completely unconstrained), which are described as relative dielectric constants  $\varepsilon$  multiplied by the permittivity of free space ( $\varepsilon_0 = 8.85418782 \times 10^{-12}$  [F/m]). The pyroelectric element stiffness matrix is given as

$$k_{\phi\theta}^e = \int_{V^e} B_{\phi}^T p N_{\theta} dV^e \quad (2.45)$$

where  $p$  is the vector of pyroelectric coefficients, and can be written as

$$p = \begin{bmatrix} p_1 \\ p_2 \\ p_3 \end{bmatrix} \quad (2.46)$$

The thermal element stiffness matrix can be described as

$$k_{\theta\theta}^e = \int_{V^e} B_{\theta}^T \lambda B_{\theta} dV^e + \int_{O_n^e} N_{\theta}^T h_v N_{\theta} dO^e \quad (2.47)$$

where  $\lambda$  is the matrix of heat conduction coefficients [W/(mK)] and it is formulated

as

$$\lambda = \begin{bmatrix} \lambda_{11} & 0 & 0 \\ 0 & \lambda_{22} & 0 \\ 0 & 0 & \lambda_{33} \end{bmatrix} \quad (2.48)$$

The second term in Eq.(2.47),  $h_v$ , is referred to as the convective heat transfer coefficient, and  $O_h^e$  means that the integral is evaluated over the surface. The thermoelastic element stiffness matrix is formulated as

$$k_{\theta u}^e = \int_{V^e} N_{\theta}^T N_{\theta} \Theta \zeta^T B_u dV^e \quad (2.49)$$

where  $\Theta$  is the reference temperature, which is typically referred to as the nodal temperature. The electrocaloric element stiffness matrix is written as

$$k_{\theta \phi}^e = \int_{V^e} N_{\theta}^T N_{\theta} \Theta p^T dV^e \quad (2.50)$$

The heat capacity element stiffness matrix is described as

$$H_{\theta \theta}^e = \int_{V^e} N_{\theta}^T \rho c_v N_{\theta} dV^e \quad (2.51)$$

where  $c_v$  is the heat capacity coefficient of the material. The external mechanical element force vector is defined as

$$f_{uu}^e = \int_{V^e} N_u^T \rho b dV^e + \int_{O^e} N_u^T \bar{t} dO^e \quad (2.52)$$

where  $b$  is the vector of body forces,  $O^e$  denotes the prescribed values of traction  $\bar{t}$  on the surface. The electric element charge vector is given as

$$f_{\phi \phi}^e = - \int_{O^e} N_{\phi}^T \bar{Q} dO^e \quad (2.53)$$

where  $\bar{Q}$  is the prescribed surface charge on the surface  $O^e$ . The external thermal element force vector is written as

$$f_{\theta\theta} = \int_{O_h^e} N_\theta^T h_v (\Theta_\infty - \Theta_0) dO^e + \int_{O^e} N_\theta^T \bar{q}_s dO^e + \int_{V^e} \rho r dV^e \quad (2.54)$$

where  $\Theta_\infty$  is the ambient temperature,  $\Theta_0$  is the stress free temperature or body temperature,  $\bar{q}_s$  is the prescribed heat flux across the surface  $O^e$ , and  $r$  is the quantity of heat generated by internal heat sources per unit of time. All equations are presented in Tables A.1–A.3 for further reference. To form the matrices, Gaussian quadrature is applied to evaluate the integrals (see Eq. (2.14)). For the sake of simplicity, Eq. (2.35) is used to demonstrate the Gaussian quadrature technique, and it is given as

$$\begin{aligned} M_{uu}^e &= \int_{-1}^1 \int_{-1}^1 \int_{-1}^1 \rho N_u^T N_u |J| d\xi_1 d\xi_2 d\xi_3 = \\ &= \sum_{i=1}^n \sum_{j=1}^n \sum_{k=1}^n \rho N_u^T(\xi_i, \xi_j, \xi_k) N_u(\xi_i, \xi_j, \xi_k) |J| W_{\xi_i} W_{\xi_j} W_{\xi_k} \end{aligned} \quad (2.55)$$

where  $|J|$  is the determinant of the Jacobian matrix.

If the elemental system of differential equations in Eqs. (2.32–2.34) are assembled into a global matrix, the system of equations can be written as

$$\begin{aligned} \begin{bmatrix} M_{uu} & 0 & 0 \\ 0 & 0 & 0 \\ 0 & 0 & 0 \end{bmatrix} \begin{bmatrix} \ddot{U} \\ \ddot{\Phi} \\ \ddot{\Theta} \end{bmatrix} + \begin{bmatrix} 0 & 0 & 0 \\ 0 & 0 & 0 \\ K_{\theta u} & -K_{\theta\phi} & H_{\theta\theta} \end{bmatrix} \begin{bmatrix} \dot{U} \\ \dot{\Phi} \\ \dot{\Theta} \end{bmatrix} \\ + \begin{bmatrix} K_{uu} & K_{u\phi} & -K_{u\theta} \\ K_{\phi u} & -K_{\phi\phi} & K_{\phi\theta} \\ 0 & 0 & K_{\theta\theta} \end{bmatrix} \begin{bmatrix} U \\ \Phi \\ \Theta \end{bmatrix} = \begin{bmatrix} F_u \\ F_\phi \\ F_\theta \end{bmatrix} \end{aligned} \quad (2.56)$$

where the mass  $M_{uu}$  of the body multiplies the acceleration of the body in the first term of Eq. (2.56). The second term refers to the damping matrix, which multiplies the first derivatives of displacement, electric potential, and temperature. The first two terms of Eq. (2.56) are typically applied in dynamic analyses. The third term is referred to as the global stiffness matrix, which multiplies the displacement, electric potential, and temperature, and is used in static analyses. The sum of the first three terms equals the global vector of forces, which includes the mechanical, electrical, and thermal forces.

## 2.6 Boundary Conditions

Boundary conditions are fundamental constraints or specifications applied to the boundaries or nodes of the domain, where it is specified how the solution behaves at the boundaries, ensuring that the analysis accurately depicts physical conditions. If boundary conditions are not specified in the finite element method, the determinant of the global stiffness matrix  $K$  will be zero, and its inverse will not exist. This singularity is typically addressed by imposing boundary conditions [21, 88, 91].

Boundary conditions are generally classified into two types. The first type is referred to as essential or Dirichlet boundary conditions, in which the values that the primary variables (displacements, electric potential, temperature) must take on the domain are specified. The second type, the natural or Neumann boundary con-

dition, specifies the values that the derivatives must assume within the domain, as shown in the example in Fig. 2.6. The example shows a domain  $\Omega$  with a boundary  $\partial\Omega$ , where the solution is satisfied if

$$u|_{\Gamma_1} = u_0 \quad \text{and} \quad \frac{\partial u}{\partial n}\Big|_{\Gamma_2} = g \quad (2.57)$$

where  $u_0$  and  $g$  are functions defined on the boundaries  $\Gamma_1$  and  $\Gamma_2$ , respectively.

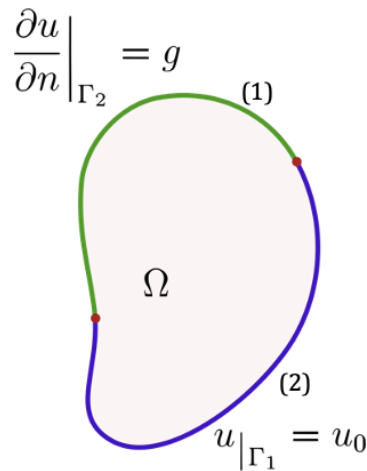


Fig. 2.8 Example of boundary conditions: Neumann (1), Dirichlet (2). (Image adapted from:[15])

Typically, structures have mechanical constraints such that the body under study is not free to move when external loads are applied. For instance, a beam under a mechanical concentrated force often has a support that prevents the beam from moving, which requires the displacements at the support to be zero. This condition is referred to as a homogeneous boundary condition when the values of

the variables are set to zero at the boundary of the domain. Electric potential and temperature can also be specified as zero along the domain when dealing with thermopiezoelectric problems. Furthermore, electric potential and temperature are also frequently prescribed to be at a level other than zero, therefore non-homogeneous boundary conditions have to be taken into account, where the values that the solution needs to take on the domain must be specified.

### 2.6.1 Homogeneous Boundary Conditions

The finite element implementation of homogeneous boundary conditions is straightforward. For the sake of simplicity, the implementation is demonstrated for displacements, but can be extended to electric potential and temperature with the same technique. Therefore, for the nodes that are mechanically constrained, their displacement will be zero. Generally, in one-dimensional cases, it is easier to remove the rows and columns associated with the constrained nodes in the stiffness matrix  $K$ , in the force vector  $F$ , and in the displacement vector  $U$ , reducing the system of matrices to be solved. However, when working with three-dimensional problems and higher degrees of freedom, a more elegant technique can be employed. The rows of the global force vector  $F$  corresponding to the constrained nodes are set to zero, the rows and columns of the global stiffness matrix  $K$  associated with the constrained nodes are set to zero, and the diagonal entry of the constrained nodes

in the global stiffness matrix  $K$  is set equal to one. This technique allows the rows and columns to be retained which can avoid mistakes because there is no need to rearrange the system of equations after the solution is calculated. Furthermore, it allows the calculation of reaction forces. For the sake of simplicity, both techniques are demonstrated with a simple example of a one-dimensional case, which can be extended to two-dimensional and three-dimensional cases. Consider a  $3 \times 3$  system of equations, where  $U_1$  is constrained in  $x$

$$\begin{bmatrix} K_{11} & K_{12} & K_{13} \\ K_{21} & K_{22} & K_{23} \\ K_{31} & K_{32} & K_{33} \end{bmatrix} \begin{bmatrix} U_1 \\ U_2 \\ U_3 \end{bmatrix} = \begin{bmatrix} F_1 \\ F_2 \\ F_3 \end{bmatrix} \quad (2.58)$$

By using the elimination technique, Eq. (2.58) can be rewritten as a  $2 \times 2$  system of matrices

$$\begin{bmatrix} K_{22} & K_{23} \\ K_{32} & K_{33} \end{bmatrix} \begin{bmatrix} U_2 \\ U_3 \end{bmatrix} = \begin{bmatrix} F_2 \\ F_3 \end{bmatrix} \quad (2.59)$$

where the system of equations can be described as

$$K_{22}U_2 + K_{23}U_3 = F_2 \quad (2.60)$$

$$K_{32}U_2 + K_{33}U_3 = F_3$$

By implementing the technique where the rows and columns are retained, Eq. (2.58)

is written as

$$\begin{bmatrix} 1 & 0 & 0 \\ 0 & K_{22} & K_{23} \\ 0 & K_{32} & K_{33} \end{bmatrix} \begin{bmatrix} U_1 \\ U_2 \\ U_3 \end{bmatrix} = \begin{bmatrix} R_1 \\ F_2 \\ F_3 \end{bmatrix} \quad (2.61)$$

where  $R_1$  is the reaction force in the constrained node. Now the system of equations is described as

$$\begin{aligned}
 U_1 + 0K_{12} + 0K_{13} &= R_1 \\
 0K_{21} + K_{22}U_2 + K_{23}U_3 &= F_2 \\
 0K_{31} + K_{32}U_2 + K_{33}U_3 &= F_3
 \end{aligned} \tag{2.62}$$

### 2.6.2 Non-homogeneous Boundary Conditions

The implementation of non-homogeneous boundary conditions is more complex than for the case of homogeneous boundary conditions. In this type of boundary condition, the value that the solution must have on the boundary of domain is specified but is not equal to zero. To enact this type of boundary condition, the first step is to rearrange the equations considering the values that the solution must obtain. Consider the example in Eq. (2.58), where  $U_1$  is constrained in  $x$ , where now, in addition,  $U_3$  has a prescribed nodal value  $d$  which can be written as

$$\begin{bmatrix} K_{11} & K_{12} & K_{13} \\ K_{21} & K_{22} & K_{23} \\ K_{31} & K_{32} & K_{33} \end{bmatrix} \begin{bmatrix} U_1 \\ U_2 \\ d \end{bmatrix} = \begin{bmatrix} F_1 \\ F_2 \\ F_3 \end{bmatrix} \tag{2.63}$$

The non-homogeneous boundary condition follows the same process as the homogeneous boundary conditions, with the difference that the force vector  $F$  has to be rearranged to account for the prescribed value of  $U_3$ . The rows and columns associated with the prescribed value are set to zero in the global stiffness matrix

$K$ , with the exception of the diagonal value  $K_{33}$ . Eq. (2.65) can be rewritten as

$$\begin{bmatrix} 1 & 0 & 0 \\ 0 & K_{22} & 0 \\ 0 & 0 & K_{33} \end{bmatrix} \begin{bmatrix} U_1 \\ U_2 \\ d \end{bmatrix} = \begin{bmatrix} R_1 \\ F_2 \\ F_3 \end{bmatrix} \quad (2.64)$$

Now, to get rid of  $d$  in the system of equations, the force vector  $F$  is rearranged as

$$\begin{bmatrix} 1 & 0 & 0 \\ 0 & K_{22} & 0 \\ 0 & 0 & K_{33} \end{bmatrix} \begin{bmatrix} U_1 \\ U_2 \\ U_3 \end{bmatrix} = \begin{bmatrix} R_1 \\ K_{23}d \\ K_{33}d \end{bmatrix} \quad (2.65)$$

where the solution of the system of equations results

$$\begin{aligned} U_1 &= R_1 \\ U_2 &= \frac{K_{23}d}{K_{22}} \\ U_3 &= \frac{K_{33}d}{K_{33}} = d \end{aligned} \quad (2.66)$$

Without loss of generality, this process can be employed to set the boundary conditions corresponding to the electric potential and temperature.

## 2.7 Static Analysis

The numerical static solution of Eq. (2.56) for static analysis is straightforward and can be solved for mechanical, piezoelectric, thermoelastic, and thermopiezoelectric problems. For mechanical problems, the equation is solved for the nodal displacements  $U$  and can be written as

$$U = K_{uu}^{-1}F \quad (2.67)$$

For piezoelectric problems, the equation is solved for both the displacement and the electric potential, where the equation considers only the elastic, piezoelectric, and dielectric matrices, and it is simplified to

$$\begin{bmatrix} U \\ \Phi \end{bmatrix} = \begin{bmatrix} K_{uu} & K_{u\phi} \\ K_{\phi u} & -K_{\phi\phi} \end{bmatrix}^{-1} \begin{bmatrix} F_u \\ F_\phi \end{bmatrix} \quad (2.68)$$

The solution of this equation will yield the vector  $\begin{bmatrix} U \\ \Phi \end{bmatrix}$ , in which the nodal displacements and electric potential can be easily split by means of number of degrees of freedom. For instance, for one single element, the mechanical degrees of freedom are three  $(x, y, z)$ , and for a 20-noded hexahedral element, the total number of mechanical degrees of freedom is 60. Therefore, the displacement will be the first 60 values of the vector  $\begin{bmatrix} U \\ \Phi \end{bmatrix}$ , and the electric potential  $\Phi$  will be the remaining 20, since  $\Phi$  has only one degree of freedom per node.

For thermoelastic problems, the equation is solved for both the displacement and temperature, and the equation is reduced to

$$\begin{bmatrix} U \\ \Theta \end{bmatrix} = \begin{bmatrix} K_{uu} & -K_{u\theta} \\ 0 & K_{\theta\theta} \end{bmatrix}^{-1} \begin{bmatrix} F_u \\ F_\theta \end{bmatrix} \quad (2.69)$$

For thermopiezoelectric problems, the full Eq. (2.56) is considered and is solved for the displacement, electric potential, and temperature. It is given as

$$\begin{bmatrix} U \\ \Phi \\ \Theta \end{bmatrix} = \begin{bmatrix} K_{uu} & K_{u\phi} & -K_{u\theta} \\ K_{\phi u} & -K_{\phi\phi} & K_{\phi\theta} \\ 0 & 0 & K_{\theta\theta} \end{bmatrix}^{-1} \begin{bmatrix} F_u \\ F_\phi \\ F_\theta \end{bmatrix} \quad (2.70)$$

Without loss of generality, the variables  $U$ ,  $\Phi$ , and  $\Theta$  are separated by type of degree of freedom, in which the displacement  $U$  has three degrees of freedom per node, while the electric potential,  $\Phi$ , and temperature,  $\Theta$ , have only one degree of freedom per node.

## 2.8 Modal Analysis

Modal analysis is the study of the dynamic characteristics of a system, in particular the natural frequencies, which are the frequencies at which the structure naturally oscillates [92]. The modal analysis follows a relation which is described as

$$(K - \omega^2 M)\Lambda = 0 \quad (2.71)$$

where  $K$  is the global stiffness matrix,  $M$  is the global mass matrix,  $\omega$  is the angular natural frequency (where  $\omega^2$  are the eigenvalues), and  $\Lambda$  is the matrix of mode shape vectors (or eigenvectors) associated with the natural frequencies. The solution of Eq. 2.71 is straightforward and results in the eigenvalues of the system. The eigenfrequencies [rad/s] of the system can now be obtained from the eigenvalues through the relation given as

$$\omega = \lambda^{\frac{1}{2}} \quad (2.72)$$

where  $\lambda$  represents the eigenvalues. The modal analysis provides important information regarding how a structure responds to induced vibrations or dynamic loads. Knowledge of the natural frequencies of a structure allows the calculation of the damping ratio, which is a dimensionless measure used to describe how oscillations decay in a vibrating system. This information is crucial for accurately analyzing structures subjected to external dynamic loads.

In the verification section, the bimorph actuator PL127.10 from *PI Ceramics* is used in simulations. Therefore, a modal analysis is performed in both FE code and ABAQUS to obtain the frequencies and, consequently, the damping coefficients. A comparison of the natural frequencies of the first 5 modes between the FE code and ABAQUS is presented in Table 2.3, demonstrating excellent agreement between the results. Furthermore, the corresponding mode shapes plots are shown in Fig. 2.9.

Modal Analysis - Bimorph PL127.10 (31×9.6×0.67) [mm]		
	FE Code	ABAQUS
Frequency [Hz]	443.74	443.74
	2454.45	2454.46
	2760.52	2760.52
	5668.79	5668.79
	7723.75	7723.75

Table 2.3 A comparison of the first five natural frequencies between the FE Code and ABAQUS

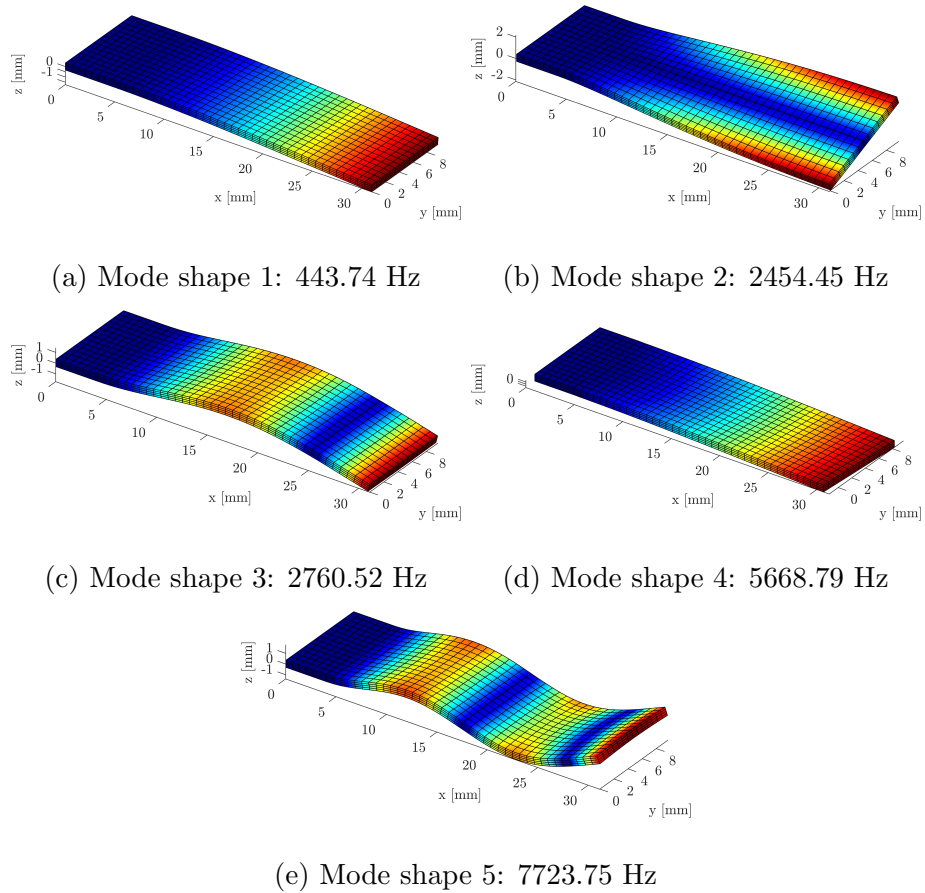


Fig. 2.9 Five mode shapes of the PL127.10 modal analysis in the FE code

## 2.9 Dynamic Analysis

For piezoelectric actuators, their advantage lies in their fast response. Therefore, the dynamic solution of interest involves determining nodal displacements, electric potential, and temperature at different time steps for any dynamic system, a process referred to as numerical integration in time [91, 21]. The most common method is direct integration, which can be divided into implicit and explicit methods. The

implicit method requires the calculation of the effective stiffness matrix at each time step  $t + \Delta t$ , while the explicit method does not. However, the implicit method, more specifically, the Newmark-Beta method, will be used as the integration in time, since it is more versatile and unconditionally stable [91, 21].

### 2.9.1 Newmark Integration Method

The Newmark method is a classic example of an implicit time-integration algorithm, in which two parameters are introduced:  $\beta$ , and  $\gamma$ . These parameters are used to control the stability and accuracy of the numerical integration, where  $\beta$  is usually chosen between 0 and  $\frac{1}{4}$ , and  $\gamma$  is frequently used as  $\frac{1}{2}$ . It has been shown that the numerical analysis is stable when  $\beta$  and  $\gamma$  are taken to be  $\frac{1}{4}$  and  $\frac{1}{2}$  respectively, resulting in the average acceleration method [91, 87]. This method is considered to be unconditionally stable, meaning that the solution will converge for all time increments [21, 91, 89].

The displacement  $U_{t+\Delta t}$  and velocity  $\dot{U}_{t+\Delta t}$  at time  $t + \Delta t$  in the Newmark method are described as

$$U_{t+\Delta t} = U_t + (\Delta t)\dot{U}_t + \left[ \left( \frac{1}{2} - \beta \right) \Delta t^2 \right] \ddot{U}_t + (\beta \Delta t^2) \ddot{U}_{t+\Delta t} \quad (2.73)$$

$$\dot{U}_{t+\Delta t} = \dot{U}_t + [(1 - \gamma)\Delta t] \ddot{U}_t + (\gamma \Delta t) \ddot{U}_{t+\Delta t} \quad (2.74)$$

Applying the time-stepping method, as

$$\Delta U_t = U_{t+\Delta t} - U_t \quad (2.75)$$

$$\Delta \dot{U}_t = \dot{U}_{t+\Delta t} - \dot{U}_t \quad (2.76)$$

$$\Delta \ddot{U}_t = \ddot{U}_{t+\Delta t} - \ddot{U}_t \quad (2.77)$$

Eqs. (2.73-2.74) can be rewritten as

$$\Delta U_t = (\Delta t)\dot{U}_t + \frac{\Delta t^2}{2}\ddot{U}_t + (\beta\Delta t^2)\Delta\ddot{U}_t \quad (2.78)$$

$$\Delta\dot{U}_t = (\Delta t)\ddot{U}_t + (\gamma\Delta t)\Delta\ddot{U}_t \quad (2.79)$$

Solving for the acceleration  $\Delta\ddot{U}_t$  yields

$$\Delta\ddot{U}_t = \frac{1}{\beta(\Delta t)^2}\Delta U_t - \frac{1}{\beta(\Delta t)}\dot{U}_t - \frac{1}{2\beta}\ddot{U}_t \quad (2.80)$$

Substituting the term  $\Delta\ddot{U}_t$  in Eq. (2.79), the velocity can be described as

$$\Delta\dot{U}_t = \frac{\gamma}{\beta(\Delta t)}\Delta U_t - \frac{\gamma}{\beta}\dot{U}_t - \left[ \left( \frac{\gamma}{2\beta} - 1 \right) \Delta t \right] \ddot{U}_t \quad (2.81)$$

The displacement is calculated by taking the inverse of the effective dynamic stiffness  $\hat{K}$  and multiplying by the effective dynamic load  $\hat{F}$ , at each time step.

This is given as

$$\Delta U_t = \hat{K}^{-1}\hat{F} \quad (2.82)$$

where  $\hat{K}$  is calculated as

$$\hat{K} = K + \frac{\gamma}{\beta(\Delta t)}D + \frac{1}{\beta(\Delta t)^2}M \quad (2.83)$$

and  $\hat{F}$  is calculated as

$$\hat{F} = F + F_{\Delta t} + \left[ \frac{1}{\beta(\Delta t)} M + \frac{\gamma}{\beta} D \right] \dot{U}_t + \left[ \frac{1}{2\beta} M + \left( \frac{\gamma}{2\beta} - 1 \right) (\Delta t) D \right] \ddot{U}_t \quad (2.84)$$

where  $D$  and  $M$  are the damping and mass matrices. Referring to Eq. (2.56), the damping matrix is rewritten as

$$D = \begin{bmatrix} R & 0 & 0 \\ 0 & 0 & 0 \\ K_{\theta u} & -K_{\theta \phi} & H_{\theta \theta} \end{bmatrix} \quad (2.85)$$

where  $R$  stands for the classical Rayleigh damping, which is a proportional linear combination of the mass matrix (see Eq. (2.35)) and elastic stiffness matrix (see Eq. (2.36)), and is given as

$$R = \alpha_R M_{uu} + \beta_R K_{uu} \quad (2.86)$$

where  $\alpha_R$  and  $\beta_R$  are the Rayleigh damping coefficients. These coefficients can be described as

$$\zeta_i = \frac{\alpha_R}{2\omega_i} + \frac{\beta_R \omega_i}{2} \quad (2.87)$$

where  $\zeta_i$  is the damping ratio, and  $\omega_i$  is the angular frequency [rad/s] which can be calculated from a modal analysis. Table 2.4 summarizes the steps for the implementation of the Newmark integration method.

## Newmark method

---

1. Initialize  $U$ ,  $\dot{U}$ , and  $\ddot{U}$  at time step zero
  2. Select time step  $\Delta t$ , and parameters  $\gamma$  and  $\beta$
  3. Form the effective stiffness matrix  $\hat{K}$  (Eq. (2.83)), and triangularize it
  4. For each time step:
    - 4.1 Calculate the effective load matrix  $\hat{F}$  (Eq. (2.84))
    - 4.2 Calculate the displacement  $\Delta U_t$  (Eq. (2.82))
    - 4.3 Calculate the velocity  $\Delta \dot{U}_t$  (Eq. (2.81))
    - 4.4 Calculate the acceleration  $\Delta \ddot{U}_t$  (Eq. (2.80))
    - 4.5 Repeat step number 4 until the last time step
  5. Output of final displacements, velocities, and accelerations
- 

Table 2.4 Steps of the Newmark integration method

### 2.10 Verification of Static Analysis

The implementation of the code is divided into steps. The first step is to implement the finite element code for 3D solid elements, followed by piezoelectric elements, thermoelastic elements, and finally thermopiezoelectric elements. Confidence in the implementation is established by using the commercial code ABAQUS to bound and verify the results for each step. This section covers the verification of the code for both static and dynamic cases. The coefficients needed for verification

are acquired from several sources of information, such as from *Physik Instrumente Ceramic*.

For mechanical element simulations, aluminum is used. For the simulations involving piezoelectric and thermoelastic elements, the bimorph PL127.10 from *Physik Instrumente Ceramic* [2] is used. For all cases the same structure is used, a rectangular structure with dimensions  $31 \times 9.6 \times 0.67$  mm, with a free length of 27 mm (see Fig. 2.10).

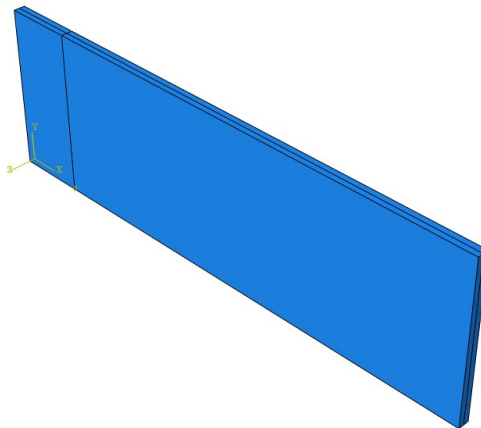


Fig. 2.10 Rectangular structure with 2 attached layers with dimensions of  $31 \times 9.6 \times 0.67$  mm

### 2.10.1 Three-Dimensional Solid Element with Reduced Integration

For a mechanical problem (3D solid elements), the code is verified by comparing the results with the commercial software ABAQUS. Element matrices are

calculated, and then Eq. (2.67) is solved. In the case of three-dimensional elements, the density  $\rho$  and the compliance matrix  $C$  are required.

### 2.10.1.1 Three-Dimensional Solid Static Case

For the solid element verification, concentrated forces of 1 N are applied in the  $z$  direction, on the edge nodes. Fig. 2.11 shows the region and nodes where the concentrated mechanical forces are applied. The beam has 160 total elements and 1053 nodes. The material used is aluminum with a Young's modulus of  $E = 70$  GPa, and Poisson's ratio of  $\nu = 0.33$ .

Fig. 2.12 provides the comparison between the implemented code and ABAQUS, showing that both agree qualitatively when comparing the mesh profile, and quantitatively with a maximum deflection in the  $z$  direction of approximately 748  $\mu\text{m}$ . There is no difference between the implemented code and the solution obtained via commercial software.

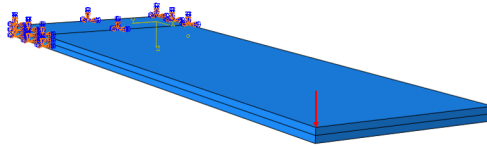


Fig. 2.11 Aluminum plate with forces (red arrows) applied on the edge nodes

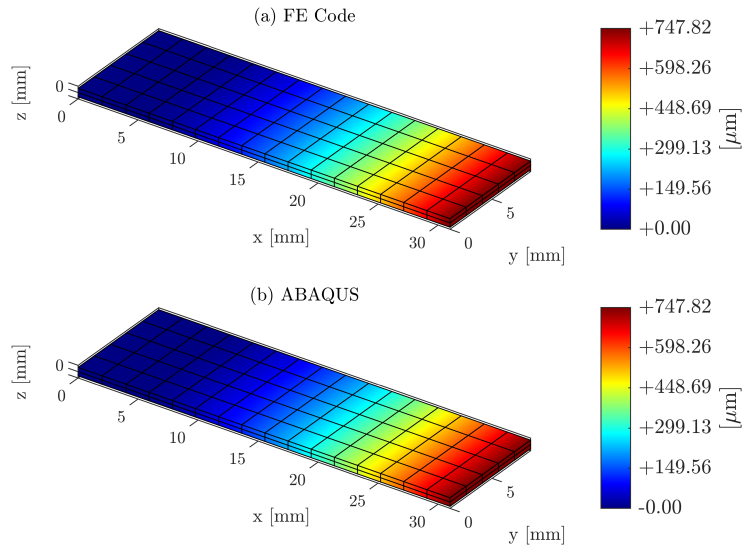


Fig. 2.12 Developed displacement in  $z$  for the three-dimensional solid static case

## 2.10.2 Piezoelectric Element

To verify, Eq. (2.68) is solved to obtain the solution for piezoelectric simulations. For this case, the compliance matrix  $C$ , the piezoelectric coefficients matrix  $e$ , and the dielectric matrix  $\varepsilon$  are required. In this case, two separate analyses are conducted to capture both mechanical and electrical behaviour.

### 2.10.2.1 Piezoelectric Static Case 1

As a first simulation, a typical example of the converse piezoelectric effect is examined. For this case, 531 V is applied to the bimorph in parallel connection and its left end is mechanically constrained, leaving a free length of 27 mm. In

the parallel connection, both top and bottom surfaces are set to a specific voltage, which is 531 V in this case, and the middle surface is set to ground (0 V), meaning the polarization of both layers is in the same direction. The bending direction is in the  $z$ -direction, and therefore, Fig. 2.13(a) refers to the  $z$ -displacement, showing an agreed maximum bending of around 458  $\mu\text{m}$  for both FE code and ABAQUS results, while Fig. 2.13(b) provides the expected voltage magnitude and profile.

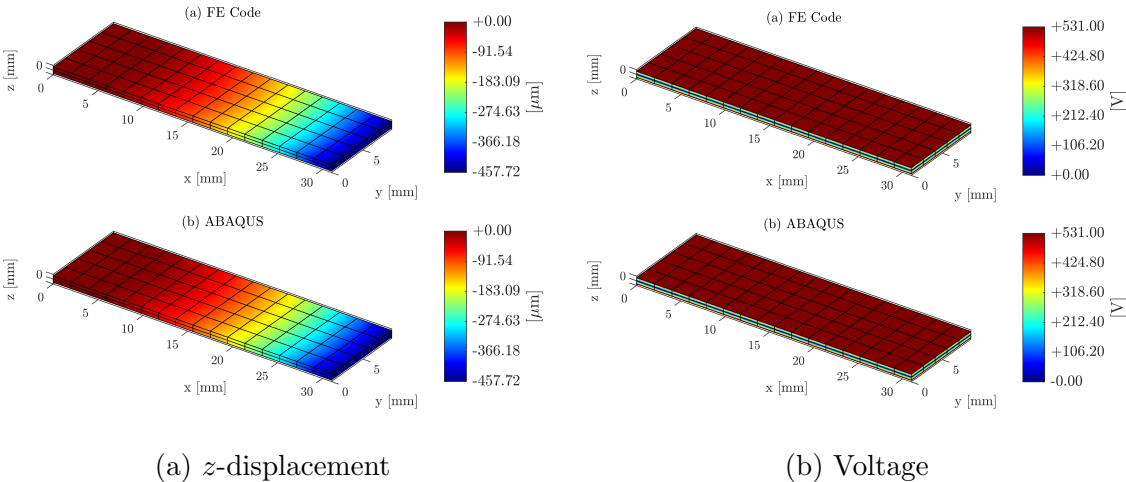


Fig. 2.13 Displacement in  $z$  and voltage results for the piezoelectric static case 1

### 2.10.2.2 Piezoelectric Static Case 2

An example of the direct piezoelectric effect is studied in this example, in which a concentrated force of 1 N is applied to the tip of the bimorph (right end), exactly in the middle of the actuator (see Fig. 2.14).

The direct piezoelectric effect generates an electric potential in the material

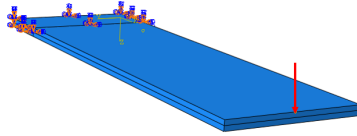


Fig. 2.14 Bimorph PL127.10 with a concentrated force applied in the right end, middle node.

when a mechanical force is applied. Fig. 2.15(b) provides the developed voltage after the concentrated force is applied to the middle node, right end of the bimorph. The static numerical analysis from the FE code produced a voltage of 15.30 V, and the commercial software showed a result of 15.16 V. The difference between the results is of about 0.2%, showing an excellent agreement. The deflection of the actuator is shown in Fig. 2.15(a), and a maximum displacement of 367.96  $\mu\text{m}$  is observed in the numerical analysis, while 367.86  $\mu\text{m}$  is the maximum deflection obtained from ABAQUS. Both the implemented code and ABAQUS plots agree qualitatively and quantitatively, with differences of less than 0.2%.

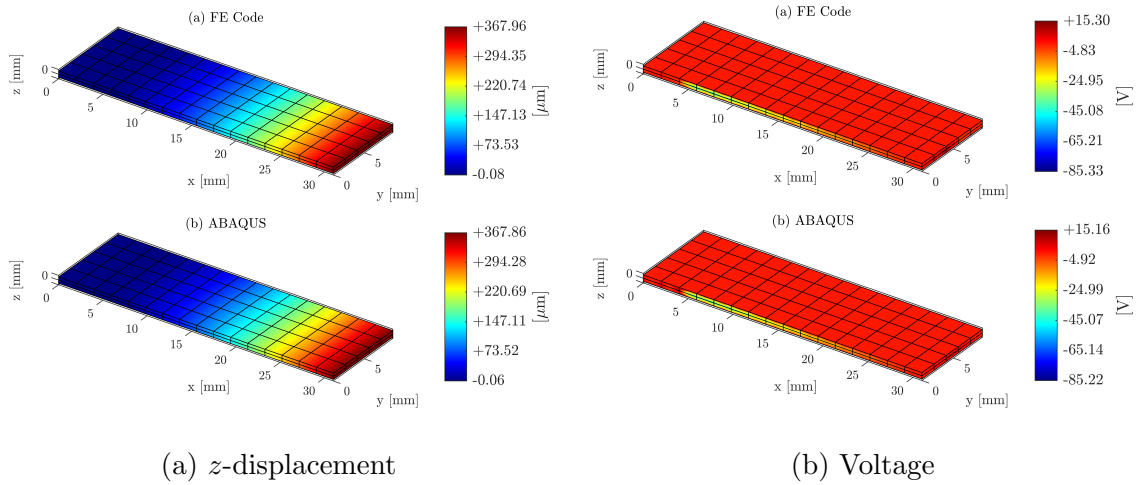


Fig. 2.15 Displacement in  $z$  and voltage results for the piezoelectric static case 2

### 2.10.3 Thermoelastic Element

For thermoelastic problems, the solution is obtained by solving Eq. (2.69). In this case, the compliance matrix  $C$ , the vector of thermal expansion  $\alpha$ , the specific heat capacity coefficient  $c_v$ , and the matrix of heat conduction coefficients  $\lambda$  are required. Since convection is neglected, the convective heat transfer coefficient  $h_v$  is not needed. In ABAQUS, the analysis type used is a coupled temperature-displacement analysis, in which the mechanical and thermal fields are coupled.

#### 2.10.3.1 Thermoelastic Static Case

The considered study is that of a 30 K temperature enforced along the surface at the tip of the bimorph, while the left end is constrained for both the temper-

ature and displacement. Since the material is expanding, Fig.2.16(a) shows the displacement mesh contour in the  $x$  axis, and a maximum expansion of  $2.78 \mu\text{m}$  is observed in this test for both FE Code and ABAQUS. Fig.2.16(b) provides the mesh contour of the developed temperature and its magnitude where it is clearly noticed that the temperature is increasing gradually from the constrained end of the bimorph (left end) to the free end of the actuator (right end), until it reaches the temperature of  $30 \text{ K}$ , matching the gradual increasing expansion in the  $x$  axis.

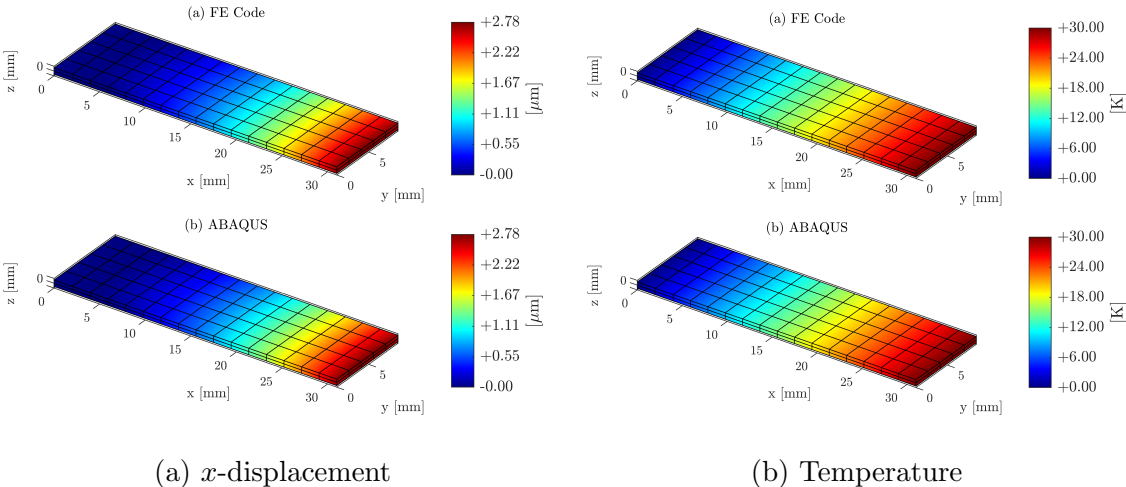


Fig. 2.16 Displacement in  $x$  and temperature results for a thermal load application

### 2.10.4 Verification of Numerical Analysis with Benchmark

The static analysis verification demonstrated that the implemented code exhibited excellent agreement with ABAQUS for various simulations. Nevertheless, it

remains important to verify the developed code against benchmarks proposed in the literature. Therefore, this section covers the verification of the numerical analysis from the implemented MATLAB finite element code with a benchmark in the literature. H.S. Tzou proposed in his book *Piezoelectric Shells* [85] a benchmark example of a bimorph beam, consisting of two layers of PVDF material with dimensions  $100 \times 5 \times 1$  mm (see Fig. 2.17) with opposite polarization directions. The material parameters for this example can be found in Table 2.5.

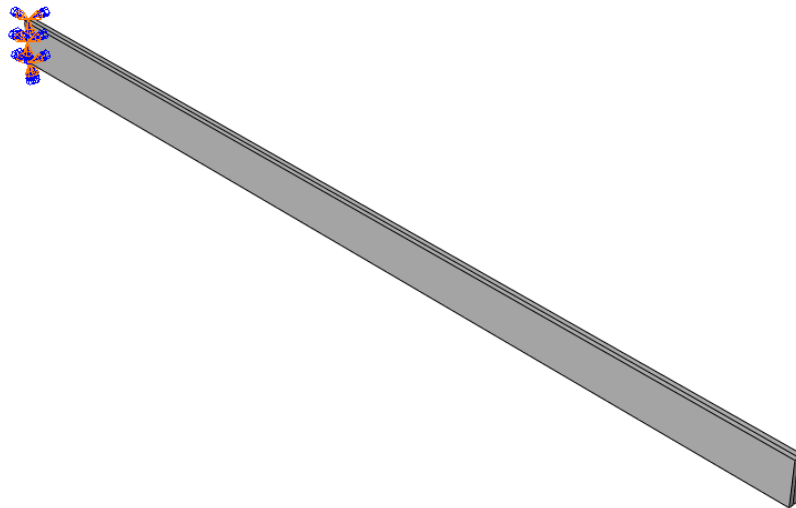


Fig. 2.17 Bimorph beam consisting of PVDF material with dimensions  $100 \times 5 \times 1$  mm

For the simulation, a voltage difference of 1 V through the thickness of the bimorph is applied (0.5 V at top surface, ground at the middle, and -0.5 V at the bottom surface). A 20 noded hexahedral element with reduced integration is

Material coefficients PVDF		
Coefficient	Unit	Value
Young's Modulus	$\frac{\text{N}}{\text{m}^2}$	$2 \times 10^9$
Poisson's Ratio $\nu$		0.29
Piezoelectric stress coefficient $e_{31}, e_{23}$	$\frac{\text{N}}{\text{Vm}}$	0.046
Dielectric matrix coefficient $\epsilon_{11}, \epsilon_{22}, \epsilon_{33}$	$\frac{\text{F}}{\text{m}}$	$1.069 \times 10^{-9}$
Mass density	$\frac{\text{kg}}{\text{m}^3}$	1800

Table 2.5 Material coefficients PVDF

used in the simulation and the results for the transverse deflection of the bimorph (displacement in the  $z$ -axis) is presented in Fig. 2.18. The numerical results are demonstrated to have an excellent agreement with the analytical results provided by Tzou [85].

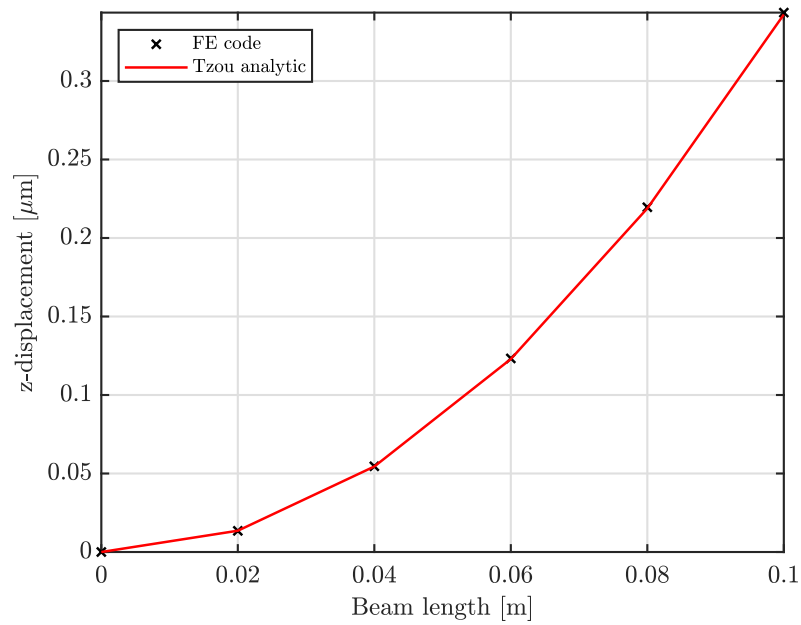


Fig. 2.18 Transverse deflection

## 2.11 Verification of Transient Analysis

In this section the transient analysis is verified. The time dependence of the field variables are considered in this case, therefore the system of equations to be solved is Eq. (2.56) or a subset of the fields. Similarly to the validation of the static cases (see Section 2.10), the same material (PL127.10 from *Physik Instrumente Ceramic*) is used to run the simulations. Consistent mass and heat capacity matrices formulations are implemented for the transient analysis, with the Newmark method employed for the time integration algorithm (see Section 2.9.1).

### 2.11.1 Rayleigh Damping Coefficients

A very commonly used method for modelling the damping of structures is the Rayleigh damping method, in which two parameters ( $\alpha_R$  and  $\beta_R$ ) are selected (see Eq. (2.87)). A modal analysis of the PL127.10 actuator (refer to Fig. 2.10) is conducted in the FE Code, with no load applied. Mechanical constraints in all three directions are fixed along the left edge of the actuator (leaving the free length of 27 mm). Table 2.6 provides the first five natural frequencies of the bimorph. These frequencies can be used to help determine the Rayleigh damping coefficients of this actuator using Eq. (2.87) with knowledge of the first and second bending frequencies, which are, for this case, 443.74 Hz and 2760.52 Hz.

Modal Analysis - Bimorph PL127.10 (31×9.6×0.67) [mm]	
Mode number	Frequency [Hz]
1	443.74
2	2454.45
3	2760.52
4	5668.79
5	7723.75

Table 2.6 First 5 natural frequencies of the PL127.10 actuator

A damping ratio ( $\zeta$ ) of 0.05 is assumed and Eq. (2.87) becomes the system of equations

$$\begin{aligned}\zeta_1 &= \frac{\alpha_R}{2\omega_1} + \frac{\beta_R\omega_1}{2} \\ \zeta_2 &= \frac{\alpha_R}{2\omega_2} + \frac{\beta_R\omega_2}{2}\end{aligned}\tag{2.88}$$

Eq. (2.88) is solved and the coefficients  $\alpha_R$  and  $\beta_R$  are found to be 240.20 and  $4.97 \times 10^{-6}$ . These parameters are used for all the analyses in this transient validation section.

### **2.11.2 Three-Dimensional Solid Element**

This section focuses on verifying the transient analysis for three-dimensional solid elements with reduced integration (C3D20R). The solution involves solving Eq. 2.56, where the active degrees of freedom in the system are exclusively the mechanical degrees of freedom.

#### **2.11.2.1 Three-Dimensional Solid Transient Case**

This case provides an example of a transient analysis involving ramp signal forces of 1 N applied at the edge nodes, at the tip the actuator (see Fig. 2.11).

Fig. 2.20 shows the displacement in the  $z$ -direction for the node at the tip of the bimorph (see Fig. 2.19) versus time, while Fig. 2.21 presents the transverse deflection through the length of the actuator at time  $t = 1$  second, along the neutral axis. The maximum deflection in the numerical analysis is approximately 0.75 mm and has excellent agreement with the results from ABAQUS.

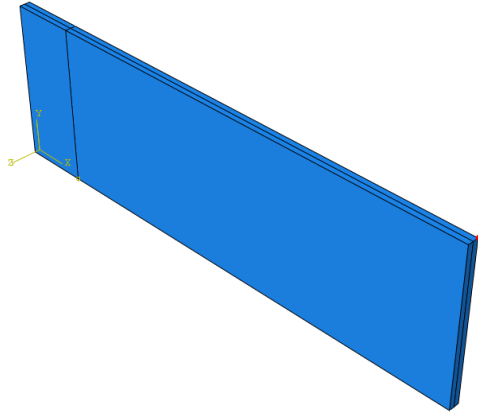


Fig. 2.19 Node of interest (red point)

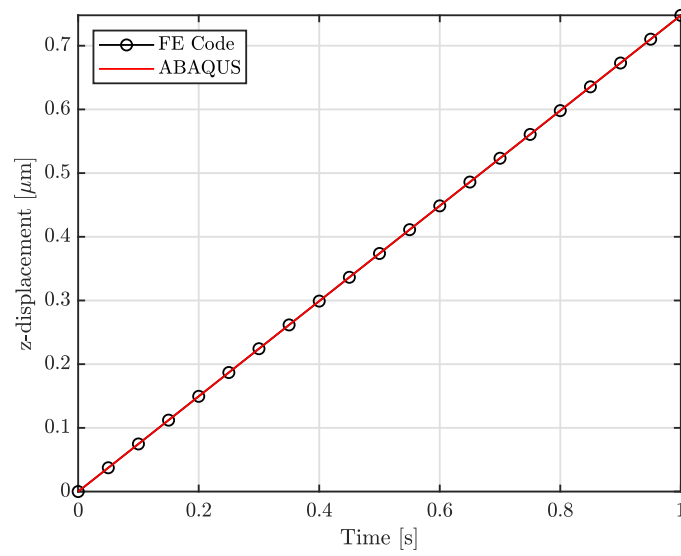


Fig. 2.20 Time versus nodal  $z$ -displacement at reference node

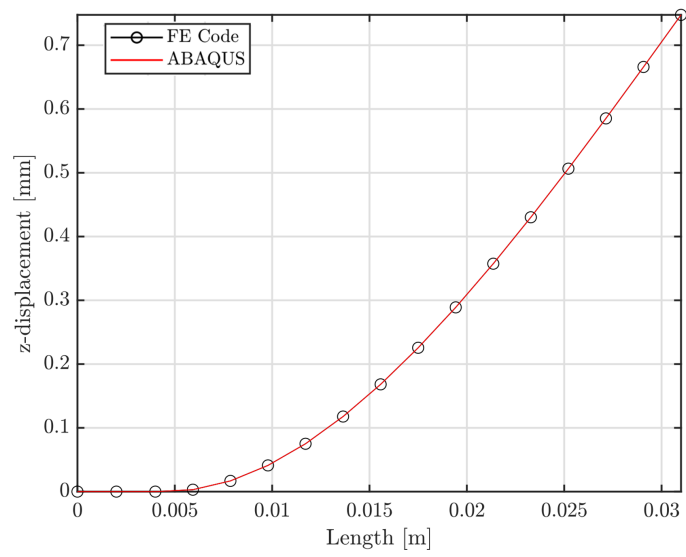


Fig. 2.21 Transverse deflection at time  $t = 1$  second across the length of the actuator

### 2.11.3 Piezoelectric Element

This section covers the verification of transient analyses for piezoelectric elements with reduced integration (C3D20RE). In this case, the active degrees of freedom in the system are the mechanical and electrical ones.

#### 2.11.3.1 Piezoelectric Transient Case

This simulation considers the transient analysis where the converse piezoelectric effect is investigated. The bimorph is subjected to voltages of 100 V in parallel connection with a sinusoidal wave  $A(t) = \sin(2\pi t f)$  showed in Fig. 2.22, where the frequency  $f$  is 1 Hz.

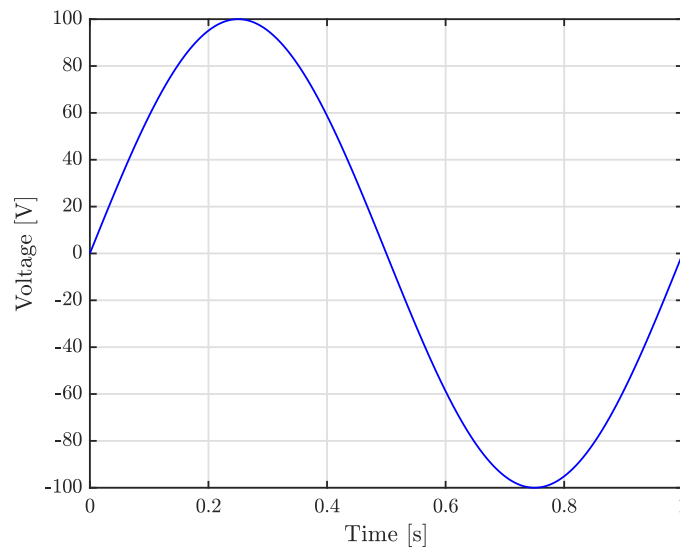


Fig. 2.22 Sinusoidal wave

The developed nodal  $z$ -displacement at the tip of the actuator (see Fig. 2.19) is seen in Fig. 2.23, where the deflection ranges from -0.08 mm to 0.08 mm. Additionally, Fig. 2.24 presents the transverse deflection of the bimorph at the times  $t = 0.25$  seconds and  $t = 0.75$  seconds through the length of the actuator at the middle of the thickness. The maximum and minimum deflections of 0.08 mm and -0.08 mm can be observed and the results showed an excellent agreement between the numerical analysis and the commercial software.

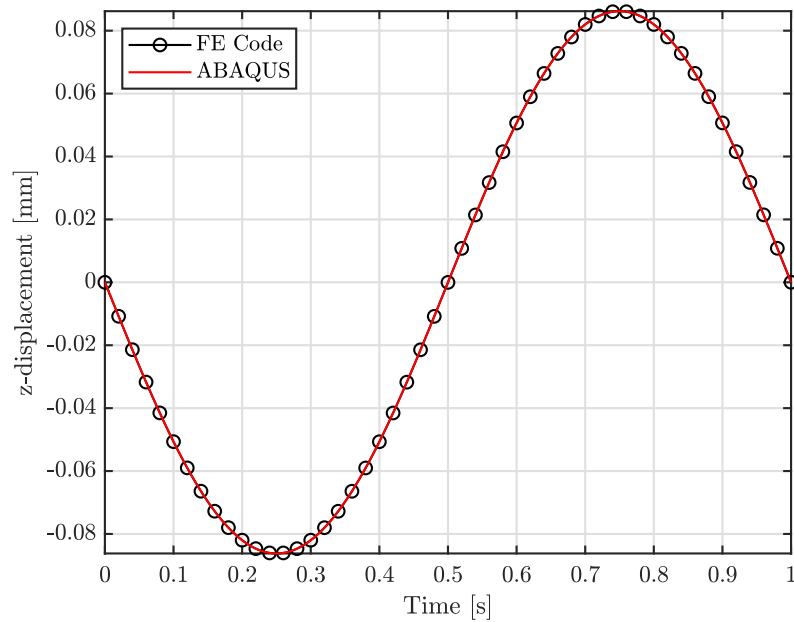


Fig. 2.23 Time versus nodal  $z$ -displacement at reference node (node 4)

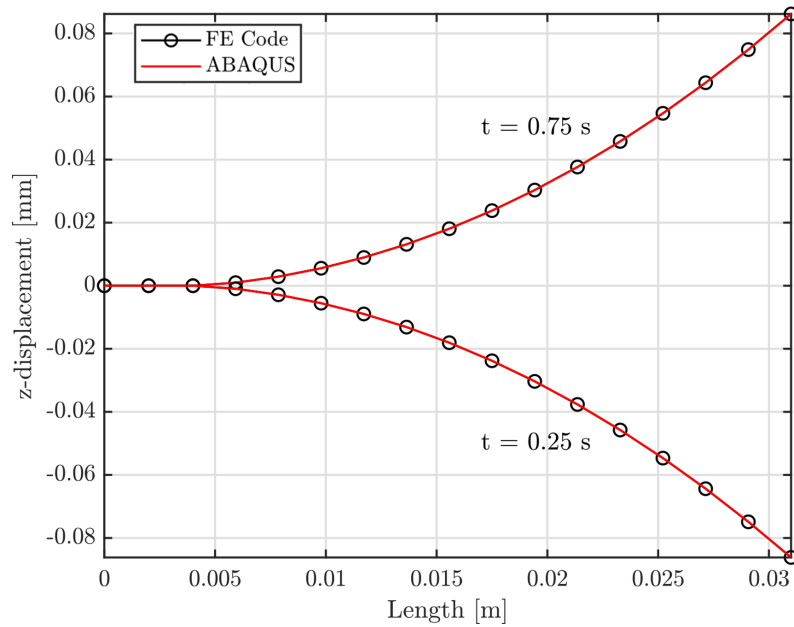


Fig. 2.24 Transverse deflection at time  $t = 0.25$  seconds and  $0.75$  seconds

#### 2.11.4 Thermoelastic Element

This section discusses the verification of thermoelastic elements with reduced integration (C3D20TR) in transient analyses. In this case, the equation of interest is Eq. (2.56), and the active degrees of freedom in the system are mechanical and thermal degrees of freedom.

##### 2.11.4.1 Thermoelastic Transient Case

The top surface of the bimorph is subjected to a sinusoidal temperature rise of 20 K ( $\theta = \theta_0 \sin(\pi t f / 2)$ ), while the bottom surface is set to a constant temperature of

273.15 K (refer to Fig. 2.25 for the sinusoidal waveform). Due to the thermal load on the top surface of the bimorph, the actuator bends down in the  $z$ -direction. Fig. 2.26 shows the bimorph deflection for both the numerical analysis and ABAQUS. Both results have an excellent agreement, where the implemented code and ABAQUS converge to the same maximum displacement of approximately -0.07 mm.

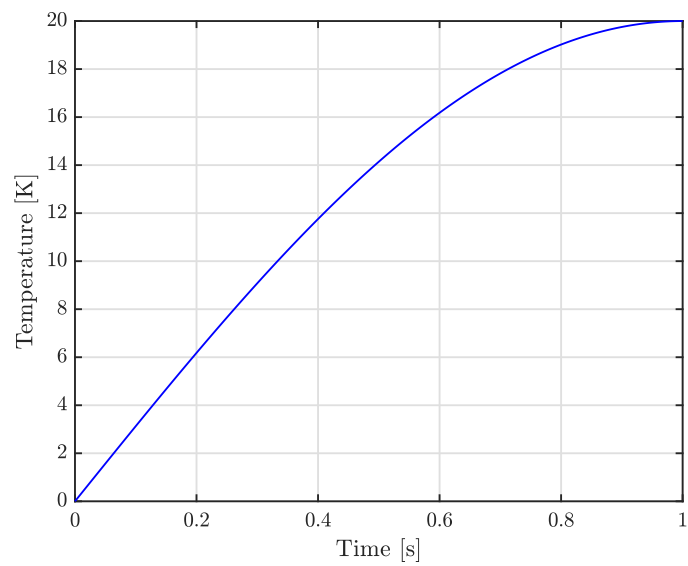


Fig. 2.25 Sinusoidal thermal load applied in time

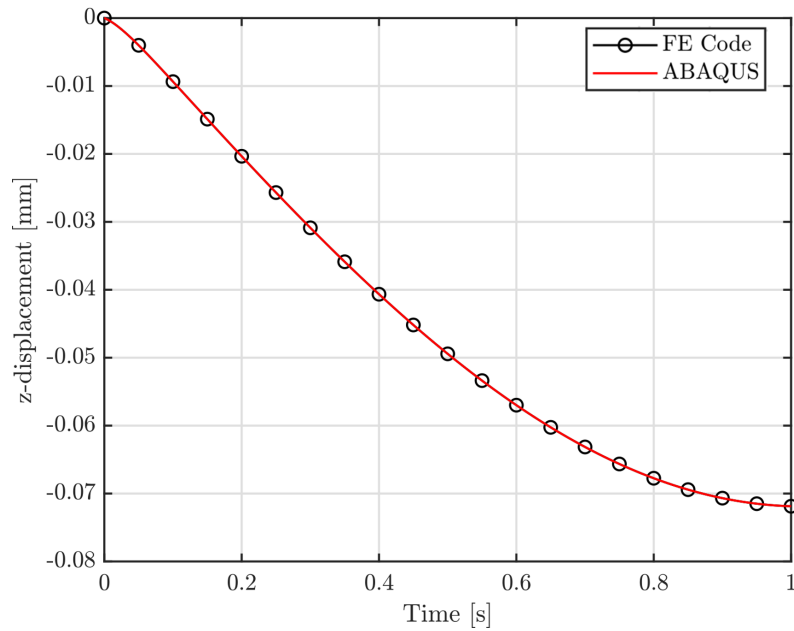


Fig. 2.26 Deflection of the bimorph at reference node due to thermal load

## 2.12 Thermopiezoelectric Element

A benchmark problem was proposed by Tauchert [86] in 1997 for evaluating the validity of the coupling effects in a five-layer plate made of two piezoelectric layers, one isotropic layer, and two orthotropic layers with  $0^\circ$  and  $90^\circ$  orientations.

The laminate configuration for the benchmark problem is shown in Fig. 2.27. The five-layer plate has a width to thickness ratio of  $b/t = 5$  with an assumed plane strain state. The width  $b$  is set to 50 mm and the thickness  $t$  is set to 10 mm, with each layer of the thickness being 2 mm. The material parameters for each layer is shown in Table 2.7.

This benchmark problem was proposed and analytically solved in 2D by Tauchert [86], and numerically investigated by Gornandt and Gabbert [4]. Furthermore, Shang et.al [93] verified the same benchmark problem with a 3D model, in a sequentially coupled analysis procedure in ABAQUS.

This work uses a finite element implementation in MATLAB (FE Code) that considers the fully-coupled equations of thermopiezoelectricity, and compares the obtained results to the previous investigations.

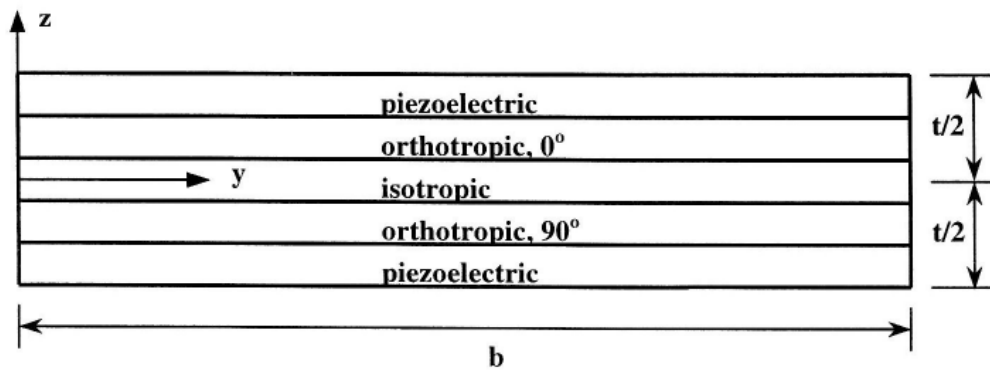


Fig. 2.27 Laminate configuration. (Source: [4])

Material	Coefficient	Value	Unit
Piezoelectric layer	Young's Modulus	$E = 2 \times 10^9$	N/m <sup>2</sup>
	Poisson's Ratio	$\nu = 0.25$	
	Thermal expansion	$\alpha = 1 \times 10^{-5}$	1/K
	Thermal conductivity	$\lambda = 1$	W/(Km)
	Electric permittivity	$\varepsilon_{11} = \varepsilon_{22} = 1 \times 10^{-8}$ $\varepsilon_{33} = 1 \times 10^{-7}$	F/m
	Electric permittivity clamped	$\varepsilon_{11} = \varepsilon_{22} = 0.5 \times 10^{-8}$ $\varepsilon_{33} = 0.6 \times 10^{-7}$	F/m
	Pyroelectric	$p = 0.25 \times 10^{-3}$	C/(m <sup>2</sup> K)
	Piezoelectric strain	$d_{31} = d_{32} = d_{24} = 2 \times 10^{-10}$ $d_{33} = 2.8 \times 10^{-10}$	m/V
Isotropic layer	Young's Modulus	$E = 2 \times 10^9$	N/m <sup>2</sup>
	Poisson's Ratio	$\nu = 0.25$	
	Thermal expansion	$\alpha = 1 \times 10^{-5}$	1/K
	Thermal conductivity	$\lambda = 1$	W/(Km)
Orthotropic layer 90°	Engineering constants	$E_1 = 1.8 \times 10^{11}$ $E_2 = 1.8 \times 10^{11}$ $G_{12} = G_{13} = 8 \times 10^9$ $G_{23} = 3 \times 10^9$	N/m <sup>2</sup>
	Poisson's Ratio	$\nu_{12} = \nu_{13} = \nu_{23} = 0.25$	
	Thermal expansion	$\alpha_1 = 2 \times 10^{-9}$ $\alpha_2 = \alpha_3 = 2 \times 10^{-6}$	1/K
	Thermal conductivity	$\lambda_1 = 100$ $\lambda_2 = \lambda_3 = 1$	W/(Km)

Table 2.7 Material parameters for the considered five-layer plate. (Source: [4])

The plate is subjected to a sinusoidal thermal load  $\theta = \theta_0 \sin(\pi y/b)$  at the bottom surface ( $-t/2$ ), while the top surface ( $t/2$ ) and the ends of the plate ( $y = 0, b$ ) are held fixed at 273.15 K. The electric potential at the inner surfaces as well as at the ends of the plate are set to zero, while distributions of the electric potential can arise on the outer surfaces. The mechanical boundary conditions are that the

plate is assumed to be simply supported.

For the investigation of this problem, the laminate is discretized using  $20 \times 10 \times 1$  quadratic elements, C3D20T (thermoelastic), C3D20E (piezoelectric), or C3D20TE (thermopiezoelectric), depending on the type of simulation being investigated. The first simulation neglects the piezoelectric and pyroelectric coupling effects, allowing for comparison with the analytical solution provided by Tauchert [86] as well as with the numerical solution presented by Gornandt and Gabbert [4]. Second, the coupling effects (piezoelectric and pyroelectric) are incorporated into the simulation, and the obtained results are compared with the results of Gornandt and Gabbert [4]. Due to the temperature load on the bottom surface, the plate curves in the  $z$ -direction and Fig. 2.28 presents the normalized displacement  $z^*$  ( $z^* = zt/(\alpha_0\theta_0b^2)$ ), where  $\alpha_0 = 1 \times 10^{-5} \text{ K}^{-1}$  and  $\theta_0 = 50 \text{ K}$ ) in the thickness direction at the center cross section of the plate for both the uncoupled and coupled simulations. The uncoupled simulation shows that the developed code provides an excellent agreement with both the analytic solution (Analytic uncoupled) [86] and the numerical solution (Magdeburg uncoupled) [4], resulting in a maximum error of around 0.3% when compared to the analytic solution, and a maximum result difference of around 0.11% when compared to the numerical solution presented by Madgeburg. The coupled simulation (considering both pyroelectric and piezoelectric coupling effects) also shows exceptional agreement with the numerical solution proposed by Gornandt

and Gabbert (Magdeburg coupled) [4], with the maximum difference between the results being approximately 0.09%.

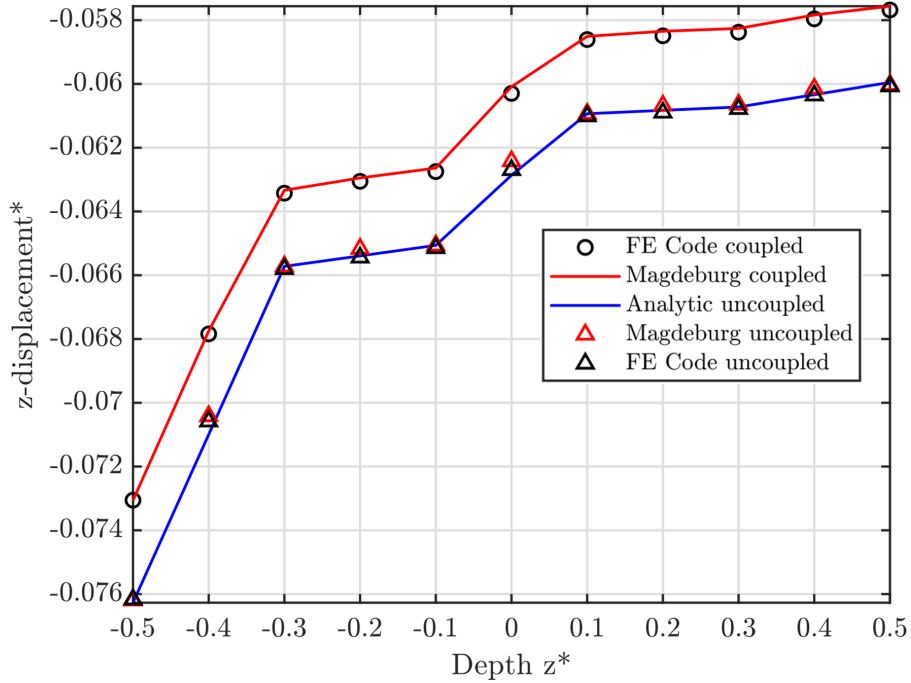


Fig. 2.28 Non-dimensional transverse deflection

The difference of the induced electric potential on the bottom surface of the lower piezoelectric layer ( $y = -t/2$ ) is presented in Fig. 2.29, where the first simulation considers both the pyroelectric and piezoelectric effects, and the second simulation only accounts for the piezoelectric effect. The results of the developed code for both simulations have an excellent agreement with the numerical results produced by Gornandt and Gabbert [4], implying the validity of the developed numerical procedure. Additionally, the results reveal that the pyroelectric effect can be of

great importance and should be considered in thermopiezoelectric applications.

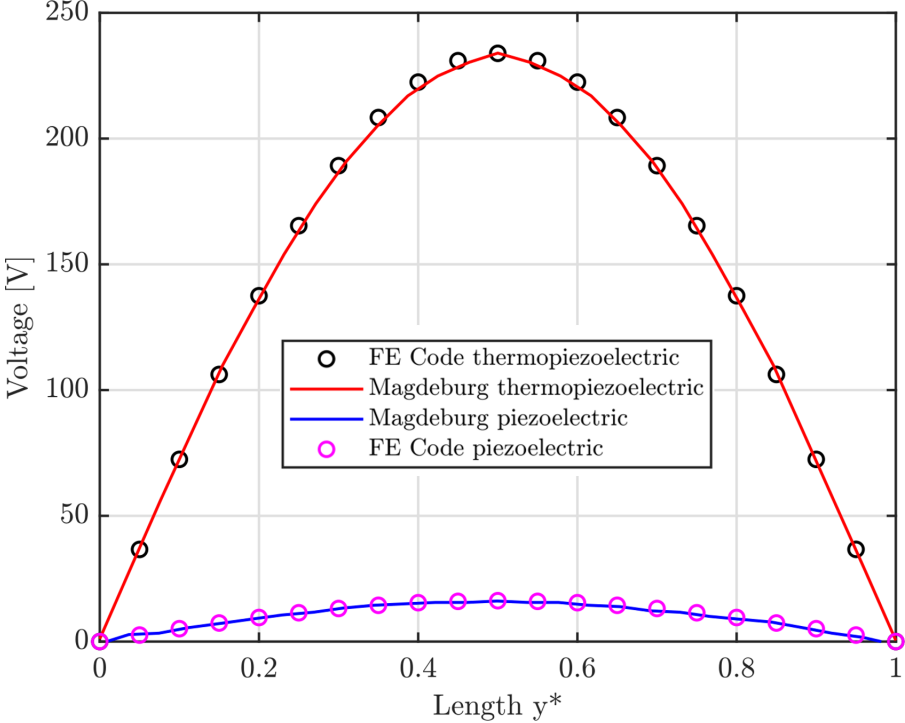


Fig. 2.29 The induced electric potential at  $[y^*, -0.5t]$  due to a thermal load

### 3 Examination of the Thermopiezoelectric Effect in Multilayer Stack Actuators

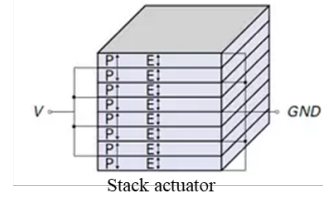
Piezoelectric stack actuators are multi-layered ceramic actuators that convert electrical energy into longitudinal mechanical displacement with high precision, force, and speed [2, 51]. This section investigates the coupled effects of thermopiezoelectricity in a P-887.51 stack actuator from *Physik Instrumente Ceramic* [2] (see Fig. 3.1(a)), whose specifications are shown in Table 3.1. The material parameters of the stack actuator P-887.51 are presented in Table 3.2. Fig. 3.1(b) shows the diagram of how the electrical connections are made in a multi-layer stack actuator, along with the polarization direction.

Piezoceramic actuator	Dimensions [mm]	Nominal travel range [ $\mu\text{m}$ ]	Operating voltage [V]
P-887.51	7 $\times$ 7 $\times$ 18	15	100

Table 3.1 P-887.51 specifications. (Source: [2])



(a) P-887.51 model



(b) Electrical diagram

Fig. 3.1 Multilayer stack actuator (Source: [2])

Material coefficients P-887.51		
Coefficient	Unit	Value
Compliance matrix	$\frac{\text{N}}{\text{m}^2}$	$C = \begin{bmatrix} 1.229 \times 10^{11} & 7.660 \times 10^{10} & 7.017 \times 10^{10} & 0 & 0 & 0 \\ 7.660 \times 10^{10} & 1.229 \times 10^{11} & 7.017 \times 10^{10} & 0 & 0 & 0 \\ 7.017 \times 10^{10} & 7.017 \times 10^{10} & 9.705 \times 10^{10} & 0 & 0 & 0 \\ 0 & 0 & 0 & 2.315 \times 10^{10} & 0 & 0 \\ 0 & 0 & 0 & 0 & 2.226 \times 10^{10} & 0 \\ 0 & 0 & 0 & 0 & 0 & 2.226 \times 10^{10} \end{bmatrix}$
Piezoelectric stress matrix	$\frac{\text{N}}{\text{Vm}}$	$e = \begin{bmatrix} 0 & 0 & 0 & 0 & 12.444 & 0 \\ 0 & 0 & 0 & 17.735 & 0 & 0 \\ -7.841 & -7.841 & 13.559 & 0 & 0 & 0 \end{bmatrix}$
Dielectric matrix	$\frac{\text{F}}{\text{m}}$	$\varepsilon = \begin{bmatrix} 1.638 \times 10^{-8} & 0 & 0 \\ 0 & 1.638 \times 10^{-8} & 0 \\ 0 & 0 & 1.550 \times 10^{-8} \end{bmatrix}$
Mass density	$\frac{\text{kg}}{\text{m}^3}$	$\rho = 7800$
Heat conduction matrix	$\frac{\text{W}}{\text{mK}}$	$\lambda = \begin{bmatrix} 1.1 & 0 & 0 \\ 0 & 1.1 & 0 \\ 0 & 0 & 1.1 \end{bmatrix}$
Thermal expansion matrix	$\frac{1}{\text{K}}$	$\alpha = \begin{bmatrix} 6 \times 10^{-6} \\ 6 \times 10^{-6} \\ -5 \times 10^{-6} \\ 0 \\ 0 \\ 0 \end{bmatrix}$
Pyroelectric matrix	$\frac{\text{C}}{\text{m}^2\text{K}}$	$p = \begin{bmatrix} 0 \\ 0 \\ -6 \times 10^{-4} \end{bmatrix}$
Heat capacity coefficient	$\frac{\text{J}}{\text{K}}$	$c_v = 350$

Table 3.2 Material parameters of the P-887.51 actuator. (Source: [2])

### 3.1 Scaling Factor and Validation

Table 3.1 presents the nominal displacement of the stack actuator for an operating voltage of 100 V with the nominal operating voltage lying between 0 and 120 V. Stack actuators are composed of multiple piezoelectric layers stacked on top of each other with alternating polarity, and the nominal displacement is the sum of the displacements of each of these layers. The longitudinal displacement of a stack actuator is given as

$$\Delta l = d_{33}nV \quad (3.1)$$

where  $\Delta l$  [m] is the longitudinal displacement,  $d_{33}$  [m/V] is the longitudinal piezoelectric charge coefficient,  $n$  is the number of layers, and  $V$  [V] is the operating voltage. In order to determine the number of layers of the P-887.51 actuator, the nominal displacement ( $15 \times 10^{-10}$  [m]) and the piezoelectric coefficient  $d_{33}$  ( $4.00 \times 10^{-10}$  [m/V]) are substituted into  $\Delta l$  and  $d_{33}$  terms. The solution of this equations yields 375 layers.

For the purpose of initial model verification, the number of layers is set to 1, and the voltage is scaled. When  $n$  is specified as one in Eq. (3.1), the necessary operating voltage to produce the same displacement is 37500 V. To demonstrate that the scaling produces displacement results consistent with those provided by *PI Ceramics*, a static model is created in ABAQUS. In this model, the bottom of

the actuator is mechanically constrained and set to ground, while the top surface is set to -37500 V.

The deflection obtained by both ABAQUS and MATLAB is 14.56  $\mu\text{m}$  (see Fig. 3.2). This amounts to a difference of 2.98% compared to the nominal displacement provided by the company specifications of 15  $\mu\text{m}$  (which allows for a tolerance of  $\pm 20\%$ ).

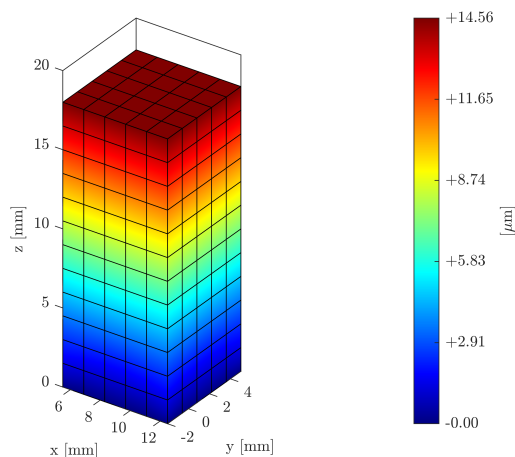


Fig. 3.2 Displacement of the stack actuator with voltage scaling for the nominal displacement

## 3.2 Rotation Matrices

To run simulations involving multiple layers, where each of these layers have opposite material orientations, leading to opposing polarization directions, rotation matrices must be employed. Consideration of material orientation can be incor-

porated via rotation matrices along with the material constitutive matrices. As the actuator stack direction aligns with the  $z$ -direction or 3-axis, a  $180^\circ$  rotation around the  $x$ -direction (or 1-axis) will yield the required orientation of the polarization direction.

A general rotation around the 1-axis can be written as

$$R = \begin{bmatrix} 1 & 0 & 0 \\ 0 & \cos(\beta) & -\sin(\beta) \\ 0 & \sin(\beta) & \cos(\beta) \end{bmatrix} \quad (3.2)$$

And the strain transformation matrix can be described as

$$T = \begin{bmatrix} 1 & 0 & 0 & 0 & 0 & 0 \\ 0 & \cos^2(\beta) & \sin^2(\beta) & 2\sin(\beta)\cos(\beta) & 0 & 0 \\ 0 & \sin^2(\beta) & \cos^2(\beta) & -2\sin(\beta)\cos(\beta) & 0 & 0 \\ 0 & -\cos(\beta)\sin(\beta) & \cos(\beta)\sin(\beta) & \cos^2(\beta) - \sin^2(\beta) & 0 & 0 \\ 0 & 0 & 0 & 0 & \cos(\beta) & -\sin(\beta) \\ 0 & 0 & 0 & 0 & \sin(\beta) & \cos(\beta) \end{bmatrix} \quad (3.3)$$

where  $\beta$  is the angle of rotation. Applying the transformations to the piezoelectric constitutive matrices, the compliance matrix becomes [?]

$$C' = TCT^T \quad (3.4)$$

where  $T^T$  is the transpose of the strain transformation matrix. The transformed piezoelectric strain coefficients can be written as

$$d' = RdT^T \quad (3.5)$$

and the transformed permittivity matrix becomes

$$\varepsilon' = R\varepsilon R^T \quad (3.6)$$

where  $R^T$  is the transpose of the rotation matrix. The thermal matrices also must be transformed accordingly. Therefore, the thermal expansion matrix in the new coordinate system can be written as

$$\alpha' = T\alpha \quad (3.7)$$

The heat conduction coefficients matrix becomes

$$\lambda' = R\lambda R^T \quad (3.8)$$

And the pyroelectric matrix in the new coordinate system can be described as

$$p' = Rp \quad (3.9)$$

### 3.3 Step Input Signal

The first simulation involves the transient analysis of the stack actuator subjected to a step input signal. The voltage is applied as shown in Fig. 3.1(b). Each layer has an opposing polarization orientation to ensure the longitudinal mechanical displacement occurs in the same direction. The simulation runs for 1 second, featuring a step at  $t = 0.01$  seconds. Analyses are run for 1 layer, 7 layers, and the realistic model with 375 layers.

### 3.3.1 Step Input for a 1-Layer Model

The initial approach involves building a stack model using just 1 layer. As mentioned in Section 3.1, the voltage needs to be scaled up, resulting in a value of 37500 V. In this configuration, the bottom surface is grounded while the top surface of the actuator is set to the desired voltage. Fig. 3.4 demonstrates the voltage, along with the resulting deflection and temperature at the reference node (see Fig. 3.3 - corner of the actuator).

The application of the step signal generates a response of the actuator, leading to longitudinal mechanical displacement. Due to the coupled fields, a temperature develops throughout the actuator where it is evident that an impulse has occurred. This behavior arises from the multiplication of the  $K_{\theta\phi}$  matrix by the derivative of the electric potential  $\dot{\phi}$ , since the derivative of a step function produces an impulse response. A significant temperature spike of approximately 100 K is observed at the time of the step signal. This spike is due to the scaling factor, as the electric field can not be scaled in as intuitive a manner.

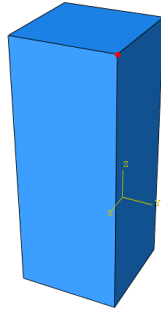


Fig. 3.3 Stack actuator modeled as 1-layer with the reference node highlighted

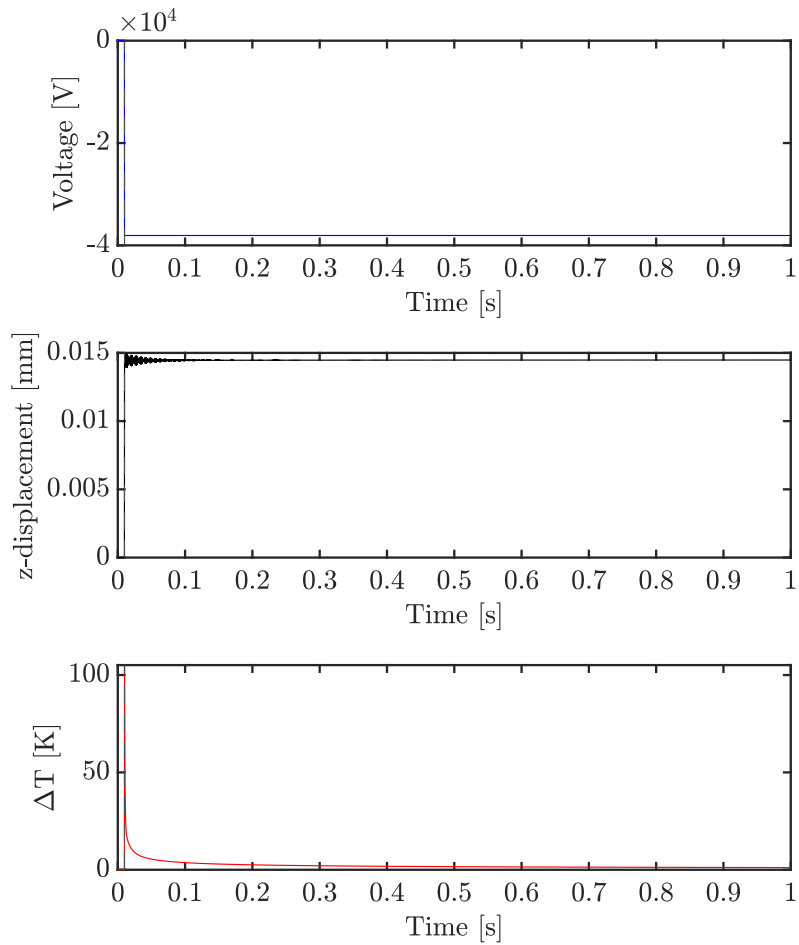


Fig. 3.4 Developed voltage,  $z$ -deflection, and temperature for the reference node

The developed temperature at time  $t = 0.5$  seconds is shown in Fig. 3.5, where a smooth and continuous temperature distribution across the actuator can be observed.

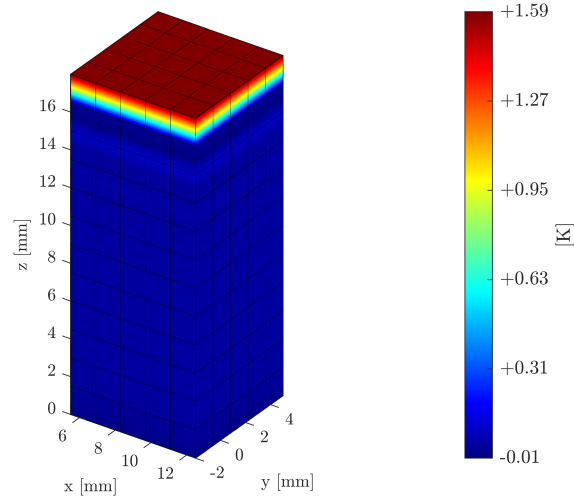


Fig. 3.5 Developed temperature due to step input for a 1-layer stack model

### 3.3.2 Step Input for a 7-Layer Model

A 7-layer model is built as an interim model as the number of layers in the model directly influence the temperature spike seen initially. In this case, the voltage is scaled to achieve the nominal displacement of  $15 \mu\text{m}$ , resulting in a scaled voltage of 5439 V. A diagram of how the voltage is applied to the surfaces of the actuator is shown in Fig. 3.6. The reference node is located at the top of the actuator, with original coordinates of (0.0125, 0.005, 0.018) mm (see Fig. 3.6).

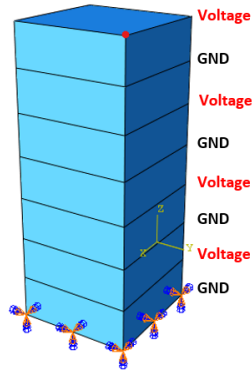


Fig. 3.6 7-layer stack actuator with electric connection and reference node

The results for the voltage, developed displacement, and temperature at the reference node are presented in Fig.3.7. Similar to the simulation with 1 layer, a significant temperature jump of approximately 70 K is observed, albeit reduced with the additional layers and hence the lower applied voltage. This leads to the conclusion that while voltage scaling is fine for the mechanical and electrical fields, to get an accurate representation of the thermal field, a realistic model with 375 layers should be simulated.

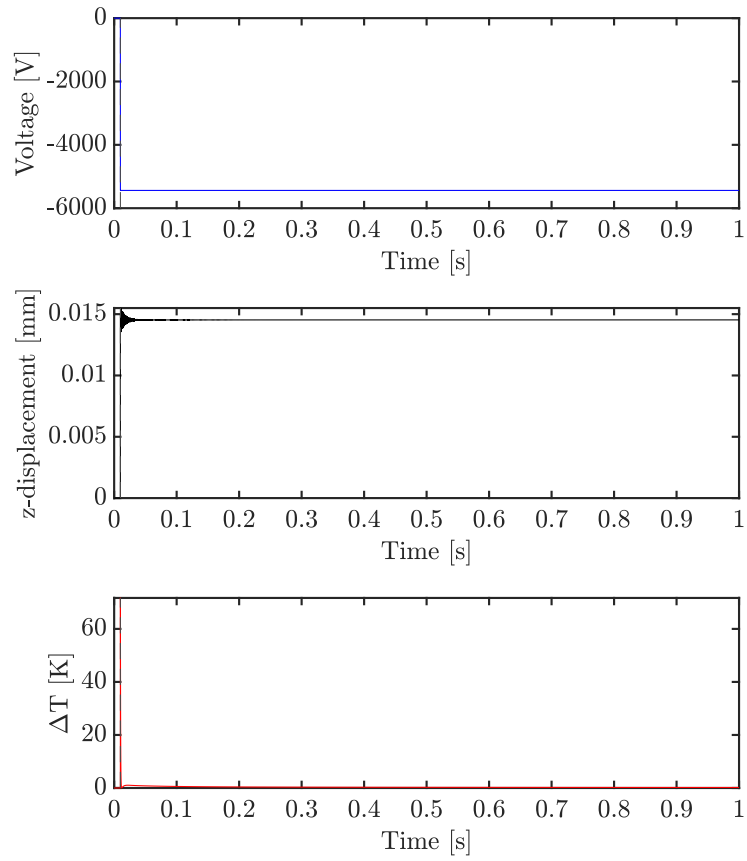


Fig. 3.7 Developed voltage,  $z$ -deflection, and temperature for the reference node

Fig. 3.8 shows the temperature of the actuator at the time of 0.5 seconds. The mesh profile shows a repeating temperature pattern across the stack actuator (exactly where the voltage is being applied). This phenomenon is a result of the pyroelectric coefficient getting switched with the polarization direction in each layer, where one side is positive, and the other is negative.

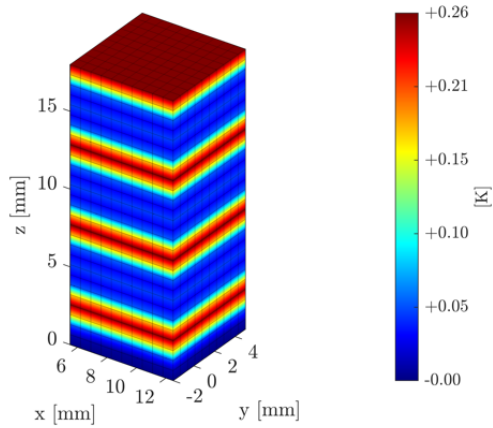


Fig. 3.8 Developed temperature of the 7-layer stack actuator due to a step input

The result for the developed displacement over time at the reference node (top of the actuator - see Fig. 3.6) is shown in Fig. 3.9 for both thermopiezoelectric and piezoelectric simulations. In the piezoelectric simulation, the thermal field is not taken into account. As expected, there is a damped oscillation in the piezoelectric simulation that decays to a constant final position. However, when temperature is incorporated into the analysis, an interesting phenomenon emerges as the actuator's position gradually drifts upward. This drift results in a slight change on the stack position of approximately 11 nm, which could hold significance in nan positioning applications [94, 95], and is reminiscent of the creep phenomenon seen in nan positioning applications.

The underlying reason for the thermopiezoelectric simulation demonstrating a smaller displacement than the piezoelectric simulation lies in the negative thermal

expansion coefficient  $\alpha_3$ . This coefficient leads to contraction of the stack actuator when subject to temperature with the pyroelectric effect responsible for the upward drift observed in the displacement. This occurs because the developed temperature increases the voltage, subsequently increasing the actuator's displacement.

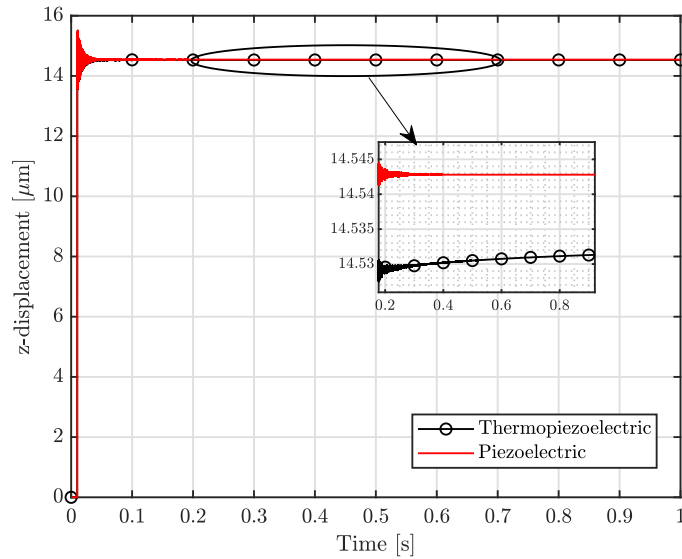


Fig. 3.9 Time versus  $z$ -displacement for thermopiezoelectric and piezoelectric simulations

### 3.3.3 Step Input for a 375-layer Model

A realistic model of the stack is created by dividing the actuator into 375 layers. In this case no scaling is necessary, hence 100 V and 0 V are alternately applied to the surfaces of each of the layers. The  $z$ -displacement is shown in Fig. 3.10.

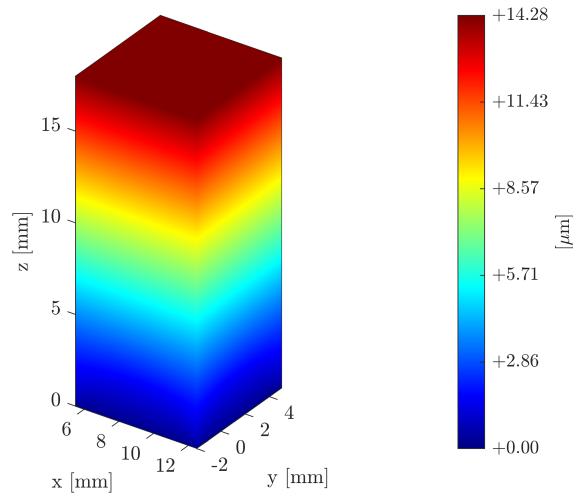


Fig. 3.10 Developed displacement of the 375-layer stack actuator due to a step input

Fig. 3.11(a) provides the temperature at the step time of 0.01 seconds. Here, no large temperature jumps are observed, with 0.62 K being the largest spike obtained. Due to the considerable number of layers and elements involved, the temperature profile in Fig. 3.11(a) is not be clear when viewed on a macro-scale. Consequently, a cross-sectional  $xz$  view is presented in Fig. 3.11(b), which provides a clearer observation of the developed temperature. This view reveals distinct red and blue regions indicating areas with higher and lower temperatures, respectively, that coincide with the positive and negative terminals at each layer.

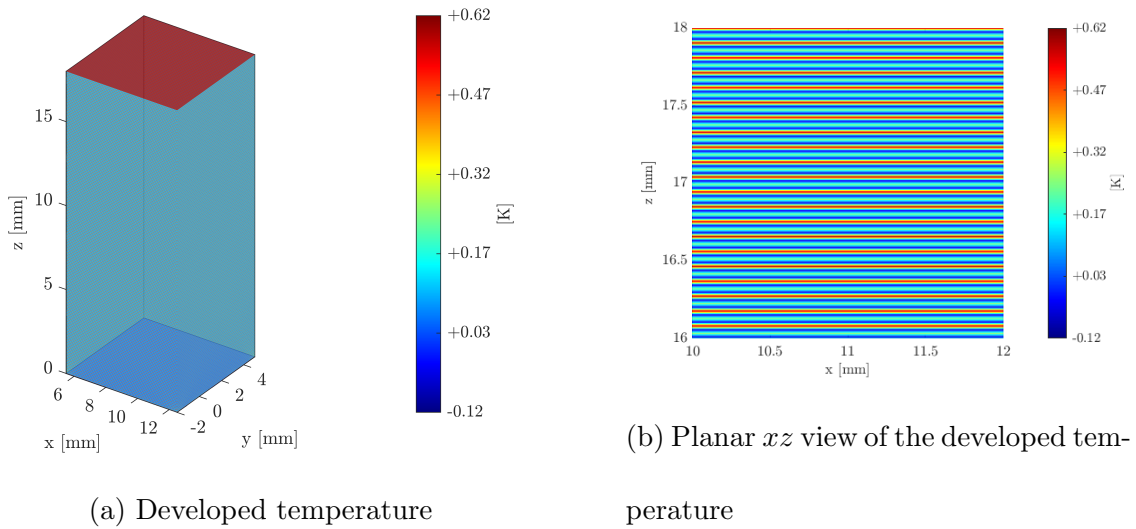


Fig. 3.11 Developed temperature of the 375-layer stack actuator

Fig.3.12 shows a comparison of the  $z$ -displacement across the length of the actuator for 1 layer, 7 layers, and 375 layers. This comparison is made at the final time increment of the simulation, and clearly demonstrates an excellent agreement among the results of these three simulations.

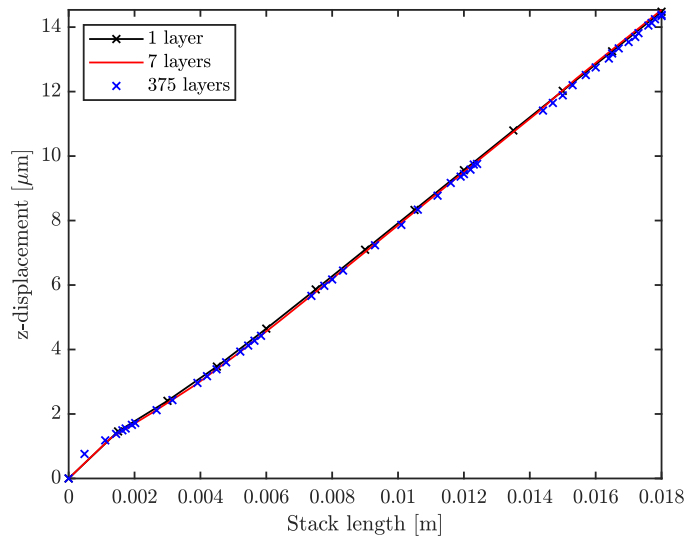


Fig. 3.12 Developed displacement in  $z$  through the length for 1 layer, 7 layers, and 375 layers

### 3.4 Thermal Load

In contrast to the previous cases where a step input was applied, this section investigates the behaviour of the stack actuator under a dynamic thermal load, particularly its impact on the electric potential and position of the actuator. This analysis involves the comparison of two simulations: one considering the pyroelectric effect and the other neglecting it. In these simulations, the top surface of the stack actuator is subjected to a sinusoidal temperature rise (see Fig. 3.13) with a magnitude of 10 K. The bottom surface maintains a constant temperature of 273.15 K. Boundary conditions are enforced to 0 V alternately on half the surfaces of the actuator, leaving the other half free to produce voltage, following the diagram

shown in Fig. 3.1(b).

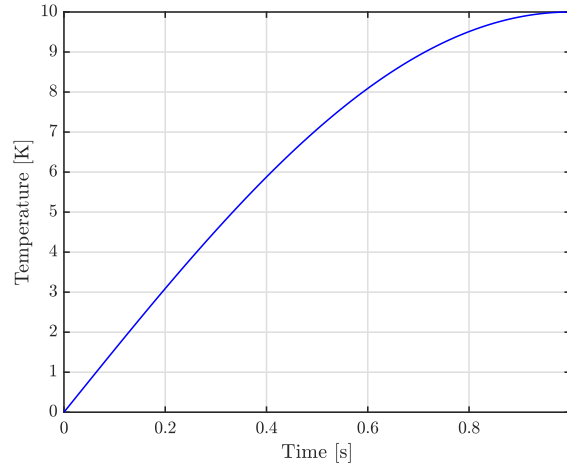
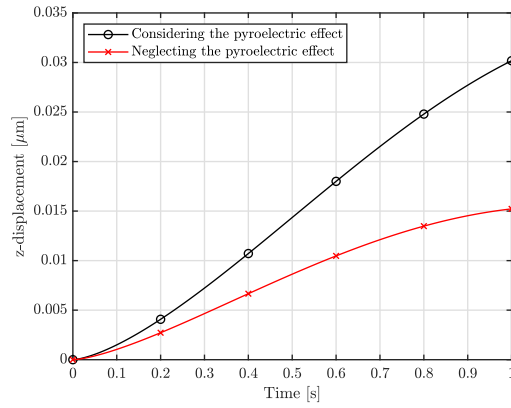


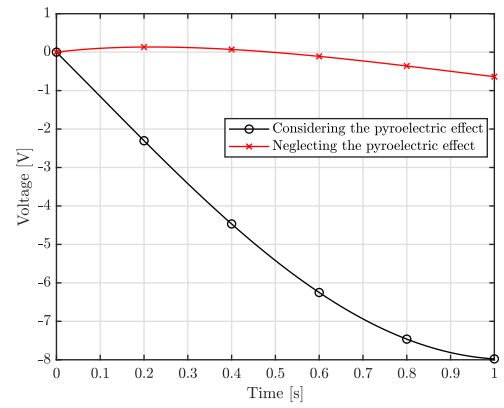
Fig. 3.13 Sinusoidal thermal load

Fig. 3.14(a) demonstrates the resulting displacement and Fig. 3.14(b) shows the generated voltage caused by the thermal load. Significant differences are evident between the results that consider the pyroelectric effect and those that neglect it. Specifically, in terms of developed displacement, accounting for the pyroelectric effect yields a result approximately twice as large as the simulation that disregards this effect (see Fig. 3.14(a)). In Fig. 3.14(b), the developed voltage in the simulation considering the pyroelectric effect is approximately 12.5 times larger than the voltage generated in the simulation that neglects the pyroelectric effect. This significant difference arises from the fact that although three fields are still considered (mechanical, electrical, and thermal), two couplings are missing, the pyroelectric and electrocaloric effects. That is the reason why the developed voltage is quite

small in this case.



(a) Developed displacement



(b) Developed voltage

Fig. 3.14 Stack actuator under thermal load considering the pyroelectric effect versus neglecting the pyroelectric effect

## 4 Examination of the Thermopiezoelectric Effect in Multimorph Bender Actuators

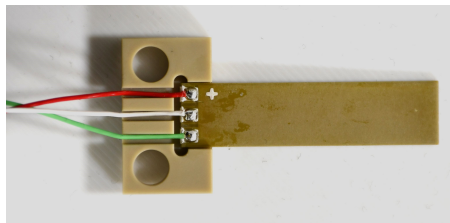
Multimorph bender actuators consist of two or more layers of piezoelectric ceramics bonded together [51, 64]. The difference to stack actuators lies in their mechanical behavior, where bender actuators generate bending. This section explores the behavior of thermopiezoelectric bimorph actuators when driven via two distinct electric field waveforms: a step input signal and a sinusoidal input signal. The final part of this chapter investigates the electric potential and displacement exhibited by the actuator when subjected to a dynamic thermal load.

The multimorph bender actuator examined in this section is the PB4NB2W model from *ThorLabs*. This bimorph actuator incorporates multiple piezoelectric ceramic layers, specifically two segments co-fired with five piezoelectric ceramic layers, resulting in a total of ten layers. The actuator offers a maximum displacement of  $\pm 450 \mu\text{m}$  with a tolerance of  $\pm 15\%$  [5]. Table 4.1 presents the specifications provided by *ThorLabs*, while Fig. 4.1 shows the PB4NB2W model (Fig. 4.1(a)) along

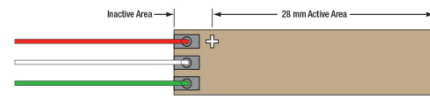
with its corresponding drawing (Fig. 4.1(b)).

PB4NB2W specifications	
Drive voltage range	0 - 150 V
Displacement at 150 V	$\pm 450 \mu\text{m}$
Dimensions	$32 \times 7.8 \times 0.8 \text{ mm}$
Free length	28 mm

Table 4.1 PB4NB2W bender actuator specifications (Source: [5])



(a) PB4NB2W bender actuator



(b) PB4NB2W actuator drawing

Fig. 4.1 Bimorph actuator. (Source: [5])

Table 4.2 presents the material properties of the PB4NB2W actuator. Rather than listing each coefficient individually, the matrices used in the simulations are presented.

Material coefficients PB4NB2W								
Coefficient	Unit	Value						
Compliance matrix	$\frac{N}{m^2}$	$C =$	$1.589 \times 10^{11}$	$1.130 \times 10^{11}$	$1.170 \times 10^{11}$	0	0	0
			$1.130 \times 10^{11}$	$1.589 \times 10^{11}$	$1.170 \times 10^{11}$	0	0	0
			$1.170 \times 10^{11}$	$1.170 \times 10^{11}$	$1.442 \times 10^{11}$	0	0	0
			0	0	0	$2.577 \times 10^{10}$	0	0
			0	0	0	0	$1.409 \times 10^{10}$	6
			0	0	0	0	0	$1.409 \times 10^{10}$
Piezoelectric stress matrix	$\frac{N}{Vm}$	$e =$	0	0	0	0	13.380	0
			0	0	0	24.484	0	0
			-3.914	-3.914	27.500	0	0	0
Dielectric matrix	$\frac{F}{m}$	$\varepsilon =$	$2.984 \times 10^{-8}$	0	0			
			0	$2.984 \times 10^{-8}$	0			
			0	0	$2.922 \times 10^{-8}$			
Mass density	$\frac{kg}{m^3}$	$\rho = 7700$						
Heat conduction matrix	$\frac{W}{mK}$	$\lambda =$	3.0	0	0			
			0	3.0	0			
			0	0	3.0			
Thermal expansion matrix	$\frac{1}{K}$	$\alpha =$	$0.25 \times 10^{-6}$					
			$0.25 \times 10^{-6}$					
			$-3.17 \times 10^{-6}$					
			0					
			0					
			0					
Pyroelectric matrix	$\frac{C}{m^2K}$	$p =$	0					
			0					
			$-6 \times 10^{-4}$					
Heat capacity coefficient	$\frac{J}{K}$	$c_v = 420$						

Table 4.2 Material parameters of PB4NB2W actuator. (Source: [5])

Section 4.1 examines the thermopiezoelectric effect in bender actuators focusing on the maximum displacement offered. The driving method used for this purpose is the differential voltage control method. Then, in Section 4.2, simulations under a step input signal, and a sinusoidal wave signal are considered. The results obtained from the implemented code are compared to those from ABAQUS. In the developed code, the fully coupled thermopiezoelectric equations are consid-

ered, while ABAQUS only takes the piezoelectric effect into account, contrasting the differences between thermopiezoelectric simulations (where the thermal field is considered) and piezoelectric simulations (where the thermal field is neglected). Lastly, Section 4.2.3 considers the evaluation of the influence of a dynamic thermal load on the electric field and displacement of the bender actuator.

#### 4.1 Differential Voltage Control for Displacement Test

A static analysis is performed in ABAQUS to verify the displacements and compare them with the maximum displacement provided by *ThorLabs*. One of the driving techniques for bender actuators is the differential voltage control method. In this method (see Fig. 4.1(b)), the red wire is set to a constant bias of 150 V, the white wire is the drive signal which varies from 0 V to 150 V, and the green wire is set to 0 V. Alternatively, voltages can be applied by setting the red wire to 75 V, the white wire from -75 V to 75 V, and the green wire to -75 V (see Table 4.3).

Differential voltage control			
Option	Red wire	White wire	Green wire
1	150 V	0 V to 150 V	0 V
2	75 V	-75 V to 75 V	-75 V

Table 4.3 Differential voltage control

The configuration for applying voltage to a multilayer bender actuator is shown in Fig. 4.2. In this arrangement, each layer exhibits opposite polarization, except for

the middle layers [2]. The polarization direction and electric field orientations for the PB4NB2W 10-layer bender actuator are demonstrated in Fig. 4.3, with colors corresponding to Table 4.3. The polarization direction for the white color is oriented in the positive  $z$ -direction, while for the red and green colors (illustrating the red and green wires from the actuator) the polarization is in the negative  $z$ -direction.

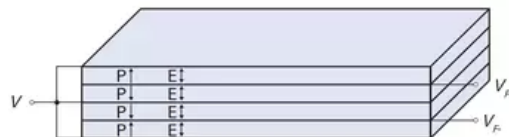


Fig. 4.2 Polarization direction and voltage application to a multilayer bender actuator. (Source: [2])

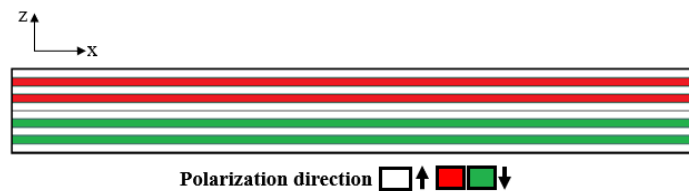


Fig. 4.3 PB4NB2W diagram -  $xz$  view: polarization direction

#### 4.1.1 Displacement Test 1

For the test, option 1 from Table 4.3 is selected. The initial simulation involves a static analysis, where 150 V is applied to the surfaces corresponding to the positive

terminal (red wire), 150 V to the surfaces that corresponds to the drive signal (white wire), and 0 V to the surfaces corresponding to the negative terminal (green wire). The material coefficients utilized are presented in Table 4.2. The bender is mechanically constrained in the  $x$ ,  $y$ , and  $z$  directions, as illustrated in Fig. 4.4, leaving a free length of 28 mm.

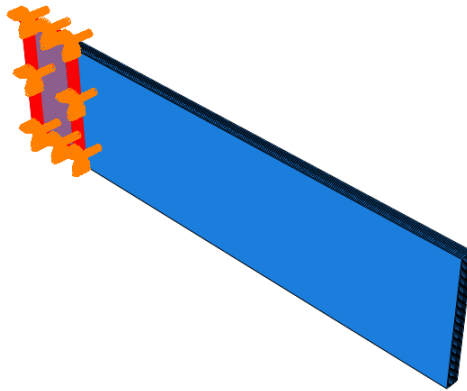


Fig. 4.4 Bender actuator model with mechanical boundary conditions depicted

The displacement result from MATLAB is demonstrated in Fig. 4.5, presenting a maximum deflection of  $-450.4 \mu\text{m}$ . The maximum displacement specified by *ThorLabs* is  $-450 \mu\text{m}$ . The difference between these two values is approximately 0.09%. This initial test confirms the simulation's accuracy in MATLAB.

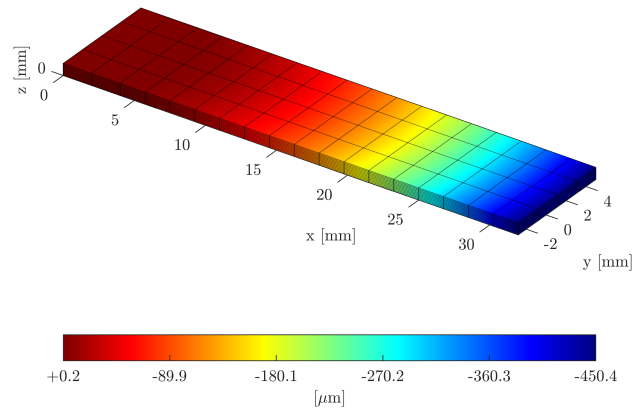


Fig. 4.5 Developed displacement of the bender actuator due to a constant bias of 150 V and a variable voltage of 150 V

#### 4.1.2 Displacement Test 2

The second test also involves a static analysis, differing only in the application of 0 V to the white wire instead of 150 V. The mesh contour and displacement results obtained from the simulation in MATLAB are presented in Fig. 4.6. Notably, this time, the deflection is positive (+ 450.4 μm) due to the change in variable voltage from 150 V to 0 V.

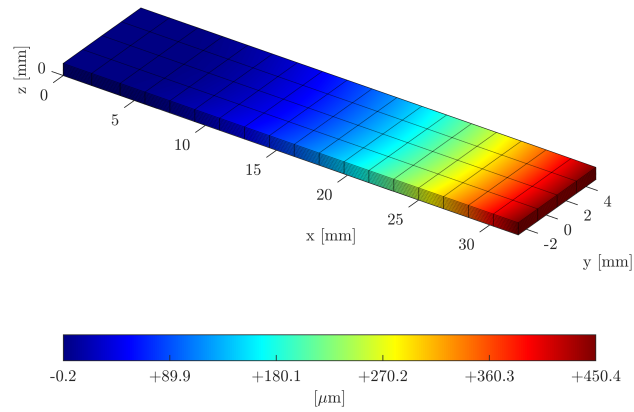


Fig. 4.6 Developed displacement of the bender actuator due to a constant bias of 150 V and a variable voltage of 0 V

## 4.2 Transient Analysis

A comparison is made between the results obtained from the implemented finite element code and those from ABAQUS. In the FE Code, the fully coupled thermopiezoelectric equations are taken into account, while ABAQUS only considers piezoelectric simulations, neglecting the thermal field.

### 4.2.1 Step Input

The first simulation involves a transient analysis for a common drive signal, specifically a step input signal. Fig. 4.3 demonstrates how the voltage is applied along with the polarization direction. The node of interest is located at the tip of the actuator (see Fig. 4.7).

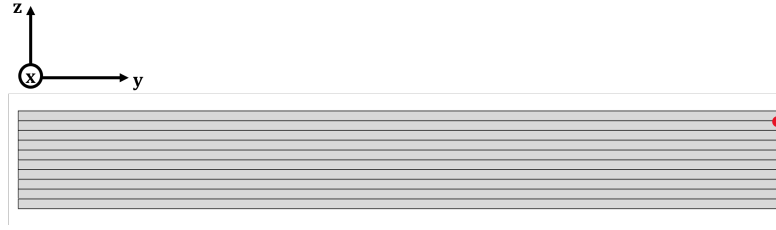
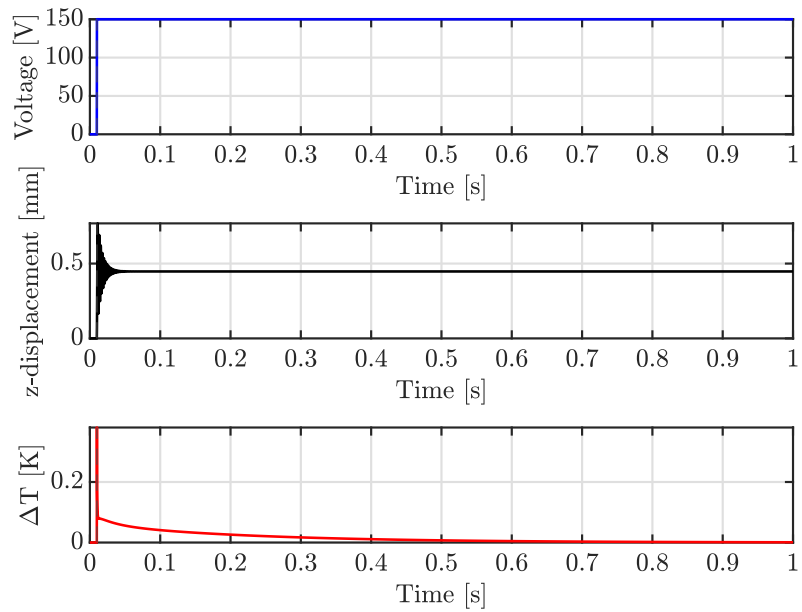


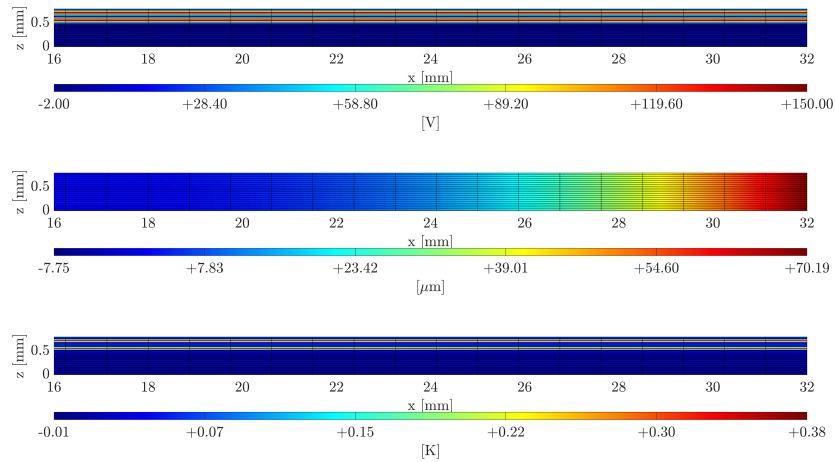
Fig. 4.7 Reference node (red dot) in  $yz$  view

Fig. 4.8(a) provides the graphs for the voltage, developed deflection and temperature for the reference node at the tip of the actuator due to the step input (refer to Fig. 4.7). Applying a 150 V voltage causes the bimorph to bend upwards and maintain its position due to the step input. The actuator experiences initial oscillation, primarily due to the low damping factor, then followed by maintaining its position at approximately 450  $\mu\text{m}$  for the remainder of the simulation. A temperature variation of approximately 0.38 K is observed in Fig. 4.8(b), with the highest peak occurring at the step time ( $t = 0.01$  seconds).

The voltage, deflection, and temperature at time  $t = 0.01$  seconds in a  $xz$ -view cut is shown in Fig. 4.8(b). The developed temperature showed in all the layers of the actuator confirms that the surfaces to which the voltage is applied experience the highest temperatures.



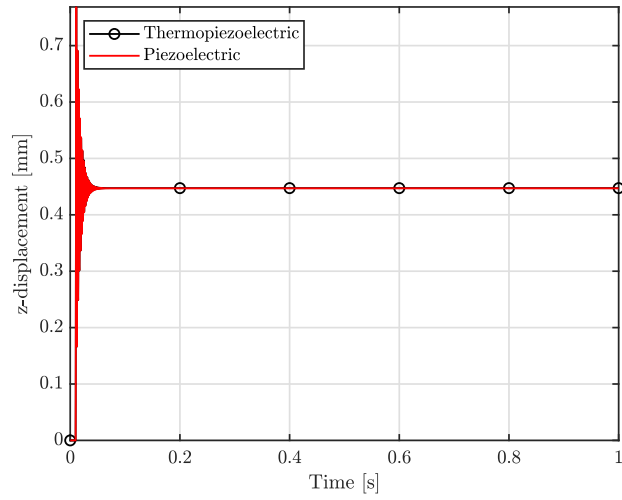
(a) Developed voltage,  $z$ -displacement, and temperature due to a step input



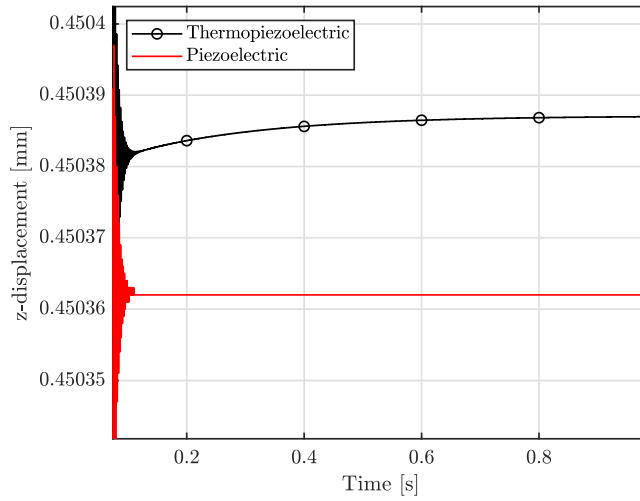
(b) Mesh profile representing the voltage, displacement, and temperature at the step time ( $t = 0.01$  seconds)

Fig. 4.8 Bender actuator due to a step signal

As discussed in Chapter 1, piezoelectric actuators are widely used in precise positioning applications, hence their displacements are of significant importance. Therefore, a comparison of the bimorph actuator position is made by considering both piezoelectric and thermopiezoelectric analyses, where the deflection of the bender is shown in Fig. 4.9. Fig. 4.9(b) provides a magnified view of the  $z$ -displacement. The displacement obtained from the piezoelectric analysis appears as a constant displacement after the oscillations have damped out, which is as expected since the step signal should maintain a constant position after the initial transient phase. In contrast, the thermopiezoelectric analysis, even with a minor temperature increase, reveals a slight upward drift in the actuator's positioning immediately after the oscillations have damped out. This difference of approximately 20 nm between the thermopiezoelectric and piezoelectric simulations indicates the impact of thermal effects, specifically the pyroelectric and electrocaloric effects. By the end of the simulation ( $t = 1$  second), the position difference reaches around 25 nm.



(a)  $z$ -displacement



(b)  $z$ -displacement with zoom in at  $y$  axis

Fig. 4.9 Thermopiezoelectric analysis versus piezoelectric analysis

### 4.2.2 Sinusoidal Input

Another common drive signal for a multimorph bender is a unipolar sinusoidal wave signal (see Fig. 4.10). The simulation is conducted for a duration of 1 second.

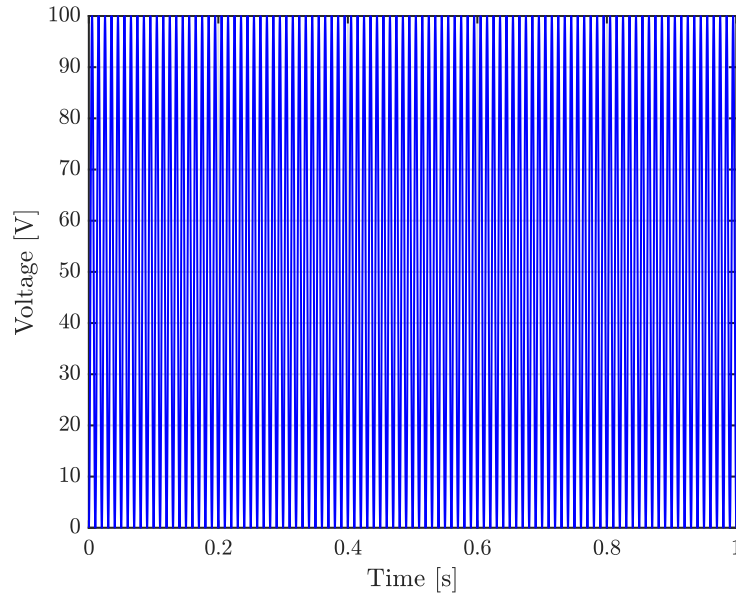
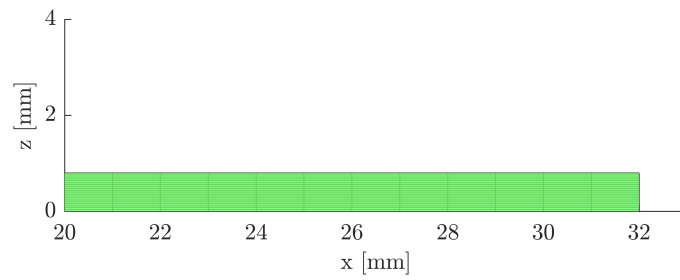


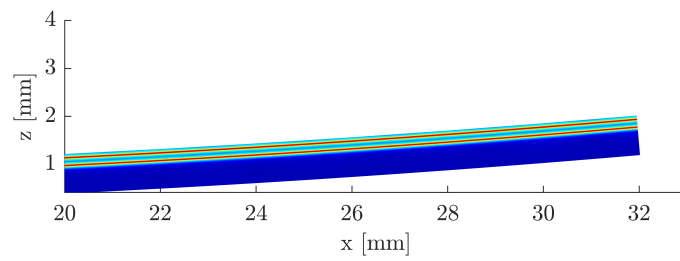
Fig. 4.10 Unipolar sinusoidal wave signal

The top surface of the actuator is subjected to a unipolar sinusoidal waveform signal ( $\phi = \frac{\phi_0}{2}(\sin(2\pi t f - \pi/2) + 1)$ ), with a voltage of 150 V applied to the surfaces corresponding to the positive terminal (red wires) and 0 V applied to the other surfaces, with an operating frequency of 100 Hz (refer to Table 4.3). The bottom surface is constrained to 0°C. The first simulation considers all thermal effects, including the pyroelectric and electrocaloric effects.

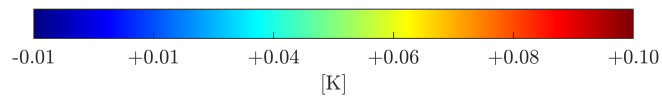
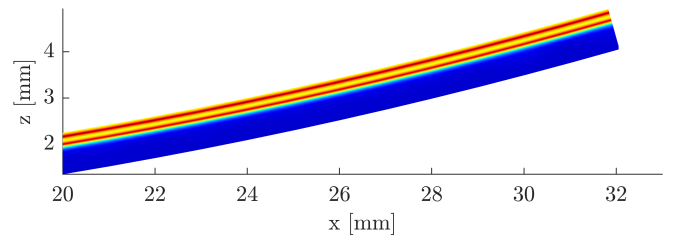
Fig. 4.11 shows the evolution of the developed temperature over time when the pyroelectric effect is considered. Initially, at the first time step, the bender actuator is at rest, as shown in Fig. 4.11(a). It then reaches its maximum developed temperature at  $t = 0.0040$  seconds (see Fig. 4.11(c)). With this quite small temperature of 0.1 K, again the mesh exhibits more intense red regions, which correspond to the areas where voltage is being applied.



(a) time  $t = 0$  seconds



(b) time  $t = 0.0018$  seconds

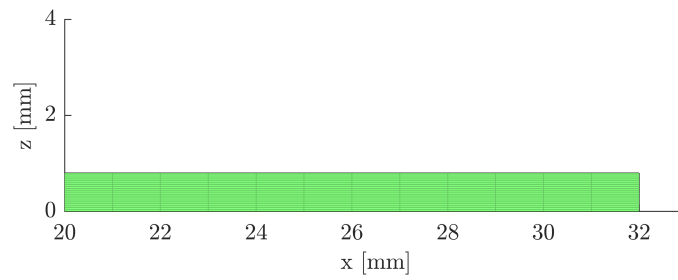


(c) time  $t = 0.0040$  seconds

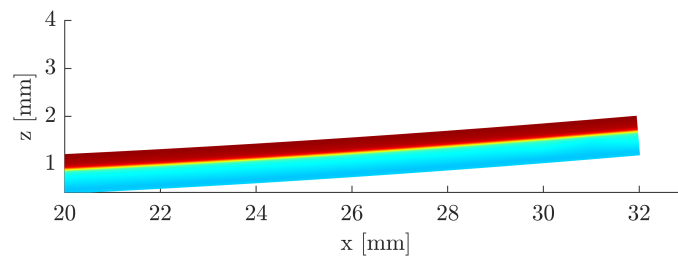
Fig. 4.11 Developed temperature at different times considering the pyroelectric effect

The second simulation takes into account thermal effects but neglects the pyroelectric coefficient. Fig. 4.12 shows the developed temperature when the pyroelectric effect is neglected. At the time  $t = 0$ , the actuator is at rest and it reaches a maximum temperature of 0.02 K, which is due to the heat of deformation only, at time  $t = 0.0040$  seconds (see Fig. 4.12(c)). In Fig. 4.12(c), the temperature gradually increases, without alternating temperature in the layers as seen in the case where the pyroelectric coefficient is considered.

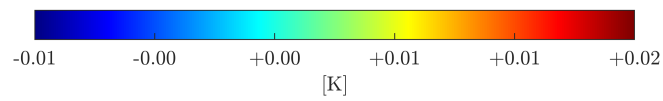
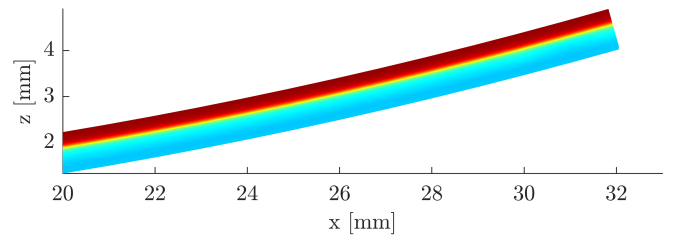
Both investigated simulations did not result in a significantly elevated temperature. However, when accounting for the pyroelectric effect, the maximum reached temperature is five times higher than when the pyroelectric effect is neglected. Consequently, a larger displacement is typically expected when the pyroelectric is taken into account. The simulation considering the pyroelectric effect resulted in a maximum displacement of 412.7  $\mu\text{m}$  at  $t = 0.0040$  seconds, while the simulation neglecting the pyroelectric effect achieved a maximum deflection of 410.1  $\mu\text{m}$  at the same time. The difference in their maximum displacement is approximately 2.6  $\mu\text{m}$ , a significant variance with potential implications for positioning applications.



(a) time  $t = 0$  seconds



(b) time  $t = 0.0018$  seconds



(c) time  $t = 0.0040$  seconds

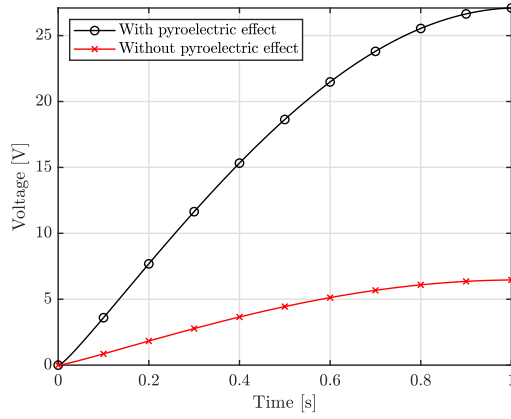
Fig. 4.12 Developed temperature at different times neglecting the pyroelectric effect

### 4.2.3 Thermal Load

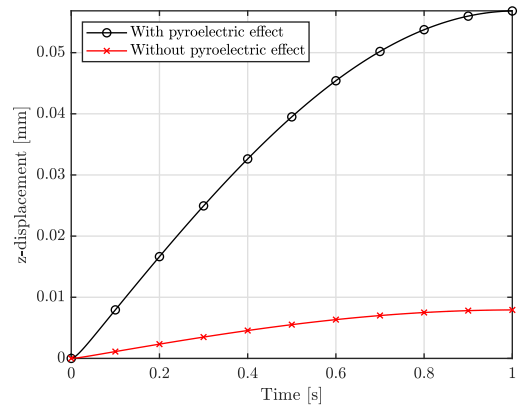
This section investigates how a thermal load impacts the voltage and deflection of the bender actuator by comparing simulations that consider the pyroelectric effect with simulations that neglect it. For this purpose, the first analysis sets the pyroelectric coefficient  $p_3$  to its correspondent values  $-6 \times 10^{-4}$ , while in the second analysis, the pyroelectric matrix becomes all zero. Thermal effects such as thermal expansion and the thermal conductivity are still considered in the simulation. The top surface of the actuator is subjected to a sudden sinusoidal temperature rise  $\theta = \theta_0 \sin(\frac{\pi}{2}t)$  with a magnitude of 50 K. The bottom surface is set to a constant temperature of 273 K. Boundary conditions are enforced to 0 V on the surfaces corresponding to drive signal (white wires), while voltage could occur on the other surfaces.

Fig. 4.13 shows the developed voltage and deflection of the actuator under the thermal load for simulations considering and neglecting the pyroelectric effect. Both voltage and displacement results, as shown in Fig. 4.13(a) and Fig. 4.13(b), reveal larger values are obtained in the simulation that considers the pyroelectric effect. The voltage exhibits a difference of approximately 21 V in magnitude, while the displacement shows a difference of around 45  $\mu\text{m}$ . These significant differences underscore the importance of accounting for the pyroelectric effect in certain ap-

plications where thermal effects are expected to be significant.



(a) Developed voltage



(b) Developed displacement

Fig. 4.13 Bender actuator under thermal load considering the pyroelectric effect versus without the pyroelectric effect

## 5 Temperature Dependence of the Piezoelectric Strain Coefficients

Numerous studies have investigated the temperature dependence of piezoelectric strain coefficients in piezoelectric actuators. This temperature dependence affects the piezoelectric strain coefficients  $d_{31}$  and  $d_{33}$  in soft PZT 5A and PZT 5H ceramics, which are often used in nan positioning applications demanding high sensitivity [16]. For bender actuators, the transverse strain coefficient  $d_{31}$  is more influential, while for stack actuators, the longitudinal strain coefficient  $d_{33}$  naturally plays a larger role. The objective is to investigate how the actuator behaves when temperature-dependent piezoelectric strain coefficients are considered in the simulations, bringing it closer to the realistic behavior of the actuator.

Up to this point, this thesis has considered all coefficients to be temperature independent. However, for a more precise characterization of an actuator behavior, the relationship between the temperature and the piezoelectric strain coefficients  $d_{31}$  and  $d_{33}$  must be taken into account into each time iteration of a transient anal-

ysis. For this purpose, the developed code is enhanced with the implementation of temperature-dependent coefficients  $d_{31}$  and  $d_{33}$ . The algorithm implemented recomputes the piezoelectric strain coefficients  $d_{31}$  or  $d_{33}$  at each time step after finding the average temperature for each element. Consequently, the new piezoelectric strain coefficient ratios multiply the element piezoelectric stiffness matrix  $k_{up}^e$ , and, as a result, the global stiffness matrix  $K$  is updated at each time step. This process is repeated until the last time step of the simulation, at which point the displacements, electric potential, and temperature are generated. Table 5.1 presents the implementation to consider varying coefficients for both  $d_{31}$  and  $d_{33}$ .

1. Assemble the global stiffness matrix  $K$ , global mass matrix  $M$ , and damping matrix  $D$
2. Enforce homogeneous and non-homogeneous boundary conditions
3. Set the Newmark parameters  $\beta$  and  $\gamma$ , initial and final time ( $t_i$  and  $t_f$ ), and time step  $\Delta t$
4. Set initial conditions for the displacement, electric potential, temperature, and their relevant derivatives
5. Start loop from initial to final time with time step  $\Delta t$ 
  - 5.1 Call the global stiffness matrix and compute the dynamic global stiffness matrix  $\hat{K}$  (Eq. (2.83))
  - 5.2 Compute the effective global force vector  $\hat{F}$  (Eq. (2.84))
  - 5.3 Compute the displacements, electric potential, temperature (Eq. (2.82)), and their relevant derivatives (Eq. (2.81)–(Eq. (2.80))) for current time step
  - 5.4 Loop over the temperature number of elements at current time step:
    - 5.4.1 Compute the nodal temperatures at current time step, and find the average temperature for each element
    - 5.4.2 Compute the new piezoelectric strain coefficient  $d_{31}$  or  $d_{33}$  using the average temperature of each element
  - 5.5 Multiply the computed  $d_{31}$  or  $d_{33}$  by the piezoelectric element stiffness matrix  $k_{up}^e$  and update the global stiffness matrix  $K$
  - 5.6 Repeat step number 5 until  $t_f$
6. Output the final displacements, voltages, and temperatures

Table 5.1 Newmark integration steps for consideration of the dependence of the piezoelectric strain coefficient  $d_{31}$  and  $d_{33}$  on temperature

## 5.1 Stack Actuators with Varying Piezoelectric Strain Coefficients Matrix

This section investigates the temperature dependence of the piezoelectric strain coefficient  $d_{33}$  in stack actuators. The behavior of the coefficient  $d_{33}$  for various loading conditions of PZT 5A (*PI Ceramics* P-887.51 stack actuator) is shown in Fig. 5.1, demonstrating its linear dependence on the temperature up to 100 °C. For the stack actuator, this thesis works with the coefficients correspondent to PZT 5A, where the coefficient  $d_{33}$  is taken to have a value of approximately  $400 \times 10^{-12}$  m/V at a temperature of  $\theta = 20^\circ\text{C}$ . To establish a more accurate relation for the actual  $d_{33}$  value ( $400 \times 10^{-12}$  m/V), a linear equation  $d_{33}(\theta) = m\theta + b$  is assumed, with the slope  $m$  derived from the black curve in Fig. 5.1. Consequently, the relationship between the piezoelectric strain coefficient  $d_{33}$  and temperature for PZT 5A can be expressed as  $d_{33} = 2.615 \times 10^{-12}\theta + 3.447 \times 10^{-10}$ , yielding the graph shown in Fig. 5.2.

For this purpose, three simulations are compared: a piezoelectric simulation, a thermopiezoelectric simulation that assumes the piezoelectric strain coefficients to be constant, and a thermopiezoelectric simulation that considers the dependence of the coefficient  $d_{33}$  on temperature. The investigated stack actuator is simplified to a 7-layer model due to the computational time required to recompute (numerically

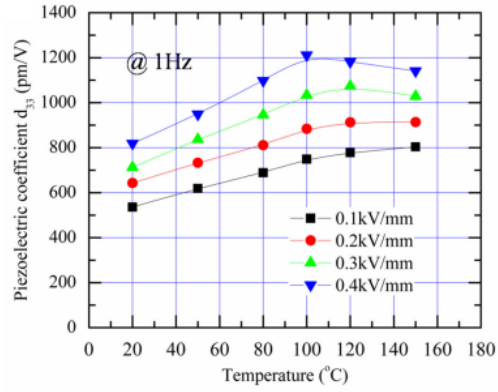


Fig. 5.1 Evolution of the piezoelectric coefficient  $d_{33}$  as a function of temperature for soft PZT type. (Source:[16])

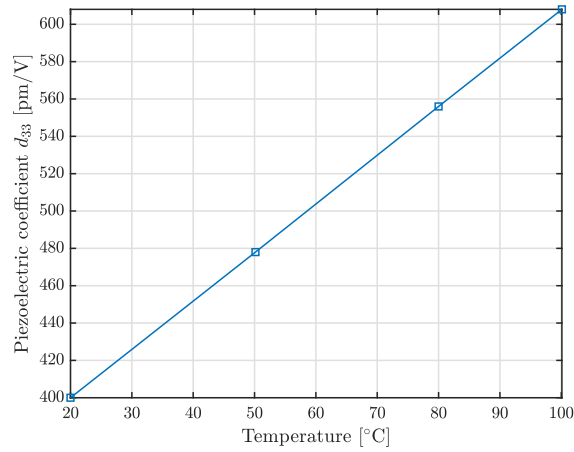


Fig. 5.2 Evolution of the piezoelectric coefficient  $d_{33}$  as a function of temperature for PZT 5A ceramic

integrate) the global stiffness matrix  $K$  at each time step in a 375-layer model.

### 5.1.1 Step Input

A step input with a voltage of 500 V is applied to alternating surfaces of the stack actuator following the diagram demonstrated in Fig. 3.6, with the bottom surface of the actuator held at a constant temperature of 273.15 K. The simulation results are presented in Fig. 5.3, where the simulation considering the temperature-dependent coefficient  $d_{33}$  shows a larger developed displacement of approximately 3 nm compared to the piezoelectric simulation, and a larger displacement of approximately 13 nm compared to the thermopiezoelectric simulation with constant piezoelectric strain coefficients. This behavior is expected since the temperature dependence of the coefficient  $d_{33}$  linearly increases, meaning that the change in temperature causes the piezoelectric coefficient to become larger. The piezoelectric simulation produces a larger displacement than the thermopiezoelectric simulation with a constant  $d_{33}$  coefficient, a difference of approximately 10 nm. This outcome is due to the temperature applied to the top surface of the actuator and the negative  $\alpha_3$  coefficient, which causes the actuator to contract. As a result, this contraction leads to a slightly smaller displacement in the thermopiezoelectric simulation (with constant coefficient  $d_{33}$ ).

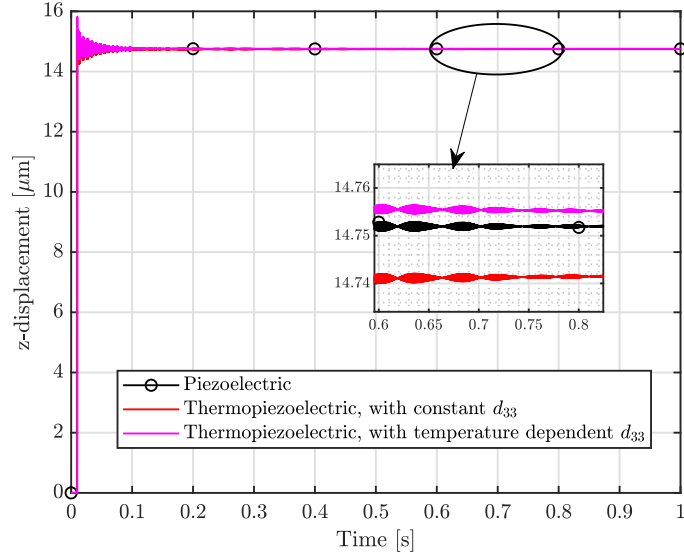


Fig. 5.3 Time versus developed  $z$ -displacement

## 5.2 Bender Actuators with Varying Piezoelectric Strain Coefficients Matrix

The relation between the temperature and the coefficient  $d_{31}$  for PZT 5H, the material of the *ThorLabs* PB4NB2W bender actuator, is demonstrated in Fig. 5.4. For the bender actuator, this thesis works with the coefficients correspondent to PZT 5H, where the coefficient  $d_{31}$  is taken to have a value of approximately  $-320 \times 10^{-12}$  m/V at a temperature of  $\theta = 20^\circ\text{C}$ . This relation can be represented by the linear equation  $d_{31}(\theta) = m\theta + b$ . The ratio of the recomputed  $d_{31}$  is required to update the piezoelectric stiffness matrix  $k_{u\phi}^e$ , and thus, the relationship can be expressed as  $d_{31}(\theta) = 0.003567(\theta) - 0.06189$ .

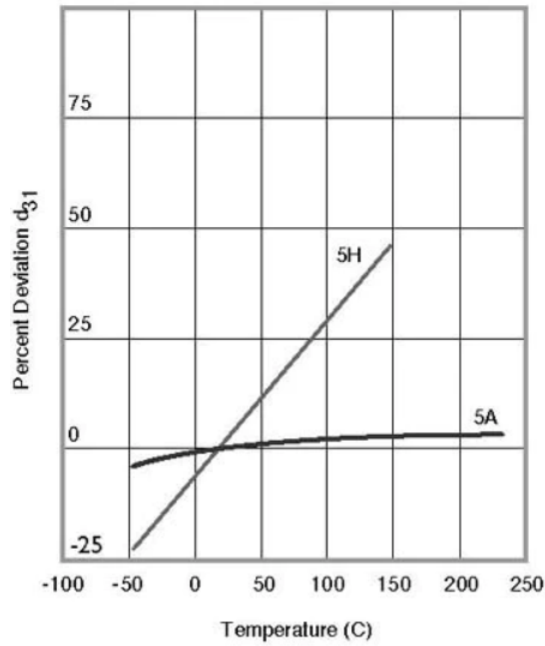


Fig. 5.4 Evolution of the piezoelectric coefficient  $d_{31}$  as a function of temperature for PZT type. (Source: [1])

This section investigates the temperature-dependent behavior of the piezoelectric strain coefficients in two different scenarios. The first case involves an applied voltage step, while the second case focuses on an applied thermal load. Since the transverse strain coefficient  $d_{31}$  exerts a more significant influence on bender actuators, the relationship demonstrated in Fig. 5.4 is used to conduct the simulations.

### 5.2.1 Step Input

This simulation is similar to the one considered in Section 4.2.1. In this case, a step input is applied to the actuator by setting the driving voltage to 150 V on the drive signal surfaces (white wires), while the other surfaces are set to 0 V, causing the actuator to bend upwards (see Table 4.1). The bender is fixed at its left end (see Fig. 4.4). This scenario allows for a direct comparison among three simulations: a piezoelectric simulation, a thermopiezoelectric simulation with a constant piezoelectric strain coefficient  $d_{31}$ , and a thermopiezoelectric simulation with a temperature-dependent  $d_{31}$ . Additionally, the simulation involving the varying  $d_{31}$  coefficient explores two distinct scenarios: one with the reference temperature  $\Theta$  set to 273.15 K and the other with  $\Theta$  set to 293.15 K.

The developed displacement in  $z$  is demonstrated in Fig. 5.5 for all cases. The simulation considering the temperature-dependent  $d_{31}$  demonstrates a larger displacement compared to both piezoelectric and thermopiezoelectric with a constant  $d_{31}$  simulations. This behavior arises from the fact that, as temperature increases, the piezoelectric strain coefficient  $d_{31}$  also increases, leading to larger displacements. The difference in displacement between the simulations with the temperature-dependent coefficient  $d_{31}$  and constant coefficient  $d_{31}$  amounts to approximately 4.225  $\mu\text{m}$ , while the difference between the temperature-dependent coefficient  $d_{31}$

and the piezoelectric simulations are approximately 4.249  $\mu\text{m}$ .

Furthermore, the difference between the simulations that account for the varying  $d_{31}$  under different reference temperatures  $\Theta$  falls within the nanometer range, around 1 nm. This difference is minimal in comparison to the overall displacement, highlighting the sensitivity of the actuator’s response to temperature-dependent variations in the piezoelectric strain coefficient.

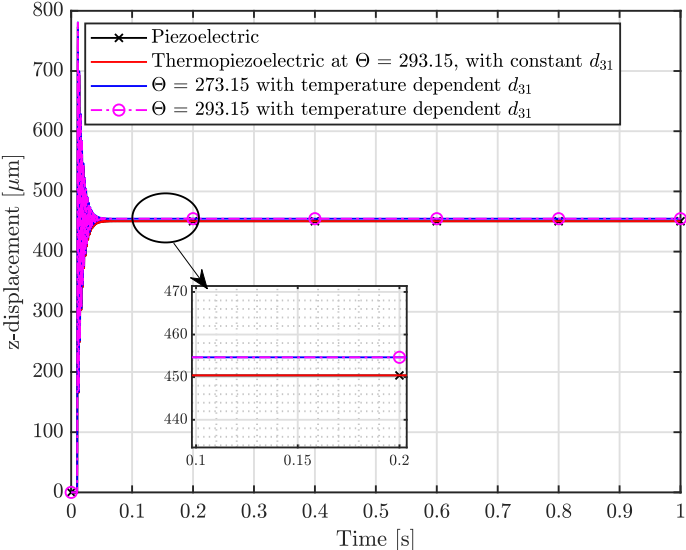


Fig. 5.5 Time versus developed  $z$ -displacement for a voltage step

### 5.2.2 Thermal Load

The bender actuator is subjected to a dynamic thermal load applied to the top surface of the actuator, while the bottom surface is maintained at a constant

temperature of 273.15 K. Boundary conditions enforce 0 V on the surfaces corresponding to the variable voltage of the actuator (white wire), while arbitrary distributions can occur on the other surfaces. The dynamic load is represented as a sinusoidal wave  $\theta = \theta_0 \sin\left(\frac{\pi}{2}t\right)$ , where  $\theta_0$  equals 15 K. The objective is to investigate the resulting displacement caused by the thermal load in two simulations: the first assumes the piezoelectric strain coefficient  $d_{31}$  to be constant, and the second considers the piezoelectric strain coefficient  $d_{31}$  dependent on temperature. The deflection of the bender actuator is shown in Fig. 5.6. The simulation where the coefficient  $d_{31}$  is temperature-dependent demonstrates a larger  $z$ -displacement than the simulation where the coefficient  $d_{31}$  is constant. Specifically, the difference between these simulations is approximately 93.8 nm.

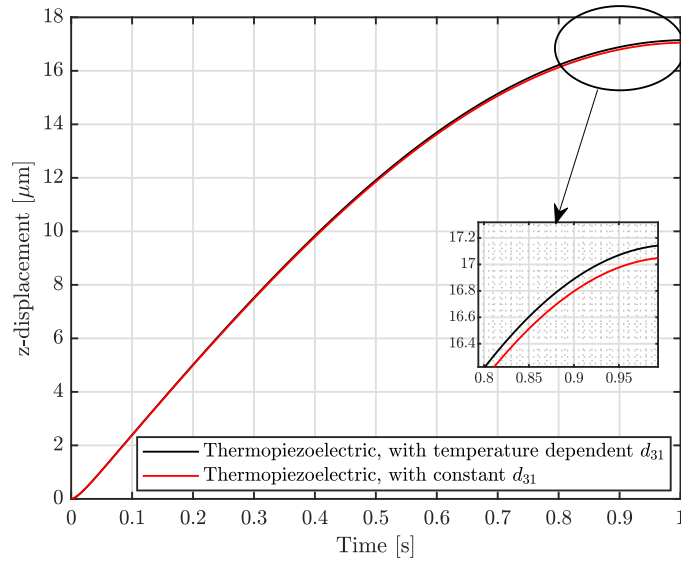


Fig. 5.6 Displacement in  $z$  caused by a dynamic thermal load

### 5.3 Case Study: A Stratospheric Balloon Flight

In this section, a realistic case study for a piezoelectric bender actuator in use as a lens positioning element on a stratospheric balloon flight is analyzed. The bender actuator is scanned across its positive range with multiple steps with periodic resets to its initial position, from the time  $t = 0.4$  seconds to  $t = 2$  seconds, ranging from 0 V to 150 V. Additionally, the ambient temperature is varied to simulate the worst-case scenario that could be expected to occur for the flight with temperatures considered between  $-20^{\circ}\text{C}$  and  $40^{\circ}\text{C}$ . Fig. 5.7 shows the step input signal, and the variation in the ambient temperature  $\Theta_{\infty}$  for the simulation during 2 seconds. The temperature variation is considered in the finite element

code by incorporating convection, with the initial body temperature set at 293.15 K. In order to conduct the simulation in a reasonable amount of time, the coefficient of convection is artificially increased such that only 2 seconds need to be considered. Four cases are considered, including piezoelectric simulation, thermopiezoelectric with temperature-independent coefficient  $d_{31}$ , thermopiezoelectric with temperature-independent coefficient  $d_{31}$  while neglecting the pyroelectric and electrocaloric effects, and thermopiezoelectric with temperature-dependent coefficient  $d_{31}$ .

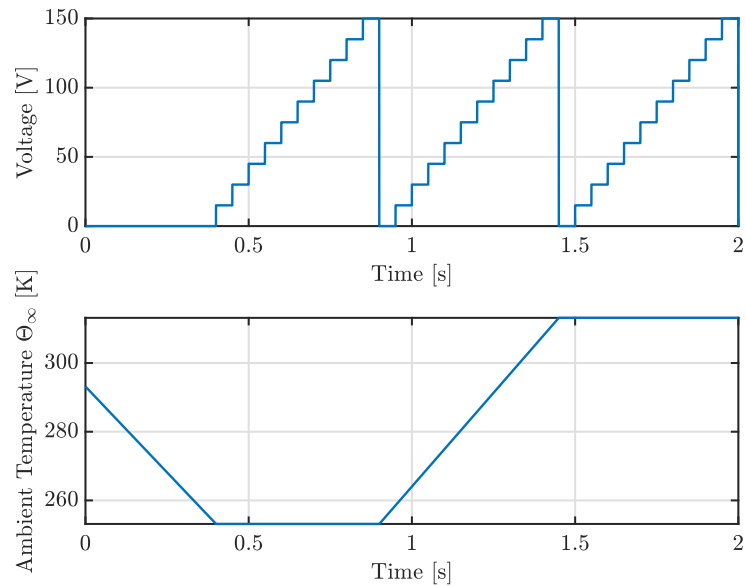


Fig. 5.7 Step input that scans across the bimorph range and the ambient temperature variation that occurs during the simulation

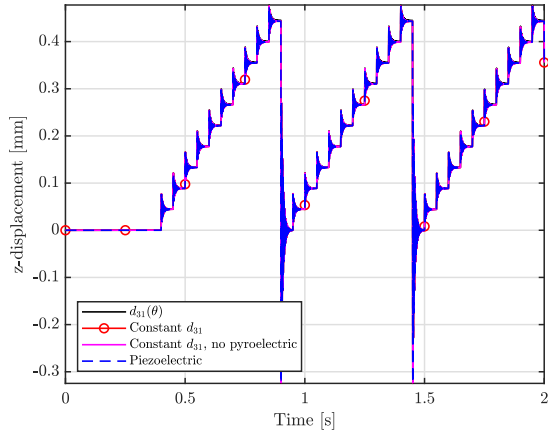
The displacement and the developed temperature of the bender actuator are

presented in Fig. 5.8. The  $z$ -displacement is depicted in Fig. 5.8(a), and the developed temperature is presented in Fig. 5.8(b), for all four cases. Fig. 5.9 focuses on the important results, where Fig. 5.9(a) depicts the part that corresponds to convection only (0 to 0.4 seconds), Fig. 5.9(b) shows the displacement at 0.9 seconds (150 V), and Fig. 5.9(c) depicts the displacement of the bender actuator from the time  $t = 0.9$  seconds to  $t = 2$  seconds. In Fig. 5.9(a), the temperature-dependent simulation ( $d_{31}(\theta)$  in the graph) demonstrates a considerable difference as compared to the two other thermopiezoelectric simulations (the piezoelectric case does not account for convection) with the largest difference compared to the thermopiezoelectric simulation with temperature-independent  $d_{31}$  that neglects the pyroelectric and electrocaloric effects (constant  $d_{31}$ , no pyroelectric in the graph) being approximately 1.04 nm.

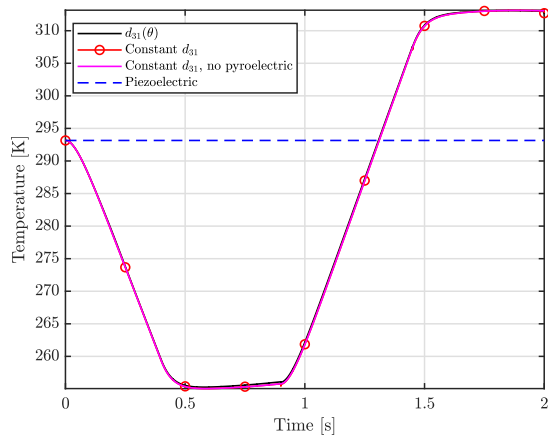
The displacement at time  $t = 0.9$  seconds is presented in Fig. 5.9(b). The difference between the thermopiezoelectric simulation  $d_{31}(\theta)$  and the other simulations increases as the step input signal increases, reaching a difference of approximately 2  $\mu\text{m}$  at 0.9 seconds (150 V) when compared to the piezoelectric simulation, and 1.7  $\mu\text{m}$  when compared to both thermopiezoelectric simulations that consider a constant coefficient  $d_{31}$ .

Fig. 5.9(c) shows the results from time  $t = 0.9$  seconds to  $t = 2$  seconds. In this specific part of the simulation, the ambient temperature increases from 253.15 K to

313.15 K and then remains constant for the remaining duration of the simulation. From Fig. 5.9(c), it is observed that the thermopiezoelectric with a temperature-dependent  $d_{31}$  experiences an upward drift when compared to the three other simulations. The difference is approximately 1.6  $\mu\text{m}$  when compared to the piezoelectric simulation and 1.7  $\mu\text{m}$  when compared to the other two thermopiezoelectric simulations.

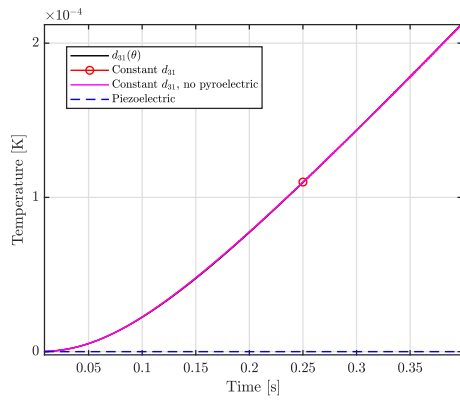


(a) Displacement in  $z$

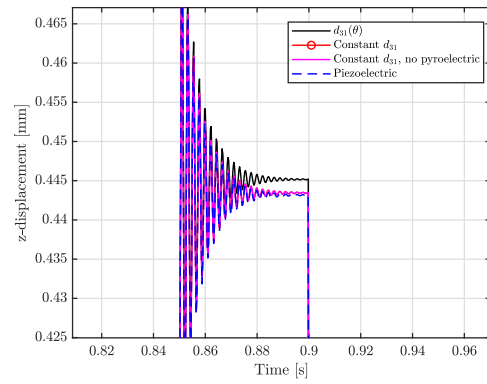


(b) Developed temperature

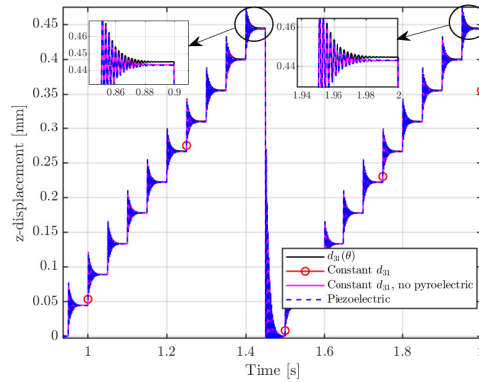
Fig. 5.8 Multimorph bender actuator performance with changing ambient conditions while scanning across the full range



(a) Displacement from 0 to 0.4 seconds



(b) Displacement at 0.9 seconds



(c) Displacement from 0.9 to 2 seconds

Fig. 5.9 Displacement of the bender actuator due to step input signals and temperature variations

## 6 Conclusions and Future Work

In this study, a finite element code was developed in MATLAB to numerically solve the fully-coupled field equations of thermopiezoelectricity in order to investigate the effects of both pyroelectric and electrocaloric effects on piezoelectric actuators, in particular stack and bender actuators. The verification process in Chapter 2 showed an excellent agreement between the implemented finite element code and the commercial FE software ABAQUS for various types of elements, including three-dimensional solid, piezoelectric, and thermoelastic elements. In addition, the developed code was verified against the results of Gornandt and Gabbert [4] confirming the implementation of the finite element code in MATLAB for thermopiezoelectric simulations.

Chapters 3 and 4 focused on the investigation of multilayer stack and multimorph bender actuators, respectively. The primary goal was to explore the behavior of these actuators, in particular under dynamic loading. For stack actuators, the response to an applied voltage step input was analyzed for models with 1, 7,

and 375 layers. In the thermopiezoelectric simulations, it was observed that the  $z$ -displacement exhibited a gradual increase over time due to the pyroelectric effect. In contrast, the piezoelectric simulations showed a constant  $z$ -displacement after the decay of the initial transient response, resulting in a difference of approximately 10 nm. The simulation results with different numbers of layers yielded excellent performance in terms of mechanical displacement. However, the thermal field varied among models with different numbers of layers. This discrepancy arose from the fact that the voltage scaling only accounted for the mechanical and electrical fields, consequently, the generated temperatures were unrealistic for the 1-layer and 7-layer models. This temperature variation was verified by introducing a realistic model with 375 layers. In this case, the temperature generated by a step input was approximately 0.62 K, in contrast to the substantial spikes seen in the 1-layer and 7-layer models. A thermal dynamic load was investigated for the realistic 375-layer model. This analysis involved subjecting the stack to a temperature rise, and the resulting voltage and displacement were studied for simulations that considered the pyroelectric effect and those that neglected it. The findings revealed that the pyroelectric effect exerted a significant influence on the developed displacement (approximately twice as large in simulations accounting for the pyroelectric effect) and on the voltage (approximately 12.5 times larger in simulations accounting for the pyroelectric effect) (refer to Fig. 3.14). These discrepancies are significant and

emphasize the importance of considering the pyroelectric effect in nanopositioning applications.

Multimorph bender actuators were investigated in Chapter 4, with a realistic 10-layer model subjected to various dynamic loads. The investigation analyzed an applied step input for both piezoelectric and thermopiezoelectric simulations. The thermopiezoelectric simulation resulted in a  $z$ -displacement that was approximately 25 nm larger than that obtained in the piezoelectric simulation. Similar to the multilayer stack actuator, the thermopiezoelectric simulation exhibited a gradual drift in the  $z$ -displacement over time, while the piezoelectric simulation maintained a constant displacement. Furthermore, the analysis explored the  $z$ -displacement and temperature developed due to a sinusoidal wave input with a frequency of 100 Hz. In one simulation, the pyroelectric effect was neglected to investigate potential differences in the resulting  $z$ -displacement and temperature. While the temperatures generated in both simulations (considering and neglecting the pyroelectric effect) were quite small, the simulation considering the pyroelectric effect produced temperatures approximately five times larger than the simulation that neglected it. Since displacement is expected to be larger under a larger thermal field, a difference of 2.6  $\mu\text{m}$  was observed in the displacement between the two simulations. Another analysis was carried out for an applied dynamic thermal load. The multimorph bender actuator was subjected to a temperature increase, and in this scenario, the

voltage and  $z$ -displacement were examined for simulations that considered and neglected the pyroelectric effect. Substantial differences were noted, with a voltage difference of 21 V and a difference generated of 45  $\mu\text{m}$  in the displacement (refer to Fig. 4.13).

The temperature-dependent piezoelectric strain coefficients  $d_{31}$  and  $d_{33}$  were investigated in Chapter 5. For multilayer stack actuators, a simplified 7-layer model was used to conduct the study since the realistic model required an impractical computational time. An applied step input was investigated for three models: piezoelectric, thermopiezoelectric with constant  $d_{33}$ , and thermopiezoelectric with temperature dependent  $d_{33}$ . As expected, the model with a temperature-dependent coefficient yielded a larger displacement than the other simulations due the fact that the piezoelectric strain coefficient increases with the produced temperature. This difference was of approximately 13 nm when compared to the thermopiezoelectric simulation with constant coefficient  $d_{33}$ . The multimorph bender actuators, the relationship between the coefficient  $d_{31}$  and temperature exhibited a more pronounced effect. Consequently, differences in the developed displacement were expected to be larger as compared to stack actuators. This statement was verified through the analysis of an voltage step. The comparison between simulations accounting for the temperature-dependent  $d_{31}$  and those using constant piezoelectric coefficients demonstrated a significant variation with an approximate difference of 4.2  $\mu\text{m}$  in

the  $z$ -displacement. Additionally, two scenarios were examined in the thermopiezoelectric simulations with temperature-dependent  $d_{31}$  coefficients: one that set the reference temperature  $\Theta_\infty$  to room temperature (293.15 K) and the other with  $\Theta_\infty$  at 273.15 K. The differences in displacement between these two scenarios were minimal (in the nanometer range) compared to the overall variations among all simulations.

Moreover, a dynamic thermal load was explored for both simulations considering a constant  $d_{31}$  and a temperature-dependent  $d_{31}$ . The observed difference amounted to 93.8 nm (see Fig. 5.6), with the temperature-dependent simulation yielding a larger  $z$ -displacement compared to the constant  $d_{31}$  simulation.

Lastly, a realistic scenario of a stratospheric balloon flight where a piezoelectric bimorph actuator is used as a positioning element for a lens is considered was analyzed. Four simulations were conducted, including a piezoelectric simulation, and three thermopiezoelectric simulations: one with a constant  $d_{31}$  coefficient, another with a constant  $d_{31}$  coefficient while neglecting the pyroelectric and electrocaloric effects, and finally a simulation that considers a temperature-dependent coefficient  $d_{31}$ . Significant differences were observed among the simulations, with an approximate difference of 1.7  $\mu\text{m}$  between the thermopiezoelectric with temperature-dependent  $d_{31}$  simulation and the two other thermopiezoelectric simulations (constant  $d_{31}$ ), and 2  $\mu\text{m}$  between the thermopiezoelectric with temperature-dependent

$d_{31}$  simulation and the piezoelectric simulation. This is significant when considering that the step height is 45  $\mu\text{m}$ , hence a 2  $\mu\text{m}$  difference is quite considerable. These simulations and the realistic case presented in Chapter 5 emphasize the importance of accounting for temperature-dependent coefficients when investigating and designing applications involving piezoelectric stack and bender actuators.

## 6.1 Future Work

This study involved simulations using models with opposite polarization directions. The polarization direction was assumed to be ideally aligned at  $0^\circ$  or  $180^\circ$ . However, in real-world scenarios, the polarization direction is typically not perfectly aligned and tends to cluster within domains. To more accurately capture the behavior of piezoelectric actuators, it is possible to implement a Gaussian distribution for the polarization direction. This approach introduces small angle deviations in the simulations to better represent the practical variation in the initial polarization direction.

Furthermore, the two most commonly seen nonlinearities associated with piezoelectric actuators, hysteresis and creep, are not present in the developed finite element code. The code could be improved by implementing the hysteresis characteristics of piezoelectric materials. By incorporating this hysteresis into the code, the simulations could more accurately replicate the complex relationship between

electrical and mechanical properties exhibited by piezoelectric materials. This addition would also impact how the temperature changes in response to varying voltage inputs over time. By doing so, the simulations could more accurately replicate the actual behavior of the analyzed actuator.

Dealing with coefficients in piezoelectric and thermopiezoelectric analyses can be extremely complex due to the intricate relationship of mechanical, electrical, and thermal fields. Chapter 5 investigated the temperature dependence of the piezoelectric strain coefficients. However, it is important to note that piezoelectric strain coefficients are not the only coefficients affected by temperature. Coefficients such as the dielectric coefficients  $\varepsilon$  and the compliance  $s_{11}^E$  also exhibit temperature dependence, for instance, and the piezoelectric strain coefficient  $d$  also increases with electric field strength. One improvement to consider is the incorporation of these temperature-dependent coefficients (dielectric and compliance) into the code. This development would enable more accurate predictions of the actual behavior of these piezoelectric actuators through simulations and would also open the door to designing better piezoelectric actuators that can perform effectively in environments where thermal fields play an important role.

## A Appendix A

External mechanical element force vector	$f_{uu}^e = \int_{V^e} N_u^T \rho b dV^e + \int_{O_t^e} N_u^T \bar{t} dO^e \quad (\text{A.1})$
Electric element charge vector	$f_{\phi\phi}^e = - \int_{O_Q^e} N_\phi^T \bar{Q} dO^e \quad (\text{A.2})$
External thermal element force vector	$f_{\theta\theta}^e = \int_{O_{qh}^e} N_\theta^T h_v (\Theta_\infty - \Theta_0) dO^e + \int_{O_{qs}^e} N_\theta^T \bar{q}_s dO^e + \int_{V^e} \rho r dV^e \quad (\text{A.3})$

Table A.1 External force equations for thermopiezoelectric finite element formulation

Mechanical element stiffness matrix	$k_{uu}^e = \int_{V^e} B_u^T C B_u dV^e \quad (\text{A.4})$
Direct piezoelectric element stiffness matrix	$k_{u\phi}^e = \int_{V^e} B_u^T e^T B_\phi dV^e \quad (\text{A.5})$
Elasto-thermal element stiffness matrix	$k_{u\theta}^e = \int_{V^e} B_u^T \zeta N_\theta dV^e \quad (\text{A.6})$
Dielectric element stiffness matrix	$k_{\phi\phi}^e = \int_{V^e} B_\phi^T \varepsilon B_\phi dV^e \quad (\text{A.7})$
Pyroelectric coupling element stiffness matrix	$k_{\phi\theta}^e = \int_{V^e} B_\phi^T p N_\theta dV^e \quad (\text{A.8})$
Thermal element stiffness matrix	$k_{\theta\theta}^e = \int_{V^e} B_\theta^T \lambda B_\theta dV^e + \int_{O_{qh}^e} N_\theta^T h_v N_\theta dO^e \quad (\text{A.9})$

Table A.2 Thermopiezoelectric finite element equations of stationary terms

Element mass matrix	$M_{uu}^e = \int_{V^e} \rho N_u^T N_u dV^e \quad (\text{A.10})$
Thermoelastic element stiffness matrix	$k_{\theta u}^e = \int_{V^e} N_\theta^T N_\theta \Theta \zeta^T B_u dV^e \quad (\text{A.11})$
Electrocaloric element stiffness matrix	$k_{\theta \phi}^e = \int_{V^e} N_\theta^T N_\theta \Theta p^T dV^e \quad (\text{A.12})$
Heat capacity element stiffness matrix	$H_{\theta \theta}^e = \int_{V^e} N_\theta^T \rho c_v N_\theta dV^e \quad (\text{A.13})$

Table A.3 Thermopiezoelectric finite element equations of dynamic terms

## Bibliography

- [1] Piezo.com, “Piezo Materials and Properties.” <https://piezo.com/pages/piezo-material>.
- [2] P. Ceramics, “Piezoelectric actuators.” [https://static.picceramic.com/fileadmin/user\\_upload/pi\\_ceramic/files/catalog\\_CAT/PI\\_CAT128E\\_R3\\_Piezoelectric\\_Actuator.pdf](https://static.picceramic.com/fileadmin/user_upload/pi_ceramic/files/catalog_CAT/PI_CAT128E_R3_Piezoelectric_Actuator.pdf).
- [3] Abaqus, *ABAQUS/Standard User’s Manual, Version 6.9*. United States: Dassault Systèmes Simulia Corp, 2009.
- [4] A. Görnandt and U. Gabbert, “Finite element analysis of thermopiezoelectric smart structures,” *Acta Mechanica*, vol. 154, no. 1, pp. 129–140, 2002.
- [5] ThorLabs, *Piezoelectric Bimorph, 150 V, ±450 μm Travel*. ThorLabs, 2020.
- [6] E. Carrera, M. Cinefra, E. Zappino, and M. Petrolo, *Finite Element Analysis of Structures Through Unified Formulation*. John Wiley & Sons Ltd, 2014.

- [7] Z. Q. Xie, R. Sevilla, O. Hassan, and K. Morgan, “The generation of arbitrary order curved meshes for 3D finite element analysis,” *Computational Mechanics*, vol. 51, pp. 361–374, 2014.
- [8] H. Shao, H. Wang, and J. Fang, “Piezoelectric energy conversion performance of electrospun nanofibers,” in *Energy Harvesting Properties of Electrospun Nanofibers*, 2053-2563, pp. 4–1 to 4–42, IOP Publishing, 2019.
- [9] S. Ghanim and M. Najim, *Preparation and Physical Properties of Barium Titanate with Some Added Oxides*. PhD thesis, University of Technology - Iraq, 2018.
- [10] R. Ruiz and V. Meruane, “Uncertainties propagation and global sensitivity analysis of the frequency response function of piezoelectric energy harvesters,” *Smart Materials and Structures*, vol. 26, no. 6, pp. 065003–14, 2017.
- [11] D. J. Dean, “Introduction to the Finite Element Method (FEM): Lecture 2 First and Second Order One Dimensional Shape Functions.” [https://www.ccg.msm.cam.ac.uk/system/files/documents/FEMOR\\_Lecture\\_2.pdf](https://www.ccg.msm.cam.ac.uk/system/files/documents/FEMOR_Lecture_2.pdf). University of Cambridge - Department of Materials Science & Metallurgy.
- [12] M. Kurki, J. Jeronen, T. Saksa, and T. Tuovinen, “Strain field theory for viscoelastic continuous high-speed webs with plane stress behavior,” in *ECCO-*

*MAS 2012 - European Congress on Computational Methods in Applied Sciences and Engineering*, 2012.

- [13] MIT, “Twenty node brick element.” [https://web.mit.edu/calculix\\_v2.7/CalculiX/ccx\\_2.7/doc/ccx/node29.html#twentynode](https://web.mit.edu/calculix_v2.7/CalculiX/ccx_2.7/doc/ccx/node29.html#twentynode).
- [14] M. Tanbakuei Kashani, “Effect of forming process on the deformational behaviour of steel pipes,” Master’s thesis, University of Ottawa, Ottawa, Canada, 2017.
- [15] Wikipedia contributors, “Mixed boundary condition — Wikipedia, the free encyclopedia,” 2022. [Online; accessed 24-July-2023].
- [16] Z. Dapeng, J. Qinghui, and L. Yingwei, “The effect of temperature and loading frequency on the converse piezoelectric response of soft PZT ceramics,” *Materials Research Express*, vol. 4, no. 12, pp. 125705–8, 2017.
- [17] K. Uchino, *Advanced Piezoelectric Materials: Science and Technology*. Woodhead Publishing, 1st ed., 2010.
- [18] J. Tichi, *Fundamentals of Piezoelectric Sensorics: Mechanical, Dielectric, and Thermodynamical Properties of Piezoelectric Materials*. Springer, 2010.
- [19] P. Dineva, D. Gross, R. Müller, and T. Rangelov, *Piezoelectric Materials*, pp. 7–32. Springer International Publishing, 2014.

- [20] G. Gautschi, *Piezoelectric Sensorics: Force, Strain, Pressure, Acceleration and Acoustic Emission Sensors, Materials and Amplifiers*. Springer, 2002.
- [21] D. L. Logan, *A First Course in the Finite Element Method*. Thomson, 4th ed., 2016.
- [22] R. F. Mould, “Pierre Curie, 1859-1906.,” *Current Oncology*, vol. 14, no. 2, pp. 74–82, 2007.
- [23] W. P. Mason, “Piezoelectricity, its history and applications,” *The Journal of the Acoustical Society of America*, vol. 70, no. 6, pp. 1561–1566, 1981.
- [24] S. Katzir, *The discovery of the piezoelectric effect*, pp. 15–64. Springer, 2006.
- [25] M. S. Vijaya, *Piezoelectric Materials and Devices*. CRC Press, 1st ed., 2016.
- [26] H. J. Lee, *Finite Element Analysis of Active and Sensory Thermopiezoelectric Composite Materials*. Phd thesis, National Aeronautics and Space Administration, Glenn Research Center, Cleveland, OH United States, 2001.
- [27] M. W. Hooker, “Properties of PZT-Based Piezoelectric Ceramics between 150 and 250 °C,” tech. rep., Langley Research Center, 1998.
- [28] M. Manutchehr Danai, *Dictionary of Gems and Gemology*, p. 770. Berlin, Heidelberg: Springer, 3rd ed., 2009.

- [29] W. G. Cady, “Nature and use of piezoelectricity,” *Electrical Engineering*, vol. 66, no. 8, pp. 758–762, 1947.
- [30] J. Valasek, “Piezo-Electric and Allied Phenomena in Rochelle Salt,” *Phys. Rev.*, vol. 17, pp. 475–481, 1921.
- [31] P. K. Panda and B. Sahoo, “PZT to Lead Free Piezo Ceramics: A Review,” *Ferroelectrics*, vol. 474, no. 1, pp. 128–143, 2015.
- [32] M. Siddiqui, J. J. Mohamed, and Z. A. Ahmad, “Structural, piezoelectric, and dielectric properties of PZT-based ceramics without excess lead oxide,” *Journal of the Australian Ceramic Society*, vol. 56, no. 2, pp. 371–377, 2020.
- [33] G. H. Haertling, “Ferroelectric Ceramics: History and Technology,” *Journal of the American Ceramic Society*, vol. 82, no. 4, pp. 797–818, 1999.
- [34] J. F. Tressler, S. Alkoy, and R. E. Newnham, “Piezoelectric Sensors and Sensor Materials,” *Journal of Electroceramics*, vol. 2, no. 4, pp. 257–272, 1998.
- [35] K. Uchino and S. Takahashi, “Multilayer ceramic actuators,” *Current Opinion in Solid State and Materials Science*, vol. 1, no. 5, pp. 698–705, 1996.
- [36] T. King, M. Preston, B. Murphy, and D. Cannell, “Piezoelectric ceramic actuators: A review of machinery applications,” *Precision Engineering*, vol. 12, no. 3, pp. 131–136, 1990.

- [37] D. Waller, J. Chen, and T. R. Gururaja, “Requirements of piezoelectric materials for medical ultrasound transducers,” *ISAF '96. Proceedings of the Tenth IEEE International Symposium on Applications of Ferroelectrics*, vol. 2, pp. 565–568, 1996.
- [38] K. K. Shung, J. M. Cannata, and Q. F. Zhou, “Piezoelectric materials for high frequency medical imaging applications: A review,” *Journal of Electroceramics*, vol. 19, no. 1, pp. 141–147, 2007.
- [39] O. Rubes, P. Tofel, R. Macku, P. Skarvada, F. Ksica, and Z. Hadas, “Piezoelectric Micro-fiber Composite Structure for Sensing and Energy Harvesting Applications,” in *18th IEEE International Conference on Mechatronics - Mechatronika*, pp. 1–6, 2018.
- [40] R. G. Loewy, “Recent developments in smart structures with aeronautical applications,” *Smart Materials and Structures*, vol. 6, no. 5, pp. R11–R42, 1997.
- [41] H. Boukabache, C. Escriba, and J. Y. Fourniols, “Toward Smart Aerospace Structures: Design of a Piezoelectric Sensor and Its Analog Interface for Flaw Detection,” *Sensors*, vol. 14, no. 11, pp. 20543–20561, 2014.

- [42] M. T. Chorsi, E. J. Curry, H. T. Chorsi, R. Das, J. Baroody, P. K. Purohit, H. Ilies, and T. D. Nguyen, “Piezoelectric Biomaterials for Sensors and Actuators,” *Advanced Materials*, vol. 31, no. 1, pp. 1802084–15, 2019.
- [43] B. T. Reinhardt, A. Suprock, and B. Tittmann, “Testing Piezoelectric Sensors in a Nuclear Reactor Environment,” *AIP Conference Proceedings*, vol. 1806, no. 1, pp. 1–8, 2017.
- [44] T. Itoh and T. Suga, “Development of a force sensor for atomic force microscopy using piezoelectric thin films,” vol. 4, no. 4, pp. 218–224, 1993.
- [45] E. J. Curry, K. Ke, M. T. Chorsi, K. S. Wrobel, A. N. Miller, A. Patel, I. Kim, J. Feng, L. Yue, Q. Wu, C.-L. Kuo, K. W.-H. Lo, C. T. Laurencin, H. Ilies, P. K. Purohit, and T. D. Nguyen, “Biodegradable Piezoelectric Force Sensor,” *Proceedings of the National Academy of Sciences*, vol. 115, no. 5, pp. 909–914, 2018.
- [46] A. B. Joshi, A. E. Kalange, D. Bodas, and S. Gangal, “Simulations of piezoelectric pressure sensor for radial artery pulse measurement,” *Materials Science and Engineering: B*, vol. 168, no. 1, pp. 250–253, 2010.
- [47] N.-I. Kim, Y.-L. Chang, J. Chen, T. Barbee, W. Wang, J.-Y. Kim, M.-K. Kwon, S. Shervin, M. Moradnia, S. Pouladi, D. Khatiwada, V. Selvamanickam,

- and J.-H. Ryou, “Piezoelectric pressure sensor based on flexible gallium nitride thin film for harsh-environment and high-temperature applications,” *Sensors and Actuators A: Physical*, vol. 305, pp. 1–9, 2020.
- [48] J. Willis and B. Jimerson, “A piezoelectric accelerometer,” *Proceedings of the IEEE*, vol. 52, no. 7, pp. 871–872, 1964.
- [49] S. Tadigadapa and K. Mateti, “Piezoelectric MEMS sensors: state-of-the-art and perspectives,” *Measurement Science and Technology*, vol. 20, no. 9, pp. 1–30, 2009.
- [50] Y. Zheng, X. Tu, J. Chen, P. Gao, and E. Shi, “Piezoelectric acceleration sensors based on LGX and ReCOB crystals for application above 645°C,” in *Joint European Frequency and Time Forum International Frequency Control Symposium (EFTF/IFC)*, pp. 977–979, 2013.
- [51] C. Niezrecki, D. Brei, S. Balakrishnan, and A. Moskalik, “Piezoelectric Actuation: State of the Art,” *The Shock and Vibration Digest*, vol. 33, pp. 269–280, 2001.
- [52] P. Zhang, “Sensors and actuators,” in *Advanced Industrial Control Technology*, ch. 3, pp. 73–116, William Andrew Publishing, 2010.

- [53] Y. Fu, J. Luo, A. Flewitt, and W. Milne, “Smart microgrippers for bioMEMS applications,” in *MEMS for Biomedical Applications*, Woodhead Publishing Series in Biomaterials, ch. 11, pp. 291–336, Woodhead Publishing, 2012.
- [54] H. J. Park, D. S. Lee, and J. H. Park, “Ultra precision positioning system for servo motor–piezo actuator using the dual servo loop and digital filter implementation,” *International Journal of Machine Tools and Manufacture*, vol. 41, no. 1, pp. 51–63, 2001.
- [55] D. Horsley, N. Wongkomet, R. Horowitz, and A. Pisano, “Precision positioning using a microfabricated electrostatic actuator,” *IEEE Transactions on Magnetics*, vol. 35, no. 2, pp. 993–999, 1999.
- [56] S. T. Ho and S. J. Jan, “A piezoelectric motor for precision positioning applications,” *Precision Engineering*, vol. 43, pp. 285–293, 2016.
- [57] D. J. Bell, T. J. Lu, N. A. Fleck, and S. M. Spearing, “MEMS actuators and sensors: observations on their performance and selection for purpose,” *Journal of Micromechanics and Microengineering*, vol. 15, no. 7, pp. S153–S164, 2005.
- [58] J. H. Park, H. C. Lee, Y. H. Park, Y. D. Kim, C. H. Ji, J. Bu, and H. J. Nam, “A fully wafer-level packaged RF MEMS switch with low actuation voltage using a piezoelectric actuator,” *Journal of Micromechanics and Microengineering*, vol. 16, no. 11, pp. 2281–2286, 2006.

- [59] N. J. Conway, Z. J. Traina, and S. G. Kim, “A strain amplifying piezoelectric MEMS actuator,” *Journal of Micromechanics and Microengineering*, vol. 17, no. 4, pp. 781–787, 2007.
- [60] K. Srinivasa Rao, M. Hamza, P. Ashok Kumar, and K. Girija Sravani, “Design and optimization of mems based piezoelectric actuator for drug delivery systems,” *Microsystem Technologies*, vol. 26, no. 5, pp. 1671–1679, 2020.
- [61] L. Headings and G. Washington, “Stiffness Controlled Piezoelectric Stick-Slip Actuator for Rapid Positioning Applications,” in *ASME International Mechanical Engineering Congress and Exposition*, vol. 70, pp. 249–258, 2005.
- [62] R. C. Simões, J. Valder Steffen, J. D. Hagopian, and J. Mahfoud, “Modal Active Vibration Control of a Rotor Using Piezoelectric Stack Actuators,” *Journal of Vibration and Control*, vol. 13, no. 1, pp. 45–64, 2007.
- [63] L. Sui, X. Xiong, and G. Shi, “Piezoelectric Actuator Design and Application on Active Vibration Control,” *Physics Procedia*, vol. 25, pp. 1388–1396, 2012.
- [64] Q. M. Wang, X. H. Du, B. Xu, and L. Cross, “Theoretical analysis of the sensor effect of cantilever piezoelectric benders,” *Journal of Applied Physics*, vol. 85, pp. 1702–1712, 1999.

- [65] R. G. Ballas, *Piezoelectric Multilayer Beam Bending Actuators: Static and Dynamic Behavior and Aspects of Sensor Integration*. Springer, 2007.
- [66] “IEEE Standard on Piezoelectricity,” *ANSI/IEEE Std 176–1987*, pp. 1–64, 1988.
- [67] A. Aabid, M. Hrairi, S. J. Mohamed Ali, and Y. E. Ibrahim, “Review of Piezoelectric Actuator Applications in Damaged Structures: Challenges and Opportunities,” *ACS Omega*, vol. 8, no. 3, pp. 2844–2860, 2023.
- [68] R. Mindlin, “Equations of high frequency vibrations of thermopiezoelectric crystal plates,” *International Journal of Solids and Structures*, vol. 10, no. 6, pp. 625–637, 1974.
- [69] W. Nowacki, “Some general theorems of thermopiezoelectricity,” *Journal of Thermal Stresses*, vol. 1, no. 2, pp. 171–182, 1978.
- [70] J. P. Nowacki, “Steady-state problems of thermopiezoelectricity,” *Journal of Thermal Stresses*, vol. 5, no. 2, pp. 183–194, 1982.
- [71] D. Chandrasekharaiah, “A temperature-rate-dependent theory of thermopiezoelectricity,” *Journal of Thermal Stresses*, vol. 7, no. 3–4, pp. 293–306, 1984.
- [72] D. S. Chandrasekharaiah, “A generalized linear thermoelasticity theory for piezoelectric media,” *Acta Mechanica*, vol. 71, no. 1, pp. 39–49, 1988.

- [73] S. Rao and M. Sunar, "Analysis of distributed thermopiezoelectric sensors and actuators in advanced intelligent structures," *AIAA Journal*, vol. 31, no. 7, pp. 1280–1286, 1993.
- [74] H. S. Tzou and R. V. Howard, "A Piezothermoelastic Thin Shell Theory Applied to Active Structures," *Journal of Vibration and Acoustics*, vol. 116, no. 3, pp. 295–302, 1994.
- [75] H. S. Tzou and R. Ye, "Piezothermoelasticity and Precision Control of Piezoelectric Systems: Theory and Finite Element Analysis," *Journal of Vibration and Acoustics*, vol. 116, pp. 489–495, 1994.
- [76] J. S. Yang and R. C. Batra, "Free vibrations of a linear thermopiezoelectric body," *Journal of Thermal Stresses*, vol. 18, no. 2, pp. 247–262, 1995.
- [77] R. F. Fung, J. S. Huang, and S. C. Jan, "Dynamic Analysis of a Piezothermoelastic Resonator with Various Shapes," *Journal of Vibration and Acoustics*, vol. 122, no. 3, pp. 244–253, 2000.
- [78] F. Ashida and T. R. Tauchert, "Thermally-induced wave propagation in a piezoelectric plate," *Acta Mechanica*, vol. 161, pp. 1–16, 2003.

- [79] X. Tian, J. Zhang, S. Yapeng, and T. Lu, “Finite element method for generalized piezothermoelastic problems,” *International Journal of Solids and Structures*, vol. 44, pp. 6330–6339, 2007.
- [80] F. A. Alshaikh, “The Mathematical Modelling for Studying the Influence of the Initial Stresses and Relaxation Times on Reflection and Refraction Waves in Piezothermoelastic Half-Space,” *Applied Mathematics*, vol. 03, no. 08, p. 14, 2012.
- [81] P. Li, F. Jin, and J. Ma, “Mechanical analysis on extensional and flexural deformations of a thermo-piezoelectric crystal beam with rectangular cross section,” *European Journal of Mechanics*, vol. 55, pp. 35–44, 2016.
- [82] R. Mindlin, “High frequency vibrations of piezoelectric crystal plates,” *International Journal of Solids and Structures*, vol. 8, no. 7, pp. 895–906, 1972.
- [83] H. Elahi, M. Eugeni, P. Gaudenzi, M. Gul, and R. F. Swati, “Piezoelectric thermo electromechanical energy harvester for reconnaissance satellite structure,” *Microsystem Technologies*, vol. 25, no. 2, pp. 665–672, 2019.
- [84] H. Elahi, “The investigation on structural health monitoring of aerospace structures via piezoelectric aeroelastic energy harvesting,” *Microsystem Technologies*, vol. 27, no. 7, pp. 2605–2613, 2021.

- [85] H. S. Tzou, *Piezoelectric Shell Vibration Theory*, ch. 2, pp. 13–62. Dordrecht, Netherlands: Springer, 1993.
- [86] T. R. Tauchert, “Plane piezothermoelastic response of a hybrid laminate — a benchmark problem,” *Composite Structures*, vol. 39, no. 3, pp. 329–336, 1997.
- [87] K. J. Bathe, *Finite Element Method*, pp. 1–12. John Wiley & Sons Ltd, 2008.
- [88] T. J. R. Hughes, *The Finite Element Method : Linear Static and Dynamic Finite Element Analysis*. Dover Publications, 2005.
- [89] S. Duczek, *Higher order finite elements and the fictitious domain concept for wave propagation analysis*. PhD thesis, Otto-von-Guericke-Universität Magdeburg, 2014.
- [90] B. M. Irons, “Engineering applications of numerical integration in stiffness methods,” *AIAA Journal*, vol. 4, no. 11, pp. 2035–2037, 1966.
- [91] L. Lapidus and G. F. Pinder, *Numerical solution of partial differential equations in science and engineering*. John Wiley & Sons, Inc., 1982.
- [92] J. H. Zhi-Fang Fu, *Modal Analysis*. Butterworth-Heinemann, 1st ed., 2001.
- [93] F. Shang, M. Kuna, and M. Scherzer, “A Finite Element Procedure for Three-dimensional Analyses of Thermopiezoelectric Structures in Static Applica-

tions,” *Technische Mechanik - European Journal of Engineering Mechanics*, vol. 22, no. 3, p. 235–243, 2002.

[94] D. Xu, Y. Liu, J. Liu, X. Yang, and W. Chen, “Developments of a piezoelectric actuator with nano-positioning ability operated in bending modes,” *Ceramics International*, vol. 43, pp. S21–S26, 2017.

[95] G. Y. Gu, L. M. Zhu, C. Y. Su, and H. Ding, “Motion Control of Piezoelectric Positioning Stages: Modeling, Controller Design, and Experimental Evaluation,” *IEEE/ASME Transactions on Mechatronics*, vol. 18, no. 5, pp. 1459–1471, 2013.